

Instituto Tecnológico y de Estudios Superiores de Monterrey

Campus Monterrey

School of Engineering and Sciences



Case Studies in Electric Arc Furnace Off-gases Transport and Steam Explosion Onset

Thesis presented by

Jorge Contreras Serna

Submitted to

School of Engineering and Sciences

in partial fulfillment of the requirements for the degree of

Master of Science

in Energetic Engineering

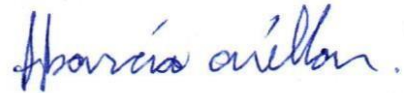
Monterrey Nuevo León, May 15th, 2018

Instituto Tecnológico y de Estudios Superiores de Monterrey

Campus Monterrey

School of Engineering and Sciences

The committee members, hereby, certify that have read the thesis presented by Jorge Contreras Serna and that it is fully adequate in scope and quality as a partial requirement for the degree of Master of Science in Energetic Engineering,



Dr. Alejandro Javier García Cuéllar
Tecnológico de Monterrey
School of Engineering and Sciences
Principal Advisor



Dr. Carlos Iván Rivera Solorio
Tecnológico de Monterrey
Committee Member



Dr. José Luis López Salinas
Tecnológico de Monterrey
Committee Member



Dr. Rubén Morales Menéndez
Associate Dean of Graduate Studies
School of Engineering and Sciences

Monterrey Nuevo León, May 15th, 2018

Declaration of Authorship

I, **Jorge Contreras Serna**, declare that this thesis titled, “**Case Studies in Electric Arc Furnace Off-gases Transport and Steam Explosion Onset.**” and the work presented in it are my own. I confirm that:

- This work was done wholly or mainly while in candidature for a research degree at this University.
- Where any part of this thesis has previously been submitted for a degree or any other qualification at this University or any other institution, this has been clearly stated.
- Where I have consulted the published work of others, this is always clearly attributed.
- Where I have quoted from the work of others, the source is always given. With the exception of such quotations, this thesis is entirely my own work.
- I have acknowledged all main sources of help.
- Where the thesis is based on work done by myself jointly with others, I have made clear exactly what was done by others and what I have contributed myself.



Jorge Contreras Serna
Monterrey Nuevo León, May 15th, 2018

Dedication

*To my parents Joel and Teresa.
To my siblings Josué, Joel and Verónica.
To all my friends and family.*

Acknowledgements

To my parents, Joel and Teresa, that always supported me to carry this Master's degree out.

I'm grateful with my twin, Josué, for being this entire process by my side helping each other.

I specially give thanks to my advisor, Dr. Alejandro Javier García Cuéllar, for all the invaluable knowledge and advices he shared with me, this research could not be possible without his support.

Also, I give thanks to Marco Herrera for the advices and the experience he shared me about the processes in the Steelmaking Industry and to Ternium for the data for carrying out this project.

I appreciate the economic support provided by the Tecnológico de Monterrey and SENER-CONACYT, this project would not be possible without those contributions.

This research is a product of the Project 266632 "Bi-National Laboratory on Smart Sustainable Energy Management and Technology Training" funded by the CONACYT SENER Fund for Energy Sustainability (Agreement: S0019-2014-01).

Case Studies in Electric Arc Furnace Off-gases Transport and Steam Explosion Onset.

by

Jorge Contreras Serna

Abstract

Steel production in an EAF may pose a serious security risk in the event of water leaks into the molten steel, causing violent steam explosions.

This thesis presents two important topics related to the Steel Making Industry. The first one is about the detection of water vapor (steam) inside the off-gas duct of an Electric Arc Furnace (EAF). And the Second one is about knowing the preconditions of melt fragmentation in a steam explosion.

A way to detect the presence of large quantities of water inside the EAF is by monitoring its off-gas duct content of water vapor. Determining where to place a probe for water vapor detection inside the duct, is of the greatest importance as this might be the first warning for the appearance of a risk situation. A computational fluid dynamics (CFD) simulation is carried out using ANSYS Fluent software to obtain the point with highest concentration of water vapor. Water vapor channeling is assumed in the inlet of the off-gas duct so that a worst-case scenario is presented. Three-dimensional simulations were run with the inlet gas containing CO₂, CO, H₂O (steam), and air. The first three components enter through the duct while air enters through small gaps in the duct. Different combinations of the inlet position of CO₂, CO and H₂O were considered to estimate a pattern for the water vapor flow through the duct. The results show that if the steam enters in a channelized way, it will tend to continue in that path along the duct. The simulation results show the zones of the off-gas duct with a higher concentration of steam. These results can guide locating the gas probe and provide a better warning of a water leak.

About the other topic, fragmentation of molten metal is an important process in steam explosions caused by melt-coolant interactions. This part of the research is dedicated to investigating how the fragmentation of the melt droplets occurs and melt jets formation in different mechanisms like a metal droplet falling in water or in a stratified water/liquid metal system. Also, an explanation of the most significant parameters in these processes is performed. 2-D computational fluid dynamics (CFD) simulations are carried out using ANSYS Fluent software to study these phenomena. The results show that the larger the pressure or density, the greater the melt jet length for a stratified system. And the larger velocity or density, the greater deformation for a melt droplet in a water pool. The formation of melt jets of Ciccarelli and Frost's experiments is observed, and fragmentation of melt droplets was also observed during current simulations.

List of Figures

Figure 1-1. EAF steelmaking process. Image taken from (BCSA, Steel for Life, and SCI 2012)	2
Figure 2-1. Refractory lining used on EAF in the past. Image taken from (Pinto, Totti, and Hopperdizel 2015).	5
Figure 2-2. Temperature and off-gas composition measured at the fume duct elbow. Image taken from (Malfa et al. 2009).	8
Figure 2-3. Streamlines of gaseous medium in EAF working space for a) annular distributing exhaust duct and b) traditional off-gas removal system. Image taken from (Timoshenko, Semko, and Timoshenko 2014).....	9
Figure 2-4. Gases concentration measured in Ternium, 2010.....	11
Figure 2-5. Inlets and outlets in the geometry.	11
Figure 2-6. Electric Arc Furnace and duct parts.	12
Figure 2-7. Schematic view of an EAF and duct system (Kirschen, Velikorodov, and Pfeifer 2006).....	12
Figure 2-8. Duct measurements.....	13
Figure 2-9. Representation of the main cases, indicating the steam inlets.....	15
Figure 2-10. Gases inlets when 15% of steam concentration is set.	16
Figure 2-11. Gas detector probe collocation.....	18
Figure 2-12. Velocity contour when steam enters by right inlet at 6 m/s.	19
Figure 2-13. Typical mass fraction contour of case #1.	20
Figure 2-14. Mass concentration plane for case #1, when velocity is 6 m/s.....	21
Figure 2-15. Lines of concentration for case #1, when velocity is 6 m/s.....	21
Figure 2-16. Mass fraction in the maximum and probe lines along Z axis for case #1.	21
Figure 2-17. Typical mass fraction contour of case #2.	23
Figure 2-18. Lines of concentration for case #2, when velocity is 6 m/s.....	23
Figure 2-19. Typical mass fraction contour of case #3.	24
Figure 2-20. Lines of concentration for case #3, when velocity is 6 m/s.....	25

Figure 2-21. Mass fraction in the maximum and probe lines along Z axis for case #3	25
Figure 2-22. Velocities contour when the gases are uniformly mixed.....	26
Figure 2-23. a) Air mass fraction, b) CO mass fraction, c) CO ₂ mass fraction, d) H ₂ O mass fraction.....	28
Figure 2-24. Mass fraction contour when all the gases are mixed.....	28
Figure 2-25. Steam mass fraction in the maximum and probe lines along Z axis whe the gases are uniformly mixed.	29
Figure 3-1. Steam explosion phases a) to c). Image taken from (Hyder and Allison 1992).	34
Figure 3-2. Steam explosion phases d) to e). Image taken from (Hyder and Allison 1992).	34
Figure 3-3. Sand mold system and ladle for filling the mold with molten stainless steel (Li and Ji 2016).	36
Figure 3-4. a) to c) Schematic illustration of different modes of break-up of large liquid drops into smaller droplets (Lee and Frost 1987; Pilch M. 1979).	37
Figure 3-5. d) to f) Schematic illustration of different modes of break-up of large liquid drops into smaller droplets (Lee and Frost 1987; Pilch M. 1979).	38
Figure 3-6. Fragmentation mechanism proposed by Kim. Image taken from (Leclerc and Berthoud 2003).	40
Figure 3-7. Splash theory model. Image taken from (Leclerc and Berthoud 2003).	40
Figure 3-8. Ciccarelli and Frost fragmentation mechanism (Ciccarelli and Frost 1994).	41
Figure 3-9. Apparatus used in stratified system of melt and water (Ciccarelli 1991).	43
Figure 3-10. Formation of melt jets, obtained by Ciccarelli and Frost (1994).	43
Figure 3-11. Geometry and boundary conditions of the simulated domain (stratified water/liquid metal system).	46
Figure 3-12. Time-step independence study: variation of spike maximum height with the time step size.	48

Figure 3-13. Mesh convergence study: variation of spike maximum height with time for different meshes.....	49
Figure 3-14. The computational mesh M4.....	50
Figure 3-15. Measurement with Digimizer. In the right, reference measure is added indicating the vapor film thickness.....	50
Figure 3-16. Overlapped results for different boundary conditions in the walls.	51
Figure 3-17. Density contours at various time instants for pressure pulse of 100 MPa.....	52
Figure 3-18. Variation of jet length with time for various melt densities when initial pressure is 40 MPa.	53
Figure 3-19. Variation of jet length with time for various initial pressures when density is 7000 kg/m ³	53
Figure 3-20. Density contour with a pressure of 40 MPa and a density of (a) 10000 kg/m ³ and (b) 3000 kg/m ³ , both at 1 ms.	54
Figure 3-21. Density contour with a density of 7000 kg/m ³ and an initial pressure of (a) 40 MPa and (b) 10 MPa, both at 1 ms.	54
Figure 3-22. Variation of jet length with time for different vapor film thickness when density is 7000 kg/m ³ and pressure is 10 MPa.....	55
Figure 3-23. Spike height vs Bond number.	56
Figure 3-24. Shape regime map for the formation of melt jets overlapped with the bubble shape regime from Amaya-Bower and Lee (2010).	57
Figure 3-25. Shock adiabatic for an initial mixture of equal volumes of tin (1000°C), water (100°C) and steam (Board, Hall, and Hall 1975).	59
Figure 3-26. Hugoniot analysis for current simulation with tin (1000°C), water (100°C) with equal volumes a vapor with a fraction of 0.029 of the total volume. .	60
Figure 3-27. Metal droplet without vapor film in water pool (Ma et al. 2002).	61
Figure 3-28. Metal droplet with vapor film in water pool (Ma et al. 2002).	62
Figure 3-29. Molten metal droplet in water pool (Thakre, Ma, and Li 2013).	63
Figure 3-30. Molten metal droplet surrounded by a vapor film (Thakre, Ma, and Li 2013).	63
Figure 3-31. Geometry and boundary conditions of melt droplet in water.	64

Figure 3-32. Geometry and boundary condition of melt droplet with vapor film in water.	64
Figure 3-33. Melt droplet deformation through time, when $V_{initial} = 2.5$ m/s.	65
Figure 3-34. Change in droplet perimeter with various initial velocities when density is 6600 kg/m^3	65
Figure 3-35. Change in droplet perimeter with various melt densities when initial velocity is 2.5 m/s.	66
Figure 3-36. Melt droplet with vapor film deformation through time, when $V_{initial} = 2.5$ m/s.	66
Figure 3-37. Change in droplet perimeter with various vapor film thicknesses.	67
Figure 3-38. Change in droplet perimeter with various initial velocities when density is 6600 kg/m^3 and vapor film thickness is 0.15 mm.	68
Figure 3-39. Change in droplet perimeter with various initial densities when V_{init} is 25 m/s and vapor film thickness is 0.15 mm.	68
Figure 3-40. Thermal effects on melt droplet with unstable vapor film (Zhong et al. 2014).	69
Figure 3-41. Geometry and boundary conditions for melt droplet with vapor film and thermal effects.	70
Figure 3-42. Sequence of melt droplet deformation when thermal effects are present.	71
Figure 3-43. Change in spike length with various initial densities when vapor film thickness is 0.5 mm.	71
Figure 3-44. Change in spike length with various vapor film thicknesses when melt density is 7000 kg/m^3	72
Figure 3-45. Aspect ratio L/Ro according the Bond number.	73
Figure 3-46. Geometry for single water jet in molten metal (Koshizuka, Ikeda, and Oka 1999).	73
Figure 3-47. Water jet impingement in molten tin in a time interval of 0.6 ms.	74
Figure 3-48. Experimental apparatus used by Zhou et al. (2014).	74
Figure 3-49. Sequence of explosive interaction of a water droplet in molten tin (Zhou et al. 2014).	75

Figure 3-50. Water droplet in molten metal model (Lin et al. 2014).....	75
Figure 3-51. Sequence of molten tin surface deformation caused by water droplet (Lin et al. 2014).	76
Figure 3-52. Geometry and boundary conditions for water jet falling in molten metal.	77
Figure 3-53. Water jet impingement sequence when initial velocity is 5 m/s.	78
Figure 3-54. Length scales in calculation results.....	78
Figure 3-55. Change in the formed crater depth or height through time for various simulations of water falling in molten metal.	79
Figure 3-56. Change in the formed crater width through time for various simulations of water falling in molten metal.....	79

List of Tables

Table 2-1. Mass flow rates for each variation when steam enters by right inlet. ...	19
Table 2-2. Results when steam enters by the right inlet.	22
Table 2-3. Results when steam enters by the middle inlet.	24
Table 2-4. Results when steam enters by the left inlet.	26
Table 3-1. Surface tensión values.	47
Table 3-2. Various computational meshes considered for the mesh convergence study.	48
Table 3-3. Bond number when pressure is varied, and density is 7000 kg/m^3	55
Table 3-4. Bond number when density is varied, and pressure is 40 MPa	56
Table 3-5. Bond number when density is varied, and pressure is 4 MPa	72
Table 3-6. Summary of results for molten metal fragmentation.	80
Table A-1. Abbreviations.	89
Table A-2. Acronyms.	89
Table A-3. Symbols.	89
Table A-4. Subscripts.	90

Table of Contents

Abstract	i
List of Figures	iii
List of Tables	viii
Chapter 1. General Introduction	1
1.1 General view of the process	1
1.2 General Objective	3
1.3 Justification	3
1.4 Thesis Organization	3
Chapter 2. Numerical Analysis of the Off-gases Through the Duct	5
2.1 Introduction	5
2.2 Specific Objective	7
2.3 Previous Related Studies	7
2.3.1 Gases Density Effects	9
2.4 Methodology	10
2.4.1 Off-gas Duct Geometry	11
2.4.2 Assumptions	13
2.4.3 Governing Equations	14
2.4.4 Tested Cases	15
2.5 Results	17
2.5.1 Steam entering by right inlet (Case #1)	18
2.5.2 Steam entering by middle inlet (Case #2)	22
2.5.3 Steam entering by left inlet (Case #3)	24
2.5.4 Uniformly mixed gases.	26
2.6 Discussion and Conclusions	29

2.7	Future Work	30
Chapter 3. Numerical Analysis of Molten Metal Fragmentation in Steam Explosions. 32		
3.1	Introduction	32
3.1.1	History of Steam Explosions.....	35
3.2	Specific Objective.....	36
3.3	Fragmentation Mechanisms	36
3.3.1	Hydrodynamic Fragmentation.....	36
3.3.2	Thermal Fragmentation	40
3.4	Simulated Models.....	41
3.4.1	Model 1. Formation of Melt Jets.....	42
3.4.2	Molten Metal Droplet in Water	60
3.4.3	Model 5. Water Jet Falling in Molten Metal.....	73
3.5	Summary of Results	80
3.6	Conclusions.....	82
3.7	Future Work	83
Chapter 4. Contributions		
		84
Bibliography.....		
		85
Appendix A.....		
		89
Curriculum Vitae.....		
		91

Chapter 1. General Introduction

The electric arc furnace (EAF) in the steel industry was invented in 1889 by Paul Héroult. This technology has become one of the most used invents in steel industry and it is one of the most energy consumer around the world. The EAF is a very studied technology in order to minimize its energy consumption, to enhance the steel production and quality, to improve the safety around it, and so other topics.

Since the walls of the EAF are cooled with water, the process becomes dangerous when a water leak occurs. Hence, this thesis focuses on finding water leaks inside the EAF and on studying the main characteristics that cause a steam explosion.

When the steam explosions are very strong, heat transfer rates are extrem and the hot molten metal gets extremely dispersed into micro droplets of diameters of 10 μm . This process is name “fined fragmentation” and it is caused by:

- The entrapment of water between the initial metal globule and the containment bottom.
- Trapped water inside the initial metal globule.
- Violent nuclear boiling of the water.

This thesis studies two topics of high importance, the first focuses on the path the steam, (water vapor) takes inside the off-gas duct and the second studies the molten metal fragmentation mechanisms in steam explosions.

1.1 General view of the process

In an EAF, the scrap and DRI (direct reduced iron) are firstly loaded into the furnace and then the roof is closed, the electrodes transfer electrical energy for the melting process. Also, natural gas and oxygen are injected from the burners and get combusted releasing chemical energy to heat more the scrap.

The scrap and DRI melt by absorbing the electrical, chemical and radiation energy. Due to the reaction of the scrap a slag layer is formed, and it covers the wall from the arc radiation. Each batch duration is about 60 minutes. Water-Cooling panels are used to cool down the roof and the walls of the EAF (Ghobara 2013).

The generated gases during the process of the EAF are extracted by the off-gas system, that is made also to combust hazardous gases such as CO and to filter out the dust (Bekker, Craig, and Pistorius 2000). These gases can be detected and measured with gas detectors within the duct.

Once the steel temperature and chemistry are correct, the steel is extracted by tilting the furnace. Few tonnes of steel are left in the furnace to maintain it hot, and the next load of scrap and DRI melts faster. The refractory as well as water-cooled panels are inspected for water leaks. Figure 1-1 shows the steelmaking process.

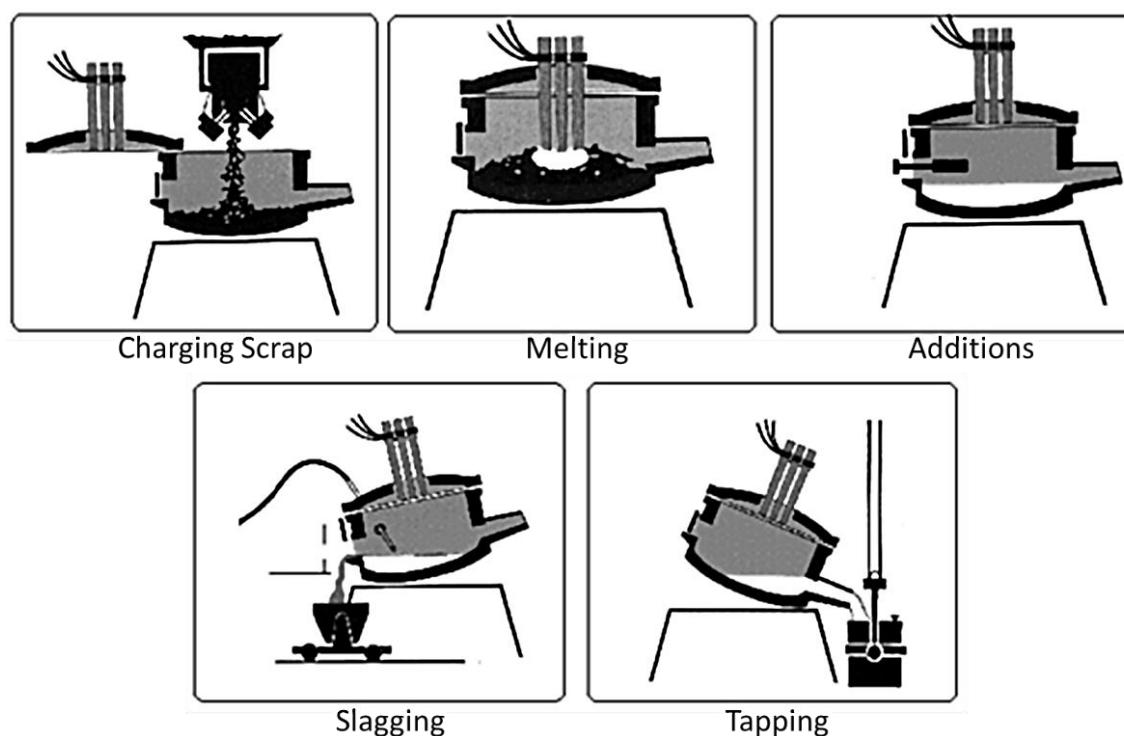


Figure 1-1. EAF steelmaking process. Image taken from (BCSA, Steel for Life, and SCI 2012)

When the furnace is completely emptied for maintenance, refractory walls are repaired if needed. And the whole water-cooled panels system is changed for a new one. This is made to avoid potential steam explosions.

1.2 General Objective

The general objective of this work is to help in finding the best place to collocate a gas detector inside an EAF off-gas duct and to study the mechanisms that exist for molten metal fragmentation in steam explosions, emphasizing the study on the formation of molten metal jets (spikes) in a stratified water/liquid metal system.

The specific objectives for each studied topic are given in the next chapters.

1.3 Justification

The studied topics are very important for both, industry and scientific community. Industrial safety is of big matter because serious accidents have occurred in the steel industry and in nuclear power plants.

The study of the steam (water vapor) inside the off-gas duct of an EAF is important to do a better detection of water leaks and be able to avoid steam explosions.

And the study about the molten metal fragmentation in steam explosions is important because it will give a better perspective on how this phenomenon is produced and what are the parameters that affect it the most.

1.4 Thesis Organization

Two important topics related to the Steel Making Industry are presented in this thesis. The first study is about the detection of water vapor (steam) inside the off-

gas duct of an Electric Arc Furnace (EAF). And the second study is about the molten metal fragmentation in a steam explosion.

Chapter 1 is about a general introduction of the studied topics and how the steel making process is performed.

Chapter 2 starts with a more specific introduction and literature review about the off-gases study. Then the problem is described. Methodology, results and conclusions of the off-gases computational simulations are presented.

Chapter 3 displays a more detailed introduction and literature review about the molten metal fragmentation and melt jets formation in steam explosions. Five different cases are simulated. Previous studies, methodology, results and conclusions of the computational simulations for each case are presented.

Chapter 4 addresses a summary of the contributions that this thesis provides to the steelmaking industry and to academic fields like nuclear engineering.

Chapter 2. Numerical Analysis of the Off-gases Through the Duct.

2.1 Introduction

Back in time the EAF's had refractory lining in the lower shell, upper shell and in the roof, as shown in Figure 2-1. To avoid down times by repairing the refractory, water-cooled panels have been being installed in the furnaces as walls.

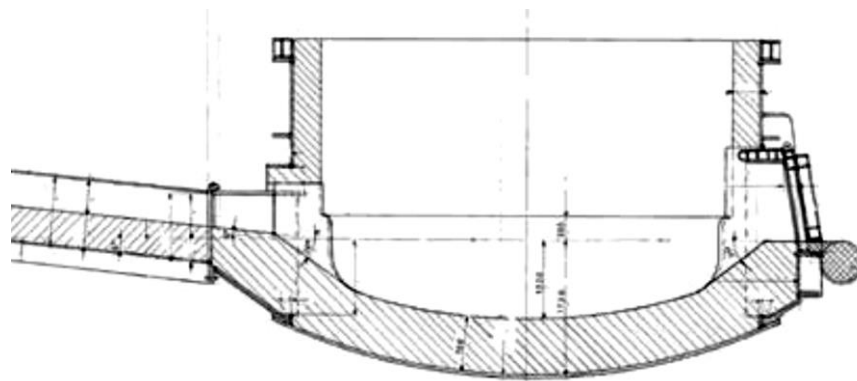


Figure 2-1. Refractory lining used on EAF in the past. Image taken from (Pinto, Totti, and Hopperdizel 2015).

The water-cooled panels are typically installed about 350 mm above the liquid steel level, and their connection to the water cooling system is located at the top of the panel, through hoses (Pinto, Totti, and Hopperdizel 2015).

Some advantages obtained with the use of water-cooled panels are:

- Increased productivity.
- Reduced downtime to repair refractory material.
- Economic advantage by reducing refractory consumption.

Although water-cooled panels are very good, they cause two factors of concern, the first factor is the increase of heat losses in the manufacture of liquid steel due to the

extraction of heat by water-cooled panels. And the second factor refers to the risk of water leaks from the panels into the EAF. The heat that the panels receive is not constant and that causes the panels to suffer thermomechanical fatigue of the tubes. This causes microcracks and minimal water leakage but over time, these microcracks expand and the amount of the water leakage increases. Small leaks are very difficult to detect even by operational experts and detection systems, and will cause wetting of the refractory lining, bringing water to the refractory-shell interface, which can cause explosions and/or damage in the furnace.

Large water leaks in an EAF are responsible for explosions and ejections of hot molten steel out of the EAF. This phenomenon occurs when the water inside the EAF is covered with a high-temperature liquid metal (steel or slag). Water leaks are usually detected by a visual inspection of the EAF, and this only depends on the expertise of the operators. (Pinto, Totti, and Hopperdizel 2015).

To detect water leaks inside the EAF, there exist automated detection systems some of them are:

- Flowmeters in the inlets and outlets of the entire system of panels or can be placed a pair of flowmeters for each panel, this will increase the precision to detect a small water leak as well as the time of detection will be reduced. The inlet mass flow rate of water must be the same as the mass flow rate in the outlet, a difference on this measurement indicates a water leak.
- Measurement of water vapor in the off-gas duct of the EAF with tunable diode laser absorption spectrometer (TDLAS). This instrument uses wavelength modulation spectroscopy to provide a quantitative determination of water vapour in the raw off-gases. The variation of vapour concentration is analysed and used for the detection of waterleaks (Dennis and Ganguly 2010).

- Extraction of sample gases with probe inserted in the off-gas duct. The probe is placed in a specific position to ensure that the sample extracted is gas coming from the furnace and not to be mixed with the air that comes from the combustion gap. The gas is transported to the analyser cabinet where the sample is filtered and dried then it is analyzed. O₂, CO, CO₂ and H₂ are measured, water leaks are predicted with the H₂ measured (Boin, Vazquez, and Levrangi 2012).
- There is also a hybrid system that uses both an extractive probe and lasers. A sample of gas is extracted from the duct then is analyzed through various lasers to detect the components in the off-gas system. Information is sent back to the control computer using fiber optic cable (Spencer and Cochran 2015).

This chapter focuses on finding the best position to place any of the mentioned detection systems.

2.2 Specific Objective

To study the path that the steam takes within the off-gas duct of an electric arc furnace (EAF) by computational simulation, and thereby detect the point of the duct where there is a higher concentration of steam in order to have a better lecture in detection system and be able to notify a water leak in a more efficient way.

2.3 Previous Related Studies

Malfa et al. (2009) developed a CFD simulation for the EAF process. On their work, they measured with TENOVA EFSOP® the concentrations of CO, CO₂ and the temperature of the off-gas composition at the exit of the furnace, in the elbow of the fume duct. Their measurements can be seen in Figure 2-2 where (S) is for the basket heating after the charge, (R) for the scrap melting and (C) for the refining.

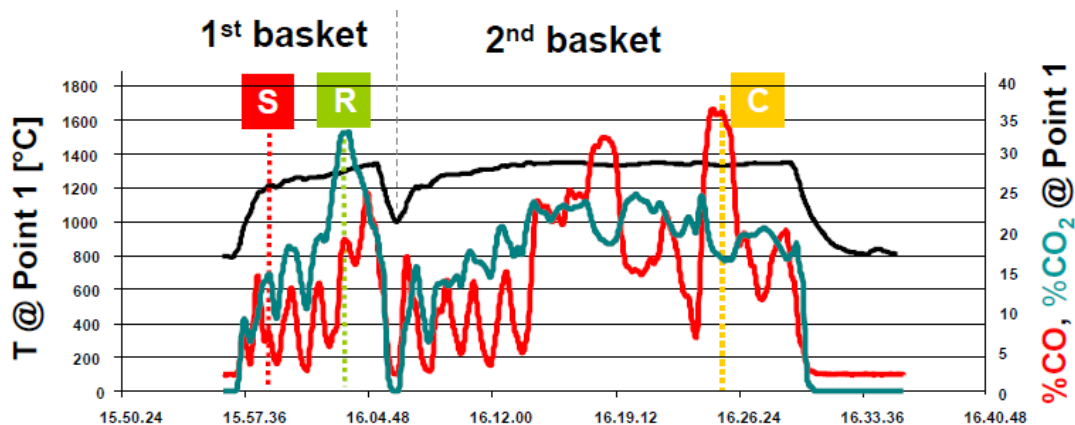


Figure 2-2. Temperature and off-gas composition measured at the fume duct elbow. Image taken from (Malfa et al. 2009).

Malfa et al. (2009) in one of their simulations they obtained that the temperature of the off-gases was above 1200°C and that the inlet velocity of the off-gases in the duct was about 0.4 m/s.

Zhang et al. (2009) developed a mathematical model for the gas flow and heat transfer in a ladle furnace. They simulated the gas velocity vector distribution, the gas flow line distribution, pressure and temperature distributions on the furnace lid wall. The furnace has two flues, the main flue (horizontal next to the electrodes) and the bending flue (In the edge of the furnace), both flues join after a mixing gas gap. Different pressures were simulated in the off-gas, it varies from 50 Pa to 200 Pa. The higher the pressure the higher the velocity of the off-gas, the maximum velocity was 20 m/s. When the pressure equals to 200 Pa, the average velocity of the off-gas in both flues is 10 m/s.

Timoshenko, Semko, and Timoshenko (2014) created a mathematical model of an EAF off-gas removal system to improve the energy efficiency in the smelting process. They state that the flowrate of the gases carries dust from the furnace and in union with the infiltration of cold air through the slag door, the efficiency of the furnace is aggravated. They propose an exhaust duct like the one of Figure 2-3a and it is good

to said that the average velocities that they observed in both types of duct was about 10 m/s.

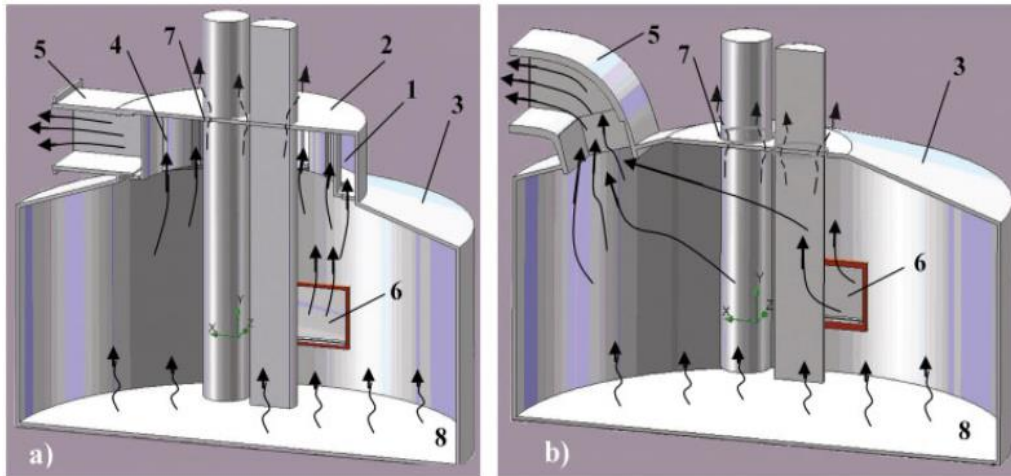


Figure 2-3. Streamlines of gaseous medium in EAF working space for a) annular distributing exhaust duct and b) traditional off-gas removal system. Image taken from (Timoshenko, Semko, and Timoshenko 2014).

With the off-gas duct proposed by (Timoshenko, Semko, and Timoshenko 2014) fugitive emissions can be reduced by 40%, air inflow into the furnace by 24%, total emissions by 13% and the melting dust removal by 33% due to annular distributing suction.

2.3.1 Gases Density Effects

Inside the off-gas duct exist two main reason for the mixing of gases, one is the turbulent effect that theses gases have when there are emitted from the furnaces and when they mix with the air that enters by the gaps after the elbow. And the other reason is due to the gases density difference, the ones with a higher molar mass will tend to go down and the ones with a lighter molar mass will tend to go up, occurring one kind of mixing.

All gases densities are in function on the ideal gases properties, the simulation software take the gases as ideal and from equation (1) it calculates the ρ gas density,

where P_{in} is the pressure in the gas inlet, T the temperature, M the molar mass and R the universal constant for ideal gases.

$$\rho = \frac{P_{in} * M}{R * T} \quad (1)$$

Ansys Fluent solves internally this equation and assignates that density for the corresponding gas according to the temperature and pressure it has, the molar mass and R are kept constant.

It has been experimentally observed that the ideal-gas relation closely approximates the P-V-T behavior of real gases at low densities. At low pressures and elevated temperatures, the density of a gas decreases and the gas behaves like an ideal gas. In the range of practical interest, many familiar gases such as air, nitrogen, oxygen, hydrogen, helium, argon, neon, and krypton and even heavier gases such as carbon dioxide can be treated as ideal gases with negligible error (often less than 1 percent) (Cengel and Cimbala 2014).

In the current study the utilized gases are: CO, CO₂, H₂O and air.

2.4 Methodology

Different simulations were performed in ANSYS Fluent to see the path of the steam through the off-gas duct of an EAF. This section describes what information and methodology were used to perform this analysis.

The gases concentration of the following tests was based in the graphic shown in Figure 2-4. The estimated concentration of each gas was: 23% for CO₂, 28% for CO, 5% for steam y 44% for air.

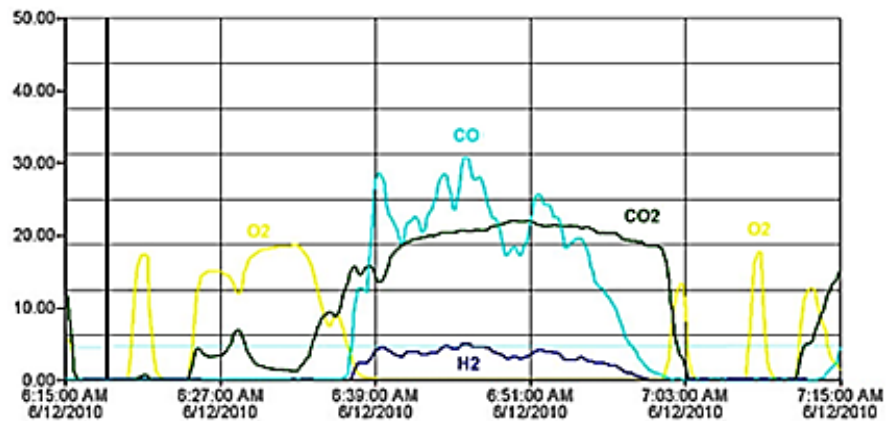


Figure 2-4. Gases concentration measured in Ternium, 2010.

2.4.1 Off-gas Duct Geometry

The Figure 2-5 shows the three-dimensional geometry of the duct with the inlets and outlets highlighted. All the tests had three inlets for the off-gases, one inlet for the air that enters through the gap between the elbow and the biggest part of the duct and one outlet where the all gases mix crosses.

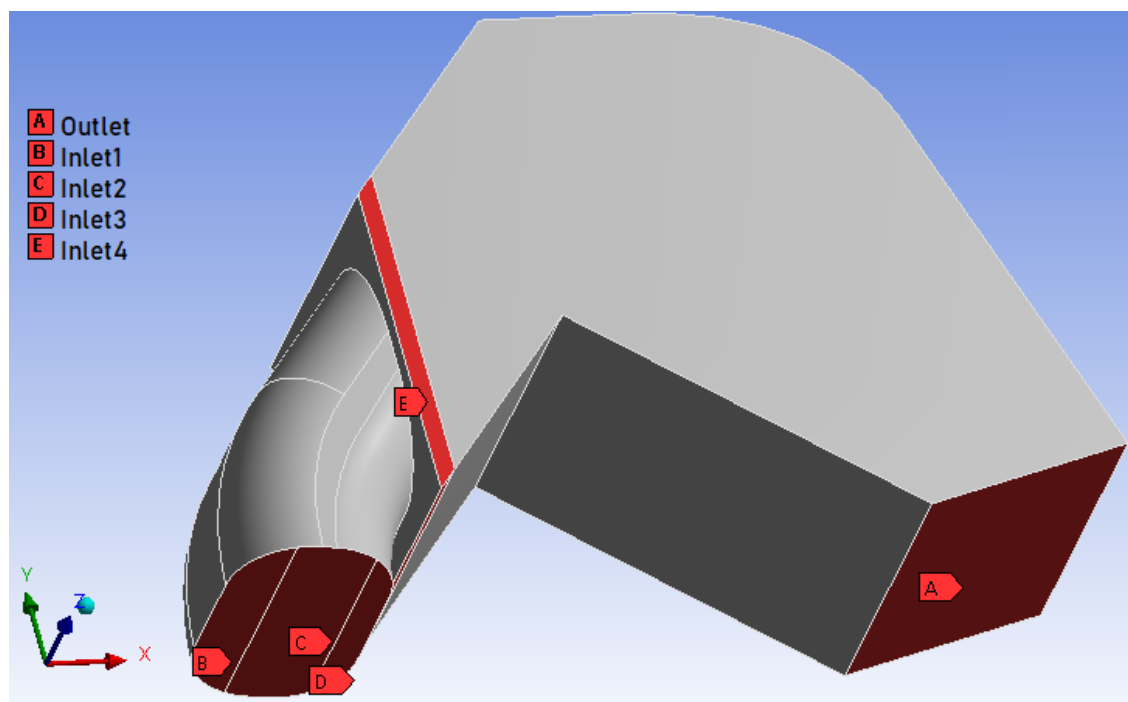


Figure 2-5. Inlets and outlets in the geometry.

Figure 2-6 is a real photograph of the electric arc furnace and the off-gas duct and Figure 2-7 is a schematic view of it. So, a better idea of the actual geometry can be made.

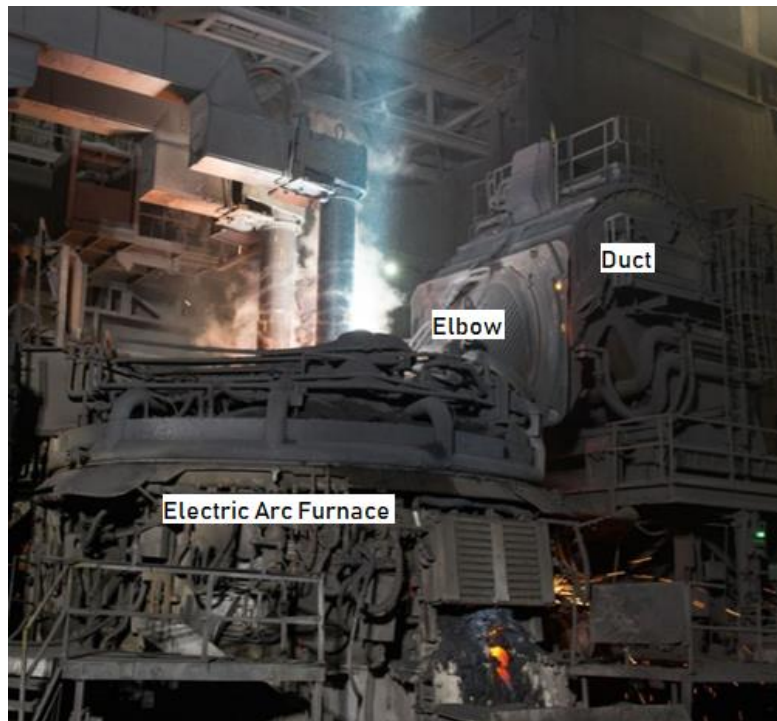


Figure 2-6. Electric Arc Furnace and duct parts.

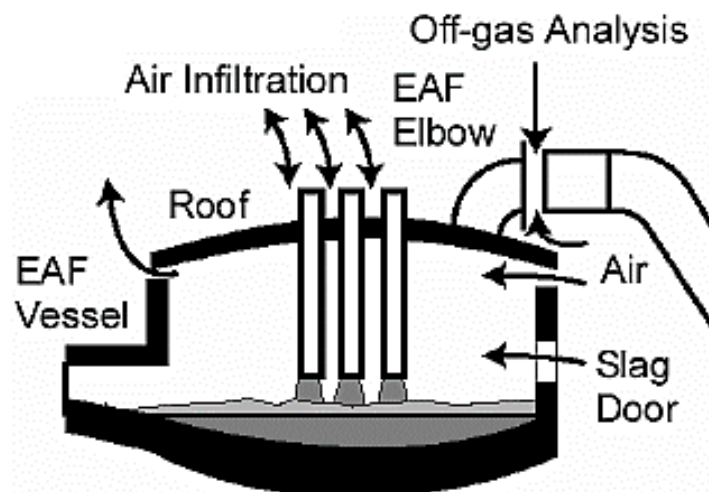


Figure 2-7. Schematic view of an EAF and duct system (Kirschen, Velikorodov, and Pfeifer 2006).

Most relevant distances of the drawn geometry are shown in Figure 2-8. The distance of 2.289 meters is the one where a probe or gas detector will be localized, and the half of the distance in “Y” axis is the height where these detectors are commonly placed. In the results section the position of gas detector will be explained with more details.

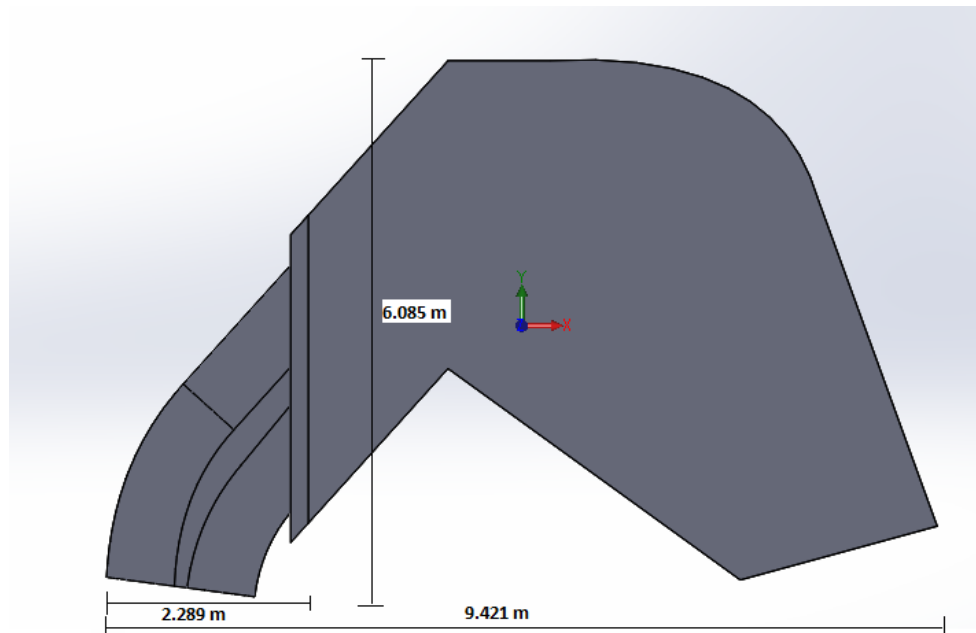


Figure 2-8. Duct measurements.

2.4.2 Assumptions

In (Timoshenko, Semko, and Timoshenko 2014; Zhang et al. 2009) simulations about the distribution of the velocities that the gases would have within an off-gas duct for an EAF were performed. Even though they used different configurations, they obtained an average gas velocity of 10 m/s in the duct inlet. So, for most of the tests simulated in this project, the base velocity for gases at the inlets was of 12 m/s, although simulations were also run with other velocities to observe if this parameter affects the path of the steam.

A temperature of 1073 K was utilized for CO₂, CO and H₂O gases, that are ones emitted by the furnace and enter the off-gas duct. The air that enters by the gaps after the elbow has a temperature of 313 K.

The initial pressure for CO₂, CO and H₂O gases was assumed at 1000 Pa and the air was assumed at 0 Pa (atmospheric pressure). The outlet pressure was set at -2500 Pa.

2.4.3 Governing Equations

Since four different gases are being used in steady stated, it was decided to use the “Species Transport” model. This model allows to have several species (gases) that can or not be mixed to each other. When the conservation equation wants to be solved for distinct species, the software predicts the local mass fraction of each Y_i specie, through the solution of equation (2) of convection-difussion for the i -th specie. This conservation equation takes the next general form:

$$\frac{\partial}{\partial t}(\rho^q \alpha^q Y_i^q) + \nabla \cdot (\rho^q \vec{v}^q Y_i^q) = -\nabla \cdot \alpha^q \vec{J}_i^q + R_i^q + S_i^q \quad (2)$$

Where R_i is the net rate of production of i species by chemical reaction for phase q , α^q is the volume fraction for phase q , S_i is the creation rate by addition of the disperse phases plus any user defined source, v is the velocity and J_i is the diffusion flux of species.

Instead of treating the turbulent dispersion as an interfacial momentum force in the phase momentum equations, the turbulent diffusion term is added in the governing equation of phase volume fraction. The term is $\nabla \cdot \alpha^q \vec{J}_i^q$. In turbulent flows, ANSYS Fluent computes the mass diffusion as:

$$\vec{J}_i = -\left(\rho D_{i,m} + \frac{\mu_t}{Sc_t}\right) \nabla Y_i \quad (3)$$

Where $D_{i,m}$ is the diffusion coefficient for species i in the mixture, Sc_t is the turbulent Schmidt number ($\frac{\mu_t}{\rho D_t}$ where μ_t is the turbulent viscosity and D_t is the turbulent diffusivity). The default Sc_t is 0.7.

2.4.4 Tested Cases

Three main cases were analyzed, in each one the steam inlet position is changed and for each of these cases, five variations were made, changing the velocity, outlet pressure and water vapor concentration.

Since the elbow is almost in a vertical way, the gases entry is in a vertical way as well. For this reason, it was decided to name the inlets of Figure 2-5 as right inlet of the duct (Inlet #3), middle inlet (Inlet #2) and left inlet (Inlet #1). Figure 2-9 represents these three main cases where it can be seen for Case #1 the steam (water vapor) enters by the right inlet, for Case #2 it does by the middle inlet and for Case #3 it does by the left inlet. Looking from below all the inlets.

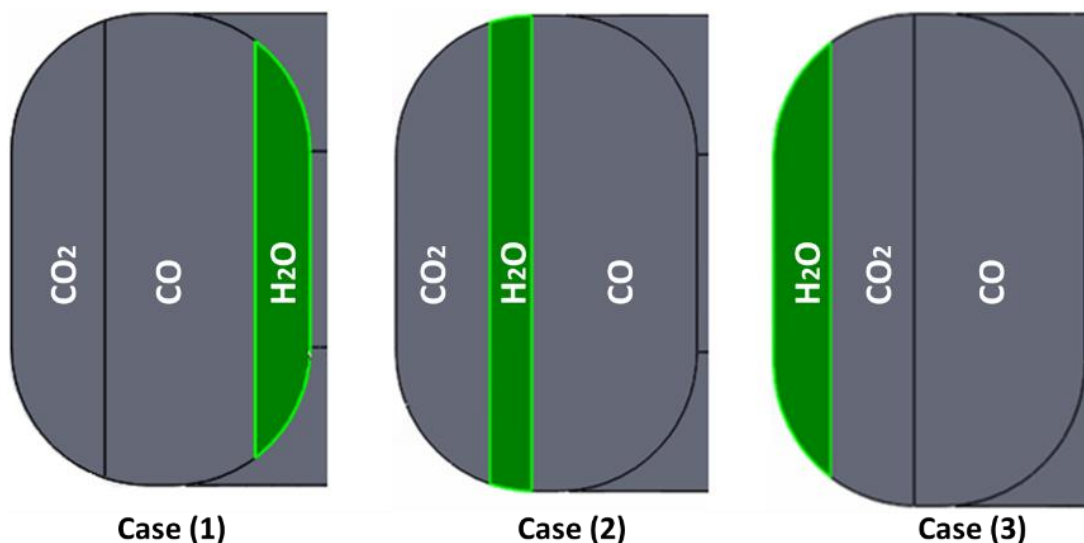


Figure 2-9. Representation of the main cases, indicating the steam inlets.

The performed variations for each case were:

- With gases velocity in the inlets at 6 m/s, 5% of H₂O concentration.

- With gases velocity in the inlets at 12 m/s, 5% of H₂O concentration.
- With gases velocity in the inlets at 25 m/s, 5% of H₂O concentration.
- With 15% of H₂O concentration and gases with a velocity of 12 m/s.
- With a pressure of -101325 Pa in the outlet, 5% of H₂O concentration and gases with a velocity of 12 m/s.

It is good to mention that the air velocity depends on its mass flow and on the other gases mass flow rates, remembering that the air mass flow is the 44% of the sum of all the mass flow rates.

When the steam concentration changes to 15%, the designated inlet area for this gas increments and the ones for CO₂ and CO decrement. So, the Figure 2-9 changes and the area for the steam inlet will look like Figure 2-10. Varying the velocities does not affect the inlets areas.

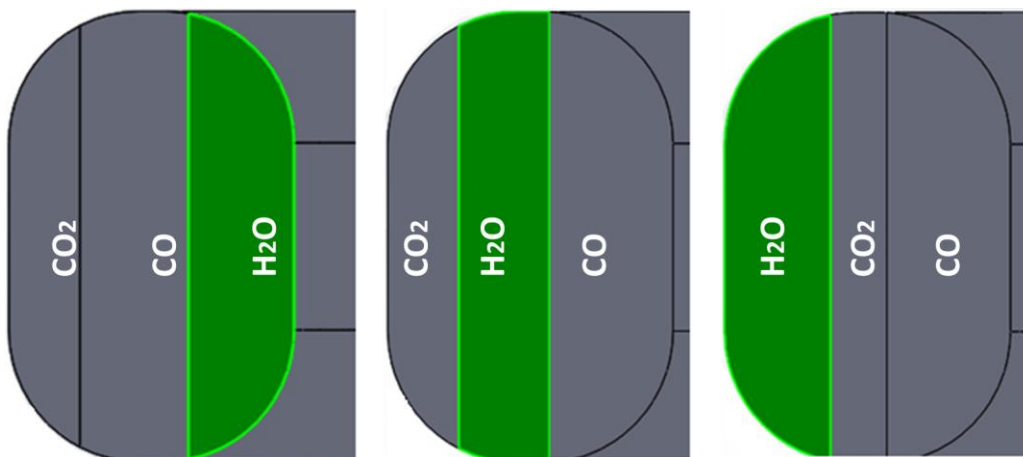


Figure 2-10. Gases inlets when 15% of steam concentration is set.

To find the area for each inlet, these were in function of its mass flow rates, densities and velocities. The velocity is the same for each inlet and densities depends of the equation of ideal gases presented in section 2.3.1. It was necessary to find the relation of mass flow, so the sum of the areas was equal to the total area of the three main inlets (CO, CO₂ and H₂O). The air inlet area does not change, so its mass flow

depends on the relation it has with the other mass flow rates. These calculations were made using EES software with next equations (4-10):

$$A_T = A_1 + A_2 + A_3 \quad (4)$$

$$\dot{m}_{CO} = \frac{28}{23} \dot{m}_{CO_2} \quad (5)$$

$$\dot{m}_{H_2O} = 5 \frac{3}{23} \dot{m}_{CO_2} \quad (6)$$

$$\dot{m}_{air} = \frac{44}{23} \dot{m}_{CO_2} \quad (7)$$

$$\dot{m}_{CO_2} = \rho_{CO_2} * v * A_1 \quad (8)$$

$$\dot{m}_{CO} = \rho_{CO} * v * A_2 \quad (9)$$

$$\dot{m}_{H_2O} = \rho_{H_2O} * v * A_3 \quad (10)$$

A_T is the total area and it is 3.9732464 m², \dot{m} is the mass flow rate for each gas, ρ is the density for each gas and v is the velocity.

2.5 Results

The results show the maximum concentration of steam that flows within the off-gas duct after the air gaps and they are compared with the concentration that gas detector probe would measure. Typically, the gas probes are collocated in the center of the duct just after the air gaps, as it is seen in Figure 2-11.

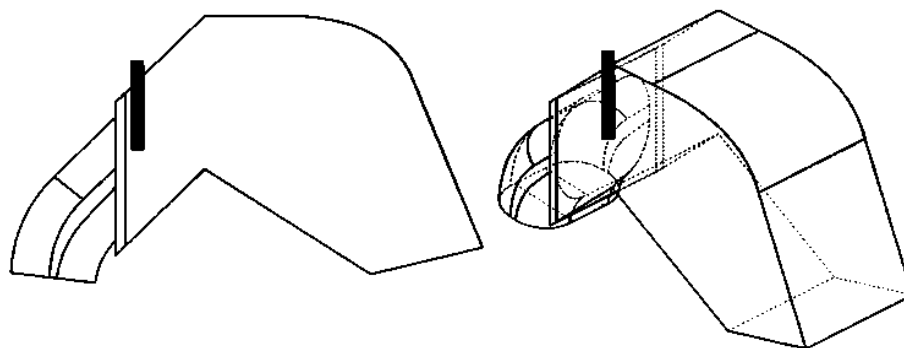


Figure 2-11. Gas detector probe collocation.

2.5.1 Steam entering by right inlet (Case #1)

The inlets for the CO₂, CO and H₂O gases were set at 6 m/s, 12 m/s and 25 m/s. In order to accomplish the concentrations of Figure 2-4 with a concentration of 5% in water vapor, doing the calculation of equations (4-10) the following areas were obtained:

- $Area_{CO_2} = 1.154 \text{ m}^2$
- $Area_{CO} = 2.207 \text{ m}^2$
- $Area_{H_2O} = 0.6127 \text{ m}^2$

These áreas don't change if a gas changes its entry position, in any of the three inlets, the area is going to be same even if the velocities of the gases changes. The only way the areas change is when the steam concentration changes to 15% and those areas are:

- $Area_{CO_2} = 0.8818 \text{ m}^2$
- $Area_{CO} = 1.687 \text{ m}^2$
- $Area_{H_2O} = 1.405 \text{ m}^2$

The mass flow rates do change when different velocities and concentration are set. When the steam enters by the right inlet, the Table 2-1 indicates the mass flow for

each case variation. The mass flow does not change when the pressure at the outlet is changed.

Table 2-1. Mass flow rates for each variation when steam enters by right inlet.

Velocity	6 m/s	12 m/s	25 m/s	H2O 15% at 12m/s
\dot{m}_{CO_2} (kg/s)	3.494	6.989	14.56	5.341
\dot{m}_{CO} (kg/s)	4.254	8.508	17.72	6.502
\dot{m}_{H_2O} (kg/s)	0.7596	1.519	3.165	3.483
\dot{m}_{air} (kg/s)	6.685	13.37	27.85	10.22

The Figure 2-12 shows the velocity contour the gases have when they enter with a velocity of 6 m/s, this contour is very similar when the velocity changes to 12 m/s or 25 m/s. Changing only the velocities magnitude.

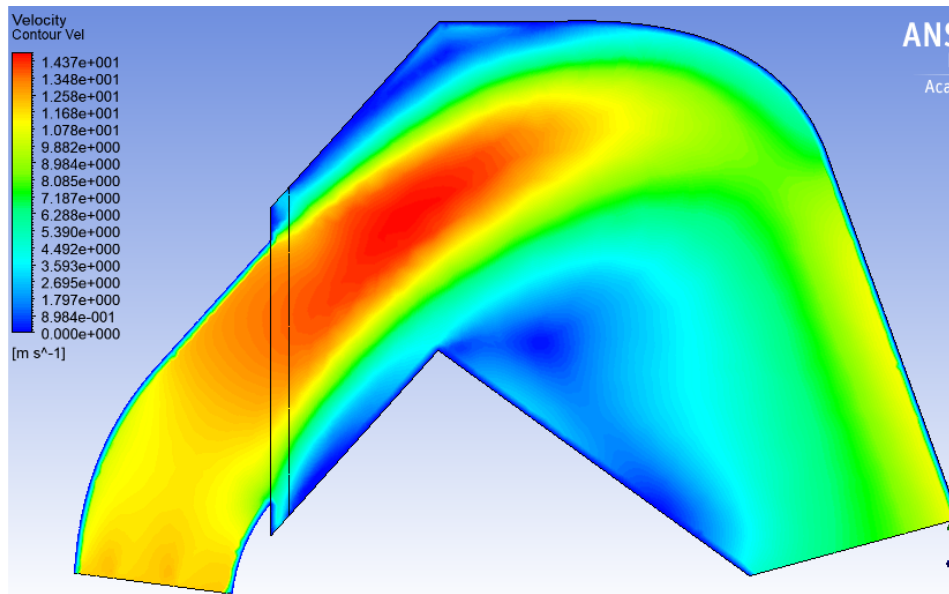


Figure 2-12. Velocity contour when steam enters by right inlet at 6 m/s.

In Figure 2-13 it is shown the mass fraction contour for steam (water vapor) in the X-Y plane when the three main gases enter with a velocity of 6 m/s. This contour shows the path the steam takes within the duct. It is pretty similar for each variation of this case.

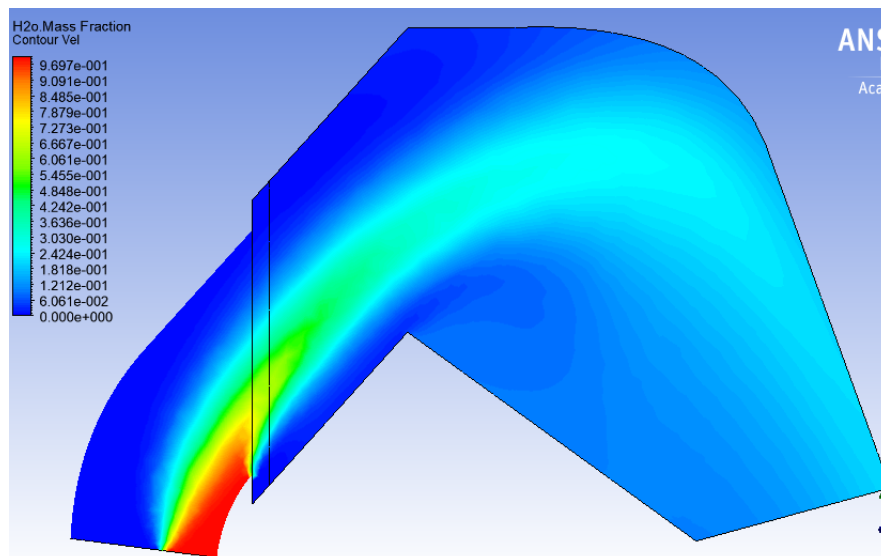


Figure 2-13. Typical mass fraction contour of case #1.

The compared measurements were made in the Y-Z plane that is after the air gaps, as shown in Figure 2-14. The maximum concentrations were compared versus the ones that were found in the probe position. The Figure 2-15 and Figure 2-16 show the position and concentration of the line where exist the higher steam concentration and the concentration for the probe. For this case the line where the probe would be collocated is the one with a highest position (from the center of the duct) and the one with maximum concentration is the one placed in the lowest part of the duct. The Figure 2-16 shows a comparison of the concentration when the gases enter at 6 m/s and the curver with a higher slope is the one with the maximum concentration.

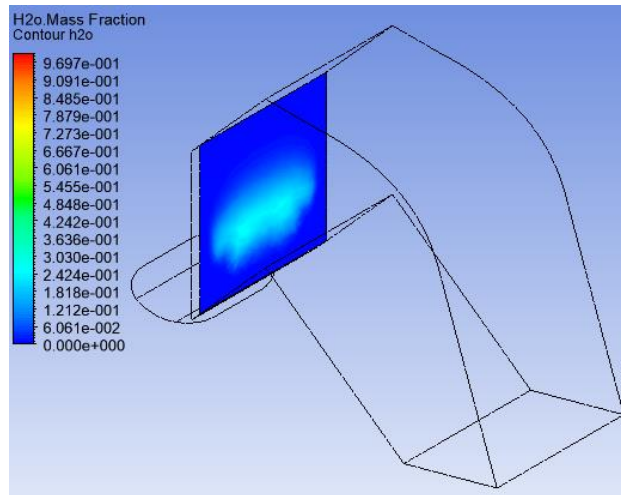


Figure 2-14. Mass concentration plane for case #1, when velocity is 6 m/s.

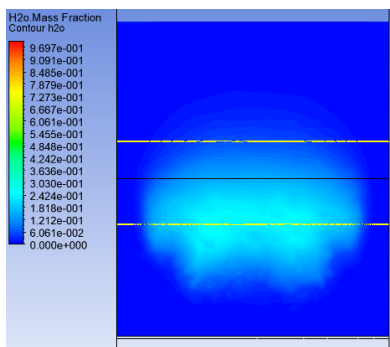


Figure 2-15. Lines of concentration for case #1, when velocity is 6 m/s.

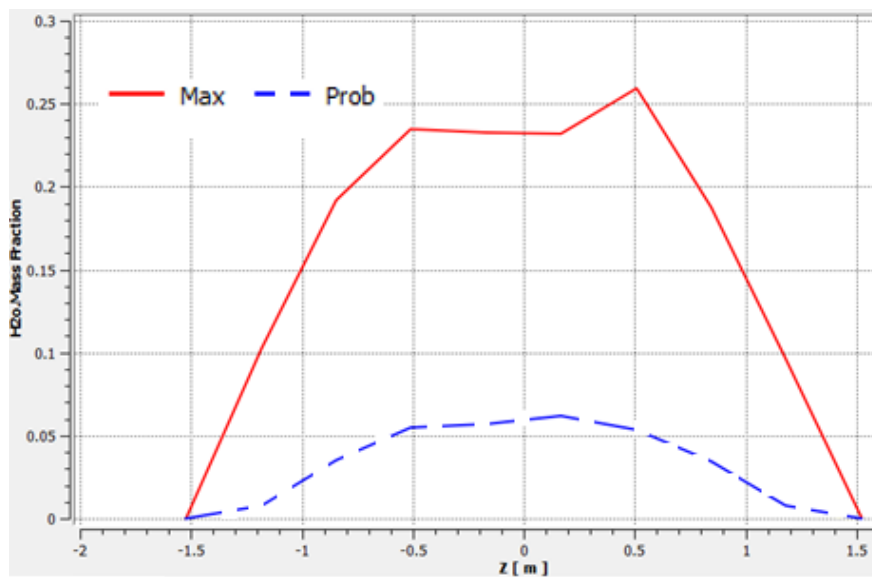


Figure 2-16. Mass fraction in the maximum and probe lines along Z axis for case #1.

All the results when the steam enters by the right inlet were analyzed and summarized in Table 2-2, which indicates the concentration the probe would measure, the maximum concentration that can be measured, the height of maximum concentration, the distances in Z axis with higher concentration and the relation of both concentrations.

Table 2-2. Results when steam enters by the right inlet.

Studied factor	Result	Probe conc.	Maximum conc.	Maximum height conc. (m)	Maximum conc. Z1 (m)	Maximum conc. Z2 (m)	Max/Probe
5% concentration with P= 0 Pa in the outlet	6 m/s	0.065	0.26	-1	-0.5	0.5	4.00
	12 m/s	0.035	0.33	-1.35	-0.2	0.5	9.43
	25 m/s	0.03	0.36	-1.35	-0.2	0.5	12.00
More steam with 12 m/s and 0 Pa	15%	0.15	0.65	-1.2	0.15	0.5	4.33
Less pressure with 5% and 12 m/s	-101325 Pa	0.035	0.33	-1.3	-0.2	0.5	9.43
Average		0.063	0.386	-1.24	-0.19	0.5	

2.5.2 Steam entering by middle inlet (Case #2)

The same areas and mass flow rates of section 2.5.1 are used, but with different gases positions. The gases enter through the duct in following order (from left to right): CO₂, H₂O and CO.

The velocities contour is pretty similar to the presented in section 2.5.1 because the gases enter at the same velocities: 6m/s, 12 m/s or 25 m/s. But the steam fraction within the duct does change its position and this can be seen in Figure 2-17, that show the steam mass fraction in the X-Y plane.

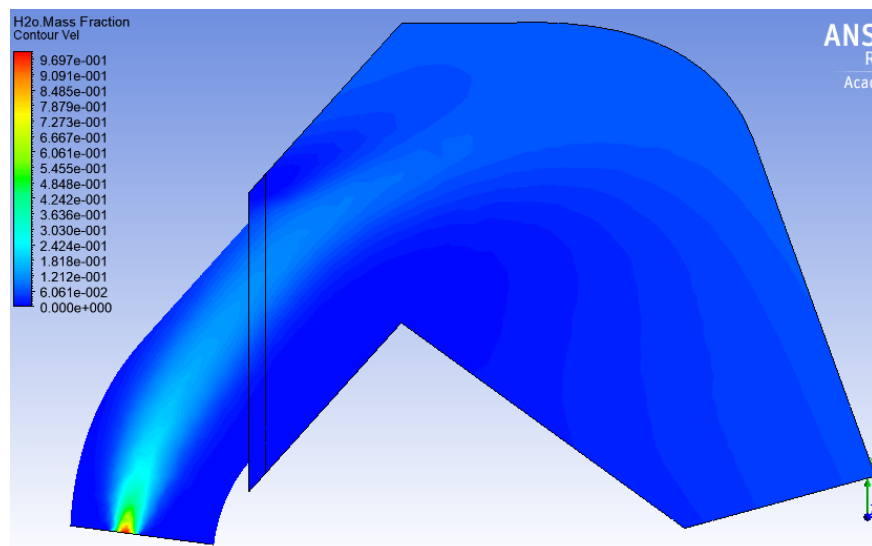


Figure 2-17. Typical mass fraction contour of case #2.

In this test maximum mass fraction values were also compared with the values that gas detector probe would measure. The concentration lines are practically spliced each other, what means that the position with a higher concentration matches with the height of the probe line. This can be observed in Figure 2-18, that shows the concentration line in Y-Z plane after the air inlet.

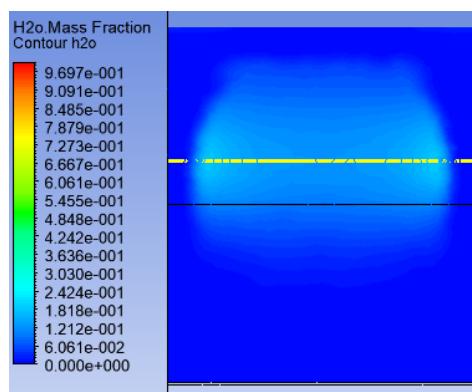


Figure 2-18. Lines of concentration for case #2, when velocity is 6 m/s.

All the results when the steam enters by the middle inlet were analyzed and summarized in Table 2-3.

Table 2-3. Results when steam enters by the middle inlet.

Studied factor	Result		Maximum height conc. (m)	Maximum conc. Z1 (m)	Maximum conc. Z2 (m)	Max/Probe	
	Probe conc.	Maximum m conc.					
5% concentration with P= 0 Pa in the outlet	6 m/s	0.115	0.165	-0.05	-1.2	1.2	1.43
	12 m/s	0.125	0.155	-0.05	-1.2	1.2	1.24
	25 m/s	0.135	0.15	0	-1.2	0.8	1.11
More steam with 12 m/s and 0 Pa	15%	0.33	0.44	-0.15	-1.2	1.2	1.33
Less pressure with 5% and 12 m/s	-101325 Pa	0.13	0.155	-0.05	-1.2	1.2	1.19
Average		0.167	0.213	-0.06	-1.2	1.12	

2.5.3 Steam entering by left inlet (Case #3).

The same areas and mass flow rates of section 2.5.1 are used, but with different gases positions. The gases enter through the duct in following order (from left to right): H₂O, CO₂ and CO.

The steam now enters by the left side of the duct elbow (looking from X-Y plane) and this can be observed in Figure 2-19. All the case variations have similar mass fraction contours in the X-Y plane.

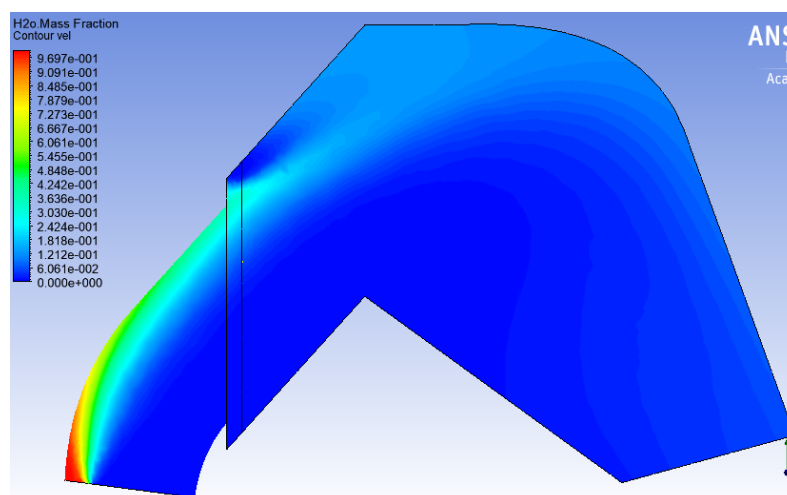


Figure 2-19. Typical mass fraction contour of case #3.

For all the case variations, the lines with a higher concentration in the Y-Z plane were presented in the duct upper zone as shown in Figure 2-20. The Figure 2-21

shows in a graphic way the difference between both concentration lines (maximum line and probe line).

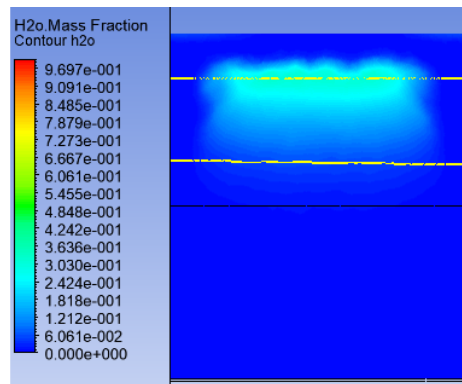


Figure 2-20. Lines of concentration for case #3, when velocity is 6 m/s

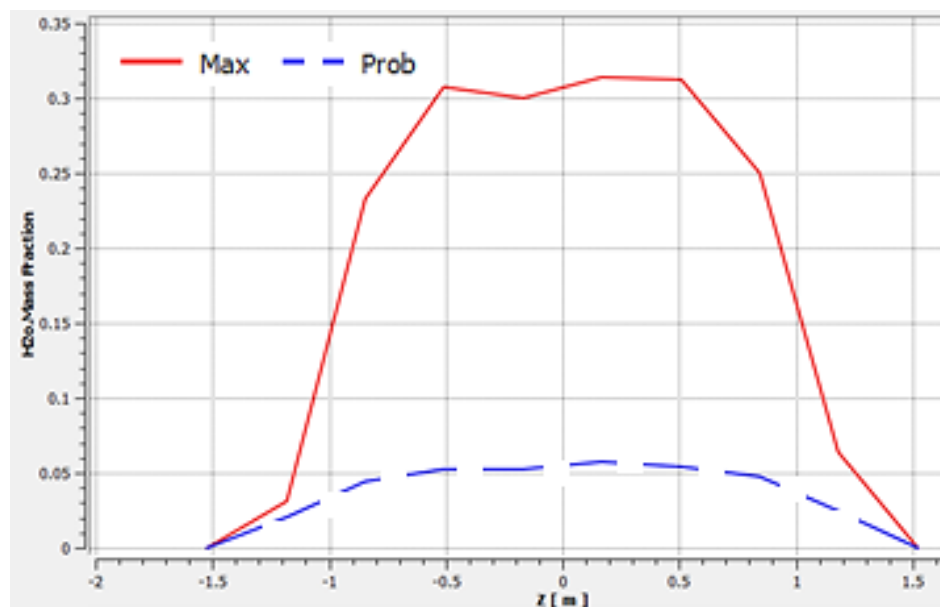


Figure 2-21. Mass fraction in the maximum and probe lines along Z axis for case #3

All the results when the steam enters by the left inlet were analyzed and summarized in Table 2-4.

Table 2-4. Results when steam enters by the left inlet.

Studied factor	Result		Maximum height conc. (m)	Maximum conc. Z1 (m)	Maximum conc. Z2 (m)	Max/Probe	
	Probe conc.	Maximum conc.					
5% concentration with P= 0 Pa in the outlet	6 m/s	0.06	0.32	0.8	0.15	0.5	5.33
	12 m/s	0.08	0.335	0.83	-0.5	0.15	4.19
	25 m/s	0.085	0.34	0.8	-0.5	0.2	4.00
More steam with 12 m/s and 0 Pa	15%	0.25	0.72	0.85	-0.5	0.2	2.88
Less pressure with 5% and 12 m/s	-101325 Pa	0.08	0.335	0.81	-0.5	0.2	4.19
Average		0.111	0.41	0.818	-0.37	0.25	

2.5.4 Uniformly mixed gases.

A simulation with uniform mixing of gases was performed to observe if channeling of gases exists for this case. Concentrations were 23% for CO₂, 28% for CO and 5% for steam. All these three gases entered with a velocity of 12 m/s. The velocities contour of Figure 2-22 was obtained.

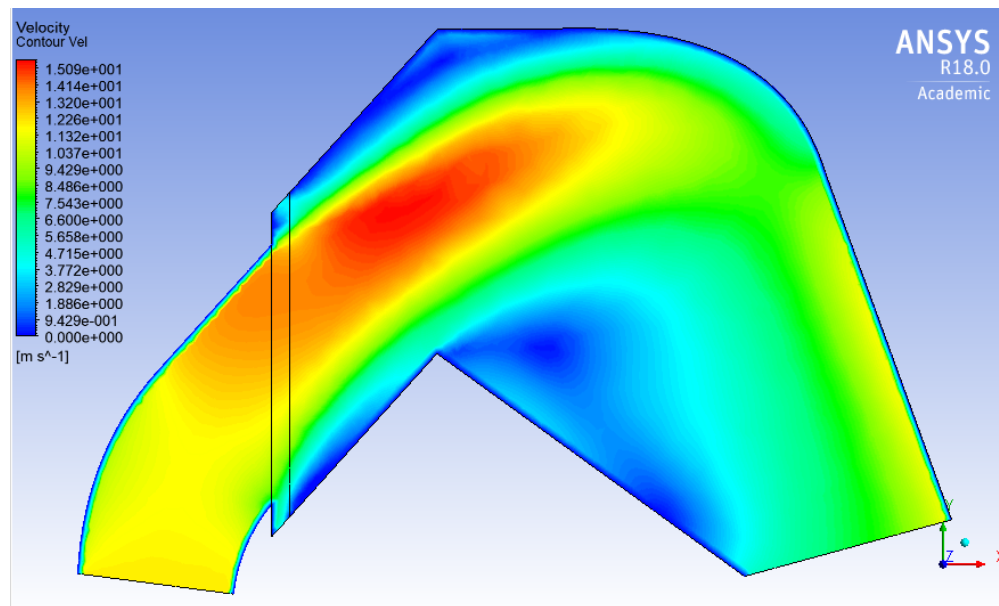
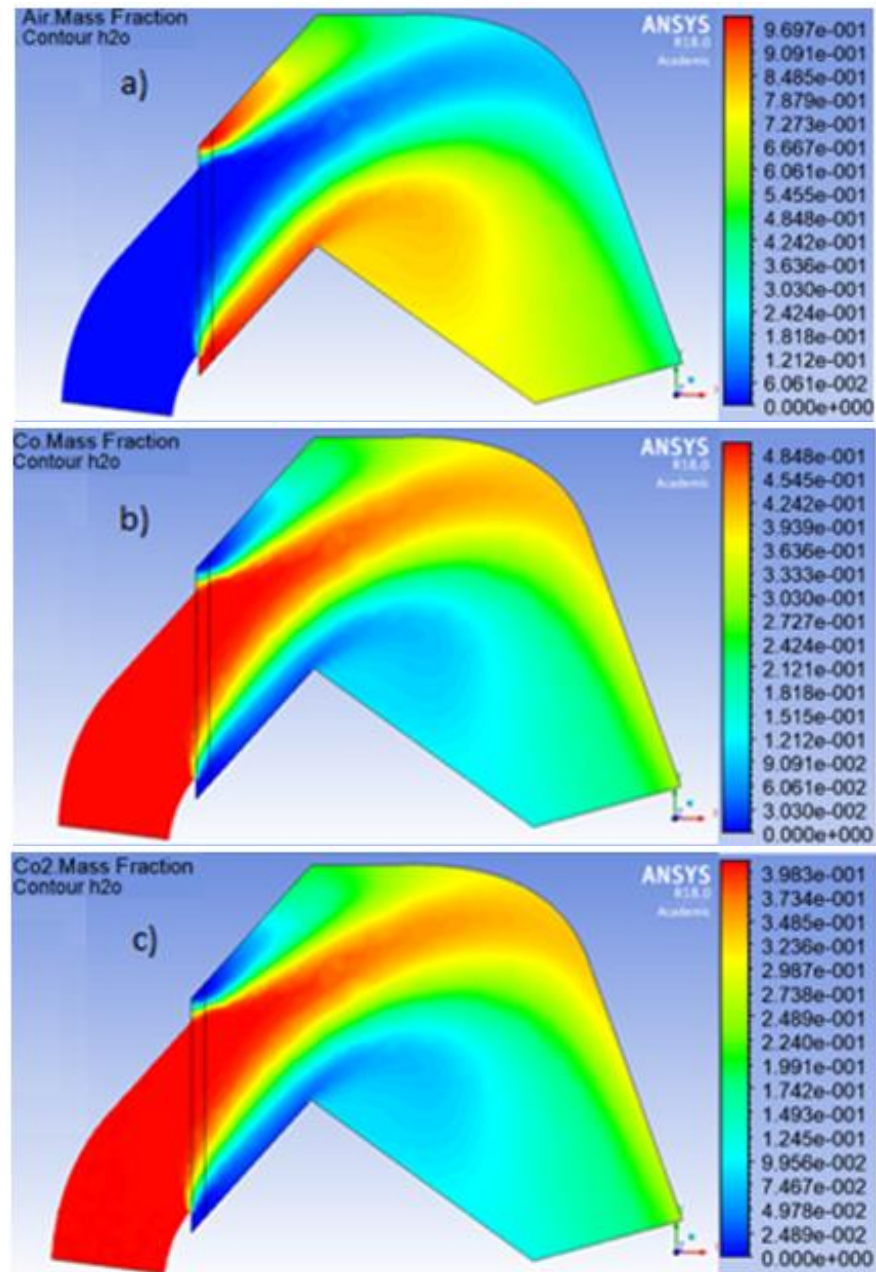


Figure 2-22. Velocities contour when the gases are uniformly mixed.

Figure 2-23 shows the concentration of the four used gases in the simulation, where initially CO_2 , CO and H_2O are mixed uniformly. Meanwhile the air enters by the gaps after the elbow.



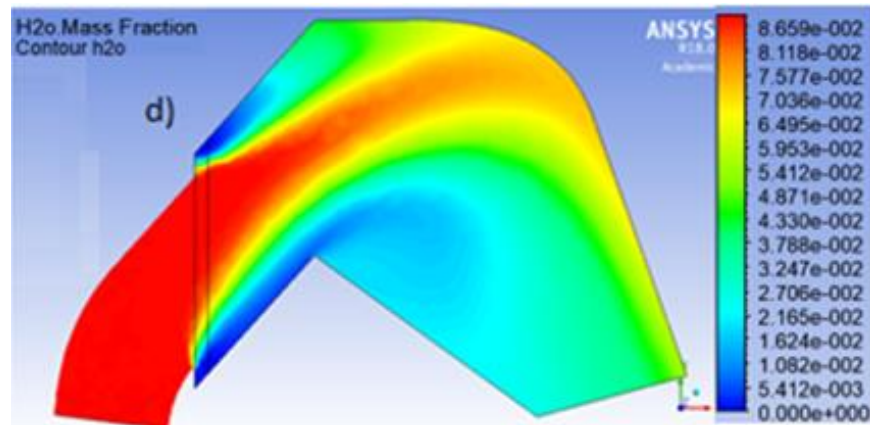


Figure 2-23. a) Air mass fraction, b) CO mass fraction, c) CO₂ mass fraction, d) H₂O mass fraction.

Steam concentration was analyzed to find channeling. It can be said that the air the enters pushes the other gases to the central zone of the duct, but they still remain uniformly mixed. Figure 2-24 shows the steam concentration in Y-Z plane after the air inlet, it can be observed that the steam concentration is the same, about 8% in the center of the duct. This concentration increased a bit from 5% because the air pushes the other gases to the center as well, so it increased in that point. Figure 2-25 shows the concentration values of the line that crosses the center of the duct.

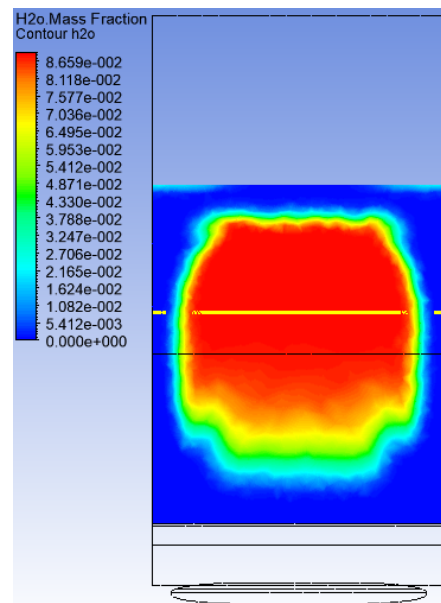


Figure 2-24. Mass fraction contour when all the gases are mixed.

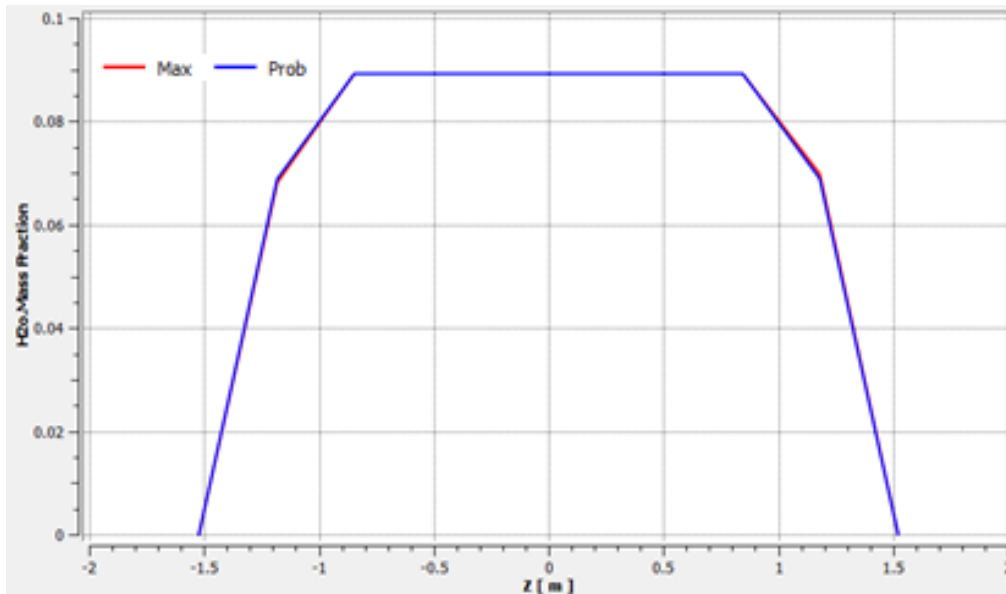


Figure 2-25. Steam mass fraction in the maximum and probe lines along Z axis when the gases are uniformly mixed.

2.6 Discussion and Conclusions

From the results and averages that were obtained when the steam enters by the right inlet of the duct, it was observed that the highest concentration of steam is 1.2 meters below the center of the duct. If a probe at that height and 0.5 meters from the center in the Z axis, it would have a measurement 4 times higher than the original position of the probe (Center in Y height and center in Z axis).

When the steam enters by the middle inlet of the duct, this gas tends to remain in the center of the duct just 0.05 meters below of it. It also tends to go to the edges, so the probe could be placed at the central height and 1.2 meters from the center of Z axis to any direction. This will give at least a 1.2 times higher measurement than the probe could have in its original position.

When the steam enters by the left inlet of the duct, it tends to remain in the upper zone of the duct. 0.8 meter above the center and it tends to stay close from the center of Z axis. So, the probe could be collocated 0.2 meters from the center of Z axis at the

mentioned height and it would have at least a 3 times higher measurement than the probe in its original position.

For lower velocities, the steam tends to go higher in duct. The gases get mixed by the end of the duct.

If it is known the section at the inlet of the duct in which enters the highest amount of steam, the presented results can guide locating the gas probe and provide a better warning of a water leak.

If it could be ascertained that the exhaust gases from the EAF are completely mixed, the gas detector probe could be placed in any section after the air gaps, trying to avoid to be close to the edges and bottom of the duct.

In the off-gases duct it can be said that the steam does not follow a similar path for all the cases, but it does if the steam enters the duct by a specific area.

A general recommendation is to locate the gas detector probe in the center height of the duct but with a separation of 0.75 m from the center of Z axis.

2.7 Future Work

To continue the development of this research topic, we suggest the following:

- Dust particles can be added to the simulations to see how they affect in the path of the steam.
- Real gas properties should be modeled. Also, the gas combustion after the air gaps should be simulated.
- The simulated volume could be extended to reach the molten steel surface in the EAF. This will eliminate the arbitrary assumptions of duct inlet gas concentration and distribution. The presence of water on top of this surface

could then be allowed to vary and the evolution of the gases would determine a more realistic entry condition at the duct.

- It would be desirable to measure the steam concentration in the EAF off-gas duct, to validate the results obtained in the current simulation.

Chapter 3. Numerical Analysis of Molten Metal Fragmentation in Steam Explosions.

3.1 Introduction

One very important problem that the metal industry foundries (p.e. EAF) have are the water steam explosions, they are of real concern where a lot of accidents have been reported resulting in property damage and personal injuries (Bergstroem 1995).

When the detection systems fail large volumes of water can enter the EAF and hazard accidents are caused (P. Dennis 2010). The water is excessively present inside the EAF and it is covered with high-temperature liquid metal (molten steel and/or molten slag) the occurrence of two chemical phenomena is triggered. The increased speed of boiling of water to form steam, and the dissociation of hydrogen from water. These phenomena cause a volumetric expansion that it is fastly pressurized within this "blanket" of steel and/or slag. The disruption of this layer of steel and/or slag creates an explosion without warnings in function of the speed of the reactions (T. P. Wandekoken B. T. Maia 2015). The explosions generated in EAF are unconfined explosions. This kind of explosions typically occur when extremely hot molten metal contacts liquid water.

An unconfined steam explosion is defined as the violent generation of water steam that can surge from incidental contact between a very hot molten metal and liquid water (Eckhoff 2016).

A fuel-coolant interaction (FCI), for this case melt-coolant interaction, is the fast evaporation of coolant, commonly water, due to the heat from fuel. The contact of a coolant with a hot molten metal which is at a temperature is above the boiling temperature of the coolant can generate a vapor explosion (Ciccarelli and Frost 1994).

A vapor explosion involves the fast vapor production as result of the fast heat transfer from the molten metal to the coolant. The high-pressure vapor expansion can produce strong compression waves and accelerate the coolant.

Considering a qualitative description, the one with the internal energy of the stored fuel is converted to produce work by a high-pressure vapor. When molten metal (fuel) and water first come into contact in a typical steam explosion, the water (coolant) begins to vaporize in the fuel-coolant liquid interface when the vapor film separates both liquids. The system remains in non-explosive metastable state during a delay period that varies from few milliseconds up to a few seconds. During this time the fuel and the coolant get mixed due to differences in density and velocity as well as the steam production (Corradini, Kim, and Oh 1988).

After the vapor film destabilization occurs, the fuel fragmentation is triggered. This quickly increases the fuel surface area, vaporizing more coolant and rising the local steam pressure. The “explosive formation of steam” propagates into the fuel-coolant mixture doing the macroscopic region to be pressurized by the coolant steam. Then, the high-pressure coolant steam expands against the inertial surroundings restriction and the mixture itself. The steam explosion is now complete, converting the fuel internal energy into coolant and surroundings kinetic energy. The kinetic energy takes two forms: In preliminary stages shock waves can be generated in the coolant mixture and subsequently, the overall mixture gets accelerated by the expanding coolant steam. High-pressure steam is produced, the dynamic shock waves and the mixture kinetic energy can do the destructive work on the surroundings (Corradini, Kim, and Oh 1988).

Figure 3-1 and Figure 3-2 show the phases of steam explosions (Hyder and Allison 1992). On the basis of experimental observations (Corradini, Kim, and Oh 1988; Cronenberg 1980), it was suggested that a large-scale explosion progresses through four distinct phases (Fletcher and Anderson 1990):

- Premixing. The two fluids inter-penetrate and mix (Figure 3-1b).
- Triggering. Occurs when the hot melt contacts the bottom of the container (vessel) (Figure 3-1c).
- Propagation. The steam film breaks down, and a quantity of superheated steam is generated.
- Expansion. The expansion generates a shock wave that continues the mixing and steam generation (Figure 3-2d). The result is an explosion (Figure 3-2e).

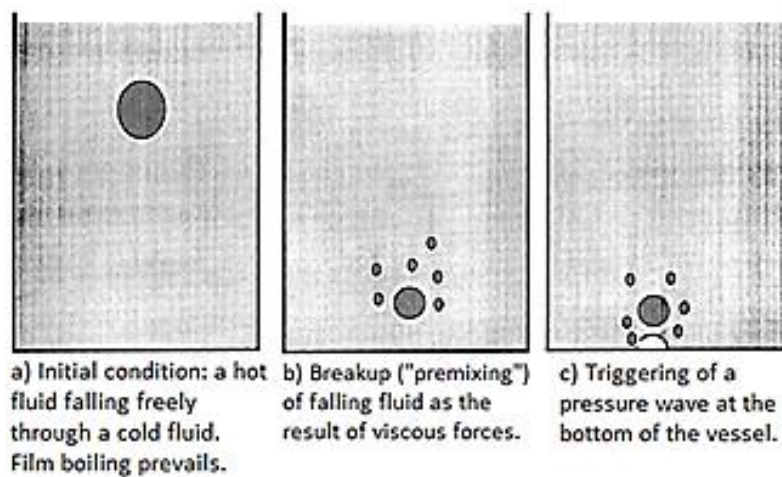


Figure 3-1. Steam explosion phases a) to c). Image taken from (Hyder and Allison 1992).

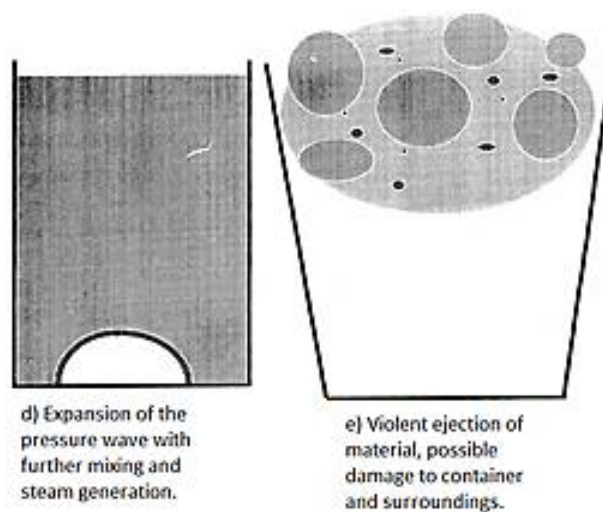


Figure 3-2. Steam explosion phases d) to e). Image taken from (Hyder and Allison 1992).

3.1.1 History of Steam Explosions

As stated by Witte et al. (1970) and (Gilbert 1979) water steam explosion accidents occur periodically in metal production industries. Histories show that destructive forces may be created in this type of explosions. The histories also clarify the type of circumstances that can lead to such accidents. Histories in metallurgical industries are shown.

- Quebec foundry explosion:

45 kg of molten steel fell into a channel that contained 0.35m³ of water. An explosion was resulted and caused one death and injured several others (Eckhoff 2016).

- Armco-steel explosion:

According to (Gilbert 1979) in 1967, an explosion happened when molten steel fell on wet ground. Several tonnes of molten steel fell from 12m, 6 workers died and 24 were injured. Moisture in the porous ground triggered small-scale water steam explosions.

- Water steam explosions in China:

The explosion happened when a stainless-steel casting of a ring had contact with a large sand molding pit. Leakage of ground water into the pit moistened the sand in the pit to an elevated level. The trapped water was heated by the molten stainless steel in the sand mold, a high steam was build up through the sand bed and the mold. The steam pressure increased abruptly and both the sand and molten steel in the casting exploded upwards to at least 5m above the pit (Li and Ji 2016). Figure 3-3 shows the sand mold system that exploded.

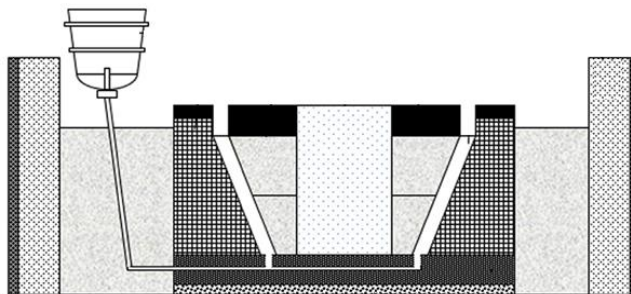


Figure 3-3. Sand mold system and ladle for filling the mold with molten stainless steel (Li and Ji 2016).

3.2 Specific Objective

To analyze by computational simulations how the molten metal fragmentation and formation of melt jets in steam explosions are affected by varying the values of velocity, pressure, density and vapor film thickness depending the case.

3.3 Fragmentation Mechanisms

Fragmentation is the phenomenon that enhances the heat transfer rate in a steam explosion. Fragmentation models have been classified according the source of its driving force or the way that the contact between hot liquid metal and cold liquid is made. The fragmentation mechanisms can be purely caused by hydrodynamic or thermal effects (Corradini, Kim, and Oh 1988).

3.3.1 Hydrodynamic Fragmentation

The fragmentation occurs as result of the acceleration of the molten metal droplet occasioned by the relative velocity with the coolant (water) (Corradini, Kim, and Oh 1988).

The hydrodynamic deformation and droplets breaks depend on the drag and superficial tension also called Weber's number. Witte et al. (1970) indicated the rol

that the Weber number takes part in the process of subdividing the initial large molten metal globel. Weber number is defined in equation (11).

$$We = \frac{\rho_c v_r^2 D_o}{\sigma} \quad (11)$$

Where ρ_c is the coolant density, D_o is the initial diameter of the molten metal droplet, v_r is the relative velocity, σ is the surface tension for both liquids. If Weber number is higher than 10, the forces caused by inertia are going to exceed the surface tension, and the molten metal will break in smaller pieces. Five mechanisms of a molten metal droplet moving in water were defined by Lee and Frost (1987) and Pilch (1979) as observed in Figure 3-4 and Figure 3-5.

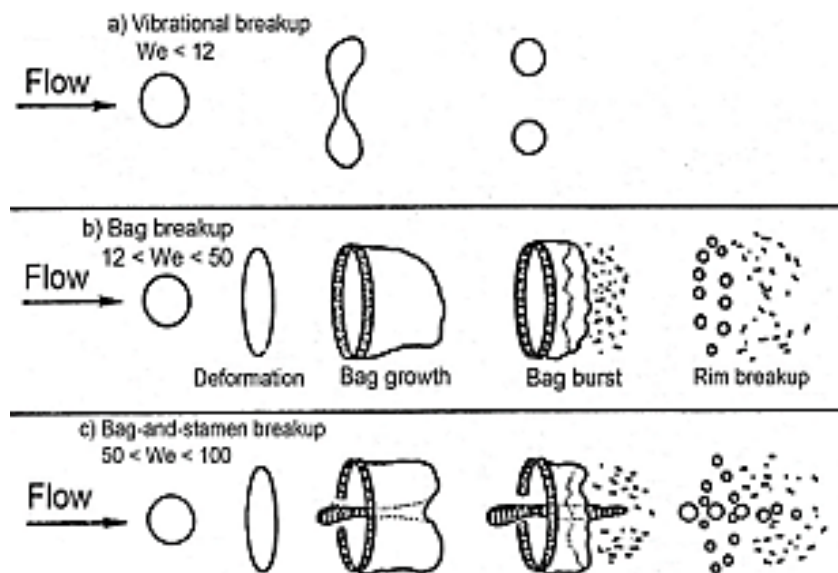


Figure 3-4. a) to c) Schematic illustration of different modes of break-up of large liquid drops into smaller droplets (Lee and Frost 1987; Pilch M. 1979).

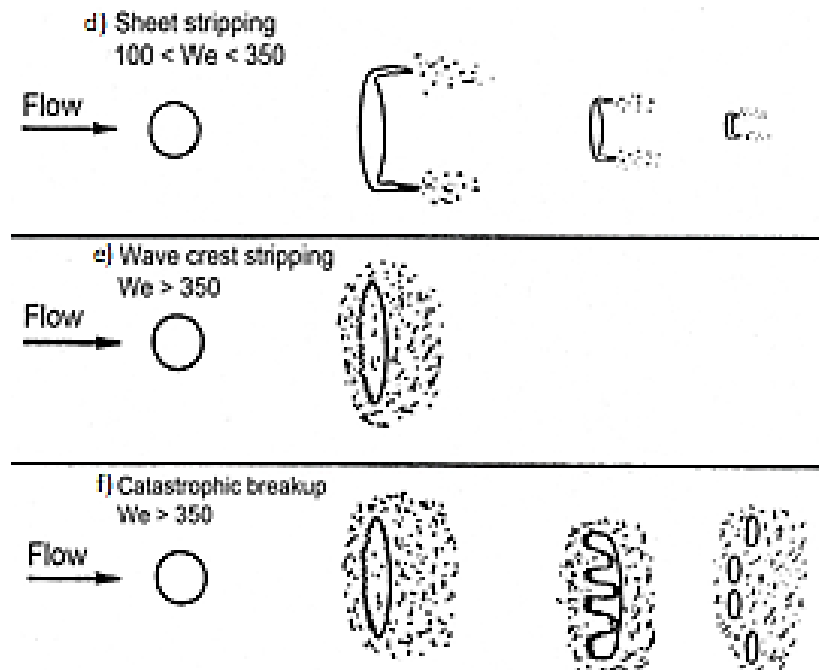


Figure 3-5. d) to f) Schematic illustration of different modes of break-up of large liquid drops into smaller droplets (Lee and Frost 1987; Pilch M. 1979).

Hydrodynamic fragmentation is also related with Rayleigh-Taylor instabilities, Kelvin-Helmholtz instabilities and boundary layer stripping.

The Rayleigh-Taylor instability is a fingering instability of an interface between two fluids of different densities, which occurs when the light fluid is pushing the heavy fluid (Sharp 1984). For the studied problems the interface is the steam film, the heavy fluid is the molten steel and the light fluid is the water. The equation (12) of motion of the interface can be written as (Piriz et al. 2006).

$$\frac{(\rho_2 + \rho_1)}{k} \ddot{\xi} = (\rho_2 - \rho_1) g \xi \quad (12)$$

Where ρ_1 is the density of the light fluid, ρ_2 is the density of the heavy fluid, g is gravity, ξ is a new position and $k = 2\pi/\lambda$ is the wave number and λ is the wave length of the perturbation.

Patel and Theofanous (1981) studied the hydrodynamic fragmentation of metal droplets, they exposed the droplets to a pressure pulse of 600 bar (60 MPa) in a shock tube. They studied the Bond number as the parameter which controls the drop breakup. The Bond number is calculated as:

$$Bo = \frac{\rho_d a_d r_d^2}{\sigma} \quad (13)$$

Where ρ_d , a_d , and r_d are the density, acceleration and radius of the drop. r_d can be changed for wave length value for geometries that are no spherical. And σ is the interfacial tension. The accelartion term in the Bond number (Bo) is specified as:

$$a = \frac{3\rho_c C_D}{8\rho_d r_d} V^2 \quad (14)$$

Where ρ_c is the coolant density, C_D is the drag coefficient, commonly 2.1 for liquid metal droplets in water, and V is the particle velocity behind the shock wave and it is obtained with the measured pressure.

$$\Delta P = \rho V c \quad (15)$$

Where ΔP is the differential pressure in the shock, ρ is the water density, V is the particle velocity and c is the velocity sound in water. Breakup occurs when the drop diameter shows a sudden substantial and continuos increase from its original value. The breakup time can be correlated with the unstable Taylor wave growth given by:

$$\tau_b^* = \tau_b \frac{V}{r_d} = 1.66 Bo^{-\frac{1}{4}} \epsilon^{\frac{1}{2}} \quad (16)$$

Where τ_b^* is the Taylor time constant, τ_b is the breakup time, V is the relative velocity and $\epsilon = \frac{\rho_d}{\rho_c}$.

3.3.2 Thermal Fragmentation

Kim and Corradini (1988) proposed a model where a film boiling occurs around a molten fuel droplet. After film collapses, formed coolant jets penetrate the fuel droplet and get trapped. Rapid evaporation of the trapped water causes the fragmentation of the fuel (Figure 3-6).

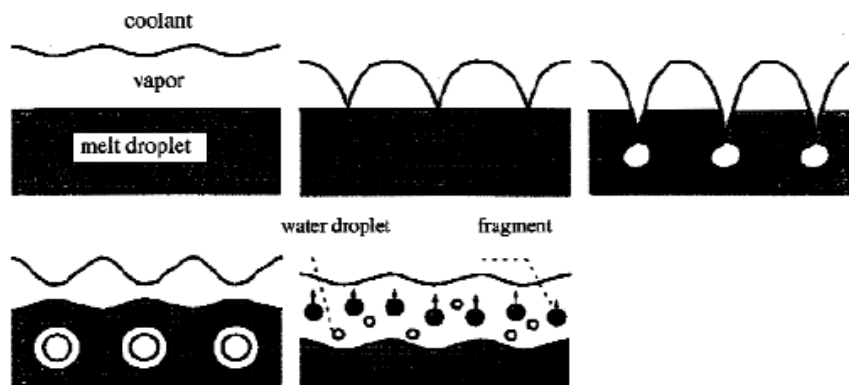


Figure 3-6. Fragmentation mechanism proposed by Kim. Image taken from (Leclerc and Berthoud 2003).

Other kind of mechanism was proposed by Ochiai and Bankoff in their splash theory, where it is assumed that melt fragmentation is due to local pressurization by spontaneous nucleation following liquid-liquid contacts, this mechanism is shown in Figure 3-7 (Leclerc and Berthoud 2003).

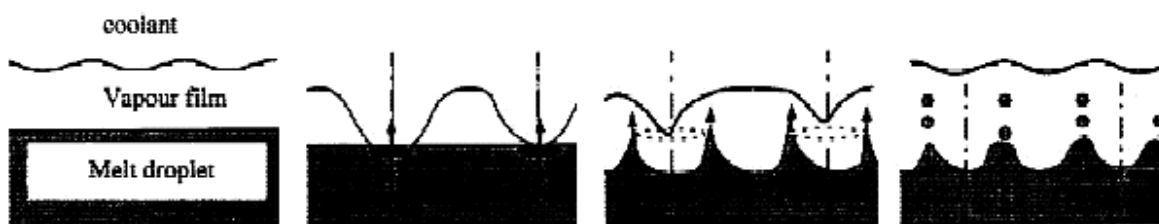


Figure 3-7. Splash theory model. Image taken from (Leclerc and Berthoud 2003).

Very similar to the splash theory, Ciccarelli and Frost (1994) suggested that local generation of high-pressure vapor at the droplet surface causes the formation of a

wave and craters on the droplet surface, giving rise to the formation of melt jets (spikes). See Figure 3-8.

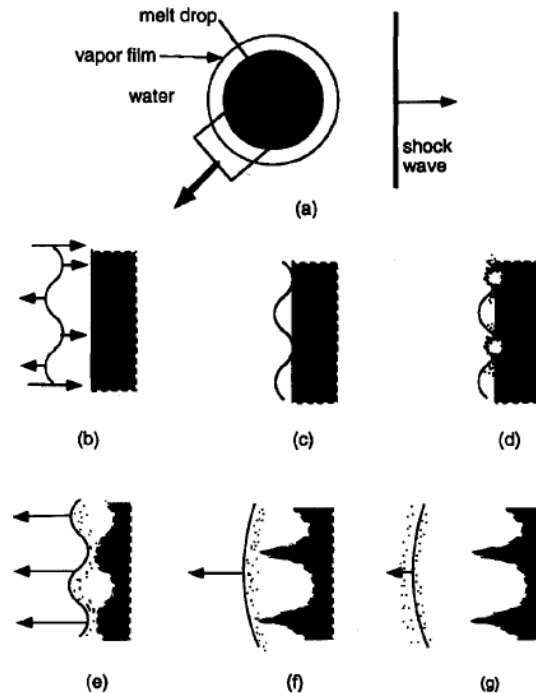


Figure 3-8. Ciccarelli and Frost fragmentation mechanism (Ciccarelli and Frost 1994).

3.4 Simulated Models

Five models are simulated and analyzed with distinct characteristics to determine the most important effects they have. Also, some comparisons of these simulated cases are made versus the original idea of the paper they were taken from.

The five models simulated are:

- Model 1. Formation of melt jets in a stratified water/liquid metal system (thermal).
- Model 2. Melt droplet in water (hydrodynamic).
- Model 3. Melt droplet with vapor film in water (hydrodynamic).
- Model 4. Melt droplet with vapor film in water (thermal).
- Model 5. Water jet falling in molten metal (thermal).

The first simulation “Formation of Melt Jets” is presented with more details like the mesh quality and time-step independence. Because it was the only simulation that had not been performed before, just experimental work was made for this system.

For the other four models the simulation results are good but their meshes were not revised strictly, these models were simulated only to observe if comparable results to the already made simulations by other authors, can be obtained with simple simulations.

The next sections of this subchapter give more details about each simulation model.

3.4.1 Model 1. Formation of Melt Jets

Ciccarelli and Frost (1994) performed several experiments, in a particular one they placed a molten metal droplet inside water and observed the formation of melt spikes in the droplet surface. Regarding this, they suggested that local generation of high-pressure vapor at the droplet surface causes the formation of a wave and craters on the droplet surface, giving rise to the formation of melt jets (spikes). To prove this mechanism, they created a stratified system of melt and water with exploding wires just above melt surface to generate high-pressure vapor and obtain the formation of melt jets.

The apparatus consisted of a narrow channel (5cm wide and 1.2 cm thick) filled to a height of 5 cm with liquid metal with an equal height of water above the metal. A low melting point alloy was used (Wood's metal, 9600 kg/m³ and 70°C for melting point) and the apparatus was heated above the melting point of the alloy with a surface heater. Two exploding wires were placed less than one millimeter above the metal surface in the water and located 2.5 cm apart. The exploding wires were connected in parallel to an 8 μ F capacitor charged to 4 kV and discharged simultaneously,

generating two-line sources of high-pressure vapor just above the liquid metal surface (Ciccarelli and Frost 1994). Figure 3-9 shows the apparatus they used.

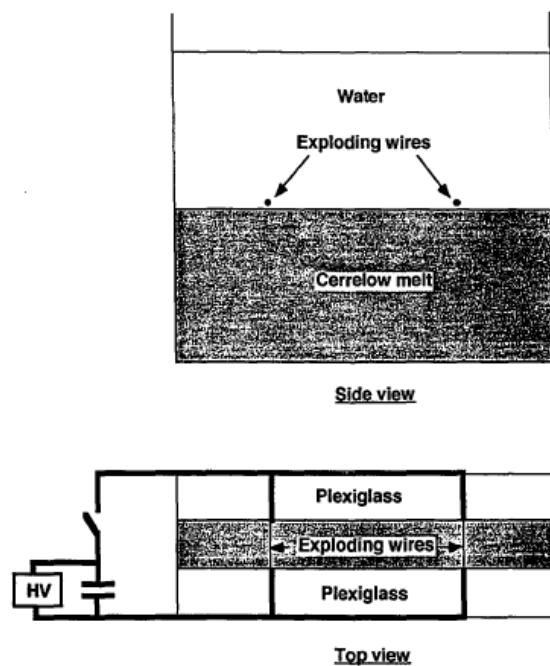


Figure 3-9. Apparatus used in stratified system of melt and water (Ciccarelli 1991).

The Figure 3-10 shows X-ray radiographs at various times, illustrating the growth of wave on the liquid metal surface.

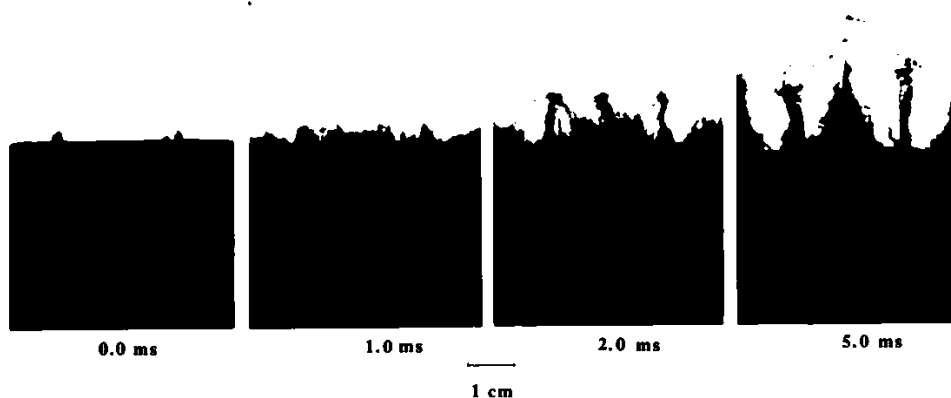


Figure 3-10. Formation of melt jets, obtained by Ciccarelli and Frost (1994).

This simulation is dedicated to investigating how melt jets are formed in this mechanism when a stratified water/liquid metal system is analyzed.

A computational fluid dynamics (CFD) simulation is carried out using ANSYS Fluent software to study these phenomena by having water above hot liquid metal, a vapor film in between and a pressure pulse in the vapor film.

A 2-D planar simulation in ANSYS Fluent software is executed. The 2-D simulations can still capture the fragmentation phenomena with a less computational effort. Standard k-ε model is used because the results with this model are similar to the experimental results in a qualitative way. The transient flow solver is used to simulate the 2-D flow.

Three fluids are present in a steam explosion system which are the liquid coolant, vapor and melt. For each fluid, continuity, momentum, and energy equations (17-20) are presented.

Continuity equation:

$$\frac{\partial \rho_i \alpha_i}{\partial t} + \frac{\partial \rho_i \alpha_i u_i}{\partial x} + \frac{\partial \rho_i \alpha_i v_i}{\partial y} = \Gamma_i \quad (17)$$

Momentum equation:

$$\begin{aligned} & \frac{\partial \rho_i \alpha_i u_i}{\partial t} + \frac{\partial \rho_i \alpha_i u_i u_i}{\partial x} + \frac{\partial \rho_i \alpha_i u_i v_i}{\partial y} \\ & = \frac{\partial}{\partial x} \left(\mu_i \alpha_i \frac{\partial u_i}{\partial x} \right) + \frac{\partial}{\partial y} \left(\mu_i \alpha_i \frac{\partial u_i}{\partial y} \right) - \alpha_i \frac{\partial p}{\partial x} + \sigma_i k_i \delta_s n_x \end{aligned} \quad (18)$$

$$\begin{aligned} \frac{\partial \rho_i \alpha_i v_i}{\partial t} + \frac{\partial \rho_i \alpha_i v_i u_i}{\partial x} + \frac{\partial \rho_i \alpha_i v_i v_i}{\partial y} \\ = \frac{\partial}{\partial x} \left(\mu_i \alpha_i \frac{\partial v_i}{\partial x} \right) + \frac{\partial}{\partial y} \left(\mu_i \alpha_i \frac{\partial v_i}{\partial y} \right) - \alpha_i \frac{\partial p}{\partial y} + \sigma_i k_i \delta_s n_y \end{aligned} \quad (19)$$

Energy equation:

$$\frac{\partial \rho_i \alpha_i e_i}{\partial t} + \frac{\partial \rho_i \alpha_i u_i e_i}{\partial x} + \frac{\partial \rho_i \alpha_i v_i e_i}{\partial y} = \frac{\partial}{\partial x} \left(\lambda_i \alpha_i \frac{\partial T_i}{\partial x} \right) + \frac{\partial}{\partial y} \left(\lambda_i \alpha_i \frac{\partial T_i}{\partial y} \right) + \Phi_i \quad (20)$$

Where $i=l, v, m$, represent coolant liquid, vapor and liquid metal respectively. α_i is the fractional volume. The term of the surface tension $\sigma_i k_i \delta_s n$ is treated with continuum surface force (CSF) model. The properties in the cell are determined as below:

$$\begin{aligned} \rho &= \sum \alpha_i \rho_i \\ \mu &= \sum \alpha_i \mu_i \\ \lambda &= \sum \alpha_i \lambda_i \\ C_p &= \sum \alpha_i C_{pi} \end{aligned} \quad (21)$$

Molten metal (tin), steam, water, and air are used in the current simulation. Default properties for steam, water, and air are taken from the software meanwhile tin properties are defined by the user. The domain consists of a rectangular shape with three adiabatic walls, one pressure outlet and a stratified system of the mentioned fluids. The domain, as well as the boundary conditions, can be seen in Figure 3-11. No slip boundary condition is specified for walls. Boundary conditions are:

$$T(0 < x < L, 0 < y < L, t = 0) = T_{melt} \quad (22)$$

$$T(0 < x < L, L < y < L + L_v, t = 0) = T_{vap} \quad (23)$$

$$T(0 < x < L, L + L_v < y < H_{tot}, t = 0) = T_{water,air} \quad (24)$$

$$\left. \frac{\partial T}{\partial x} \right|_{x,y=0} = 0 \quad (25)$$

$$\left. \frac{\partial T}{\partial y} \right|_{x=0,y} = 0 \quad (26)$$

$$\left. \frac{\partial T}{\partial y} \right|_{x=L,y} = 0 \quad (27)$$

Where $L = 5 \text{ cm}$, $L_v = 3 \text{ mm}$, $H_{tot} = 13.3 \text{ cm}$, $T_{melt} = 1073 \text{ K}$, $T_{vap} = 374 \text{ K}$ and $T_{water,air} = 373 \text{ K}$.

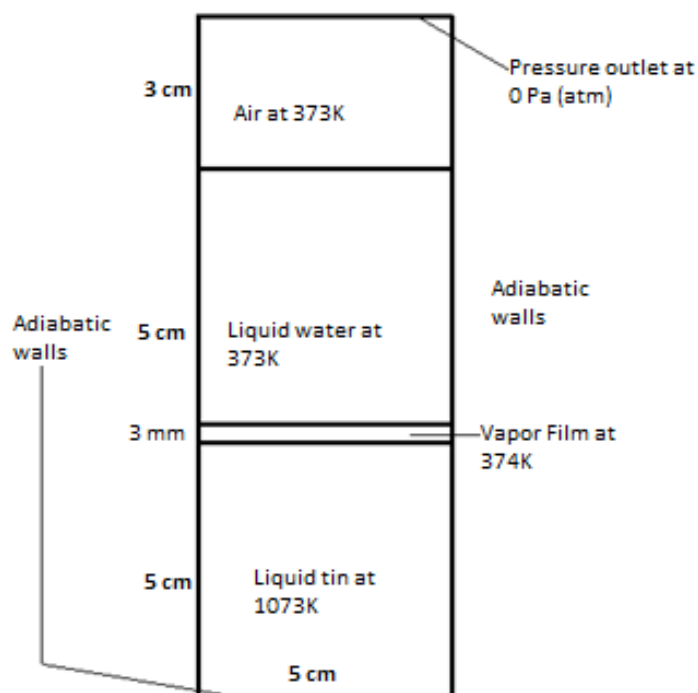


Figure 3-11. Geometry and boundary conditions of the simulated domain (stratified water/liquid metal system).

The volume of fluid method (VOF) is used because it is simple and accurate, this method allows us to track fluid-fluid interfaces. The VOF method is a numerical formulation to track fluid-fluid interfaces (Thakre, Ma, and Li 2013). A unit value of volume fraction α_i would correspond to a cell full of fluid, while a zero value would indicate that the cell contained no fluid. Those cells with a volume fraction α_i between 0 and 1 must contain an interface. The interfaces tracking is made by solving the continuity equation for the volume fraction of one (or more) of the phases. The VOF method has already been successfully used in earlier works (Thakre, Ma, and Li 2013; Zhong et al. 2014; Zhou et al. 2013).

Four phases were defined, one for each fluid. A geo-reconstruct solution scheme for volume fraction is used to track the interfaces. This scheme is recommended when the jet breakup is analyzed with VOF method. SIMPLEC scheme used for pressure-velocity coupling helps in achieving the convergent solution. The evaporation-condensation mechanism is used for the phase change from liquid water to water vapor. Continuum Surface Force model is used in the surface tension model as well as wall adhesion. Surface tension values for the materials, except air which was used as zero, were obtained from (Thakre, Ma, and Li 2013). Table 3-1 lists surface tension values. Pressure pulse in the vapor film is placed with a patch in the initial conditions, the pulse starts from 0 s until 50 μ s. The computations are carried out with a time step of size 10 μ s. Time independence study was performed for time steps of 20 μ s, 15 μ s, and 10 μ s. The spike height for the flow at 0.4 ms is shown in Figure 3-12. The results with three different time steps are matching and the maximum difference in the spike height is less than 3%.

Table 3-1. Surface tensión values.

Phases	Surface tension
Melt-vapor	0.52
Melt-liquid water	0.468
Vapor-liquid water	0.072

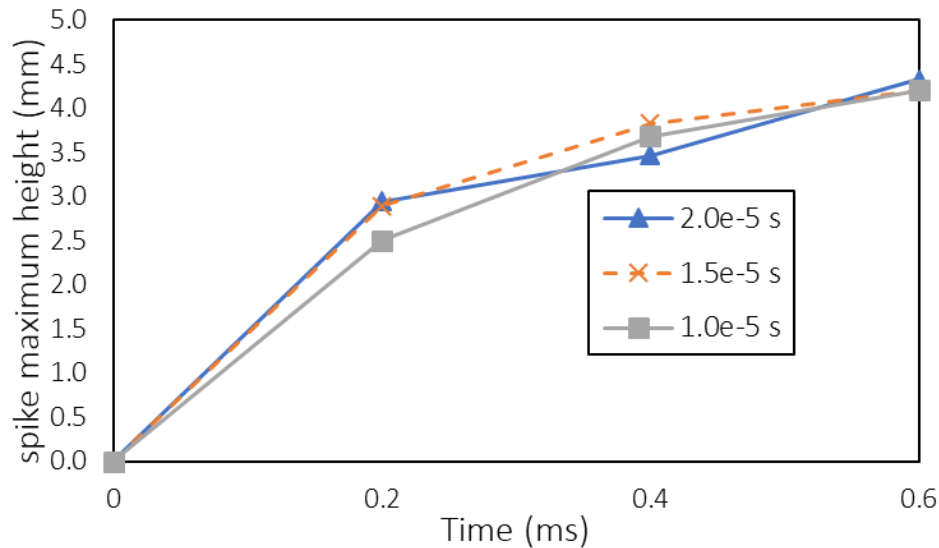


Figure 3-12. Time-step independence study: variation of spike maximum height with the time step size.

In systems with several phases, it is important to capture all the interfaces with a good accuracy. Six different types of meshes were created to study the mesh convergence. And, the number of cells in the vapor film region was increased until similar measures were obtained in the height of the melt spikes versus time. Table 3-2 lists the minimum (a) element length, number of nodes (NN) and number of cells (NE) of various meshes considered for the mesh convergence study.

Table 3-2. Various computational meshes considered for the mesh convergence study.

	a (μm)	NN	NE
Mesh M1	500	7885	7711
Mesh M2	250	10643	10490
Mesh M3	125	21283	21148
Mesh M4	85	21265	21050
Mesh M5	93.75	30681	30579
Mesh M6	62.5	56222	56114

Figure 3-13 illustrates the mesh convergence study with different minimum element sizes, the study was made for a density of 7000 kg/m^3 and 100 MPa . The results with M4, M5, and M6 are similar. Therefore, the mesh M4 was used for the computations.

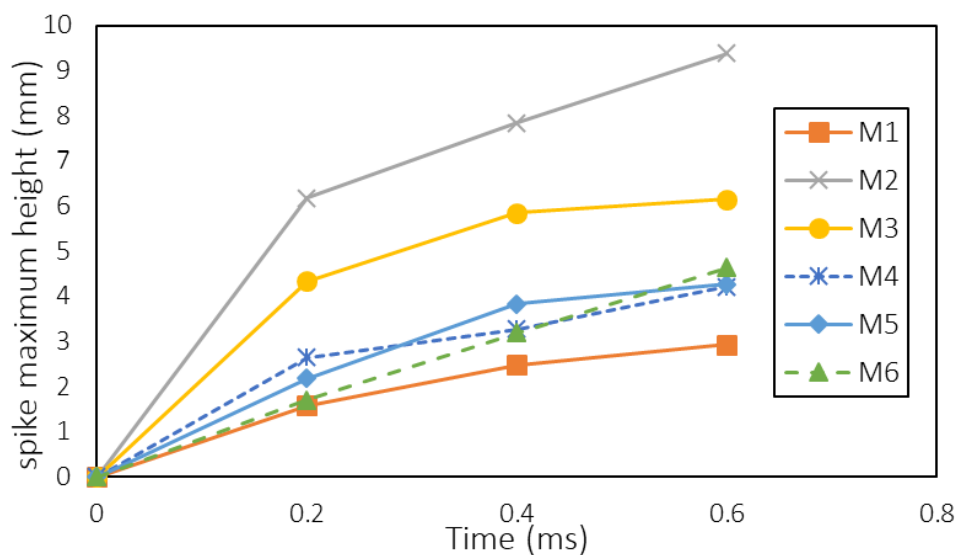


Figure 3-13. Mesh convergence study: variation of spike maximum height with time for different meshes.

In addition, the mesh M4 contains approximately $2/3$ of the number of elements in the mesh M5 and helps us to minimize the computational time.

Convergence in residuals was presented for both meshings, the criteria were $1e-3$ for continuity, velocities and $k-\epsilon$, and $1e-6$ for energy. The mesh M4 had a 3 times faster convergence in residuals. The mesh M4 is shown in Figure 3-14. The average quality of the mesh is 0.8935.

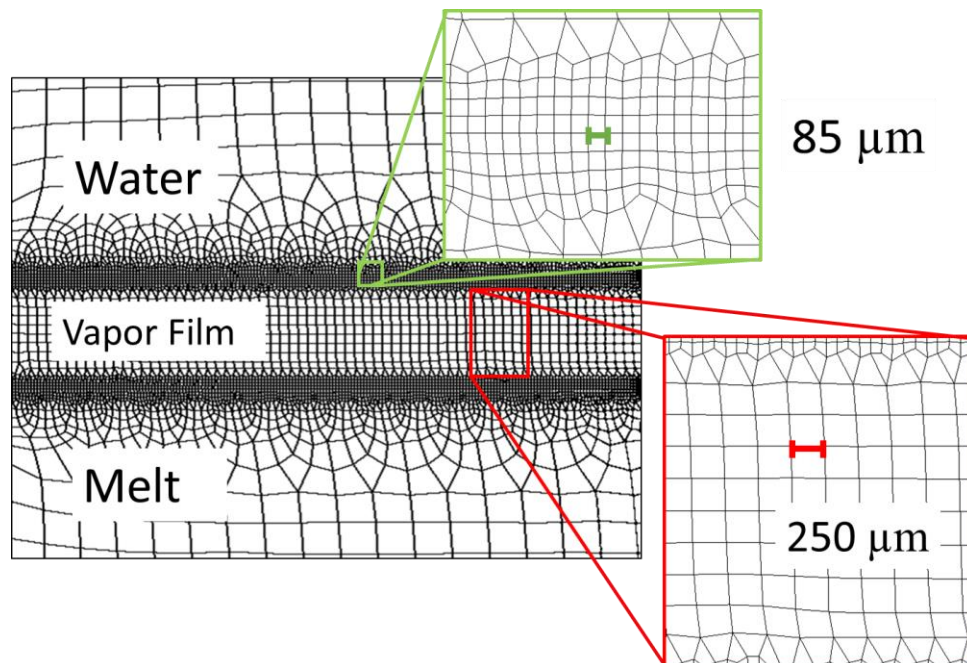


Figure 3-14. The computational mesh M4.

The melt jets (spikes) are measured by using the software Digimizer, a software where a reference length value is given to a certain number of pixels. Figure 3-15 shows a measurement made with Digimizer.

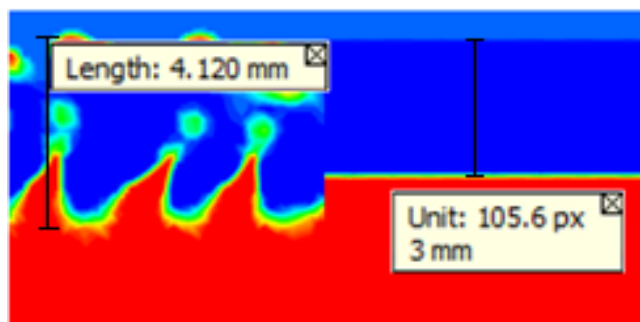


Figure 3-15. Measurement with Digimizer. In the right, reference measure is added indicating the vapor film thickness.

To review if the boundary conditions of adiabatic wall on the left and right walls did not affect the height of the melt spikes, a single test with symmetry in these walls as boundary condition was set. Figure 3-16 shows the results for both boundary conditions overlapped, the spikes in white are the one with adiabatic walls. It is observed, regardless the boundary conditions of the left and right walls, that the spikes height is not affected.

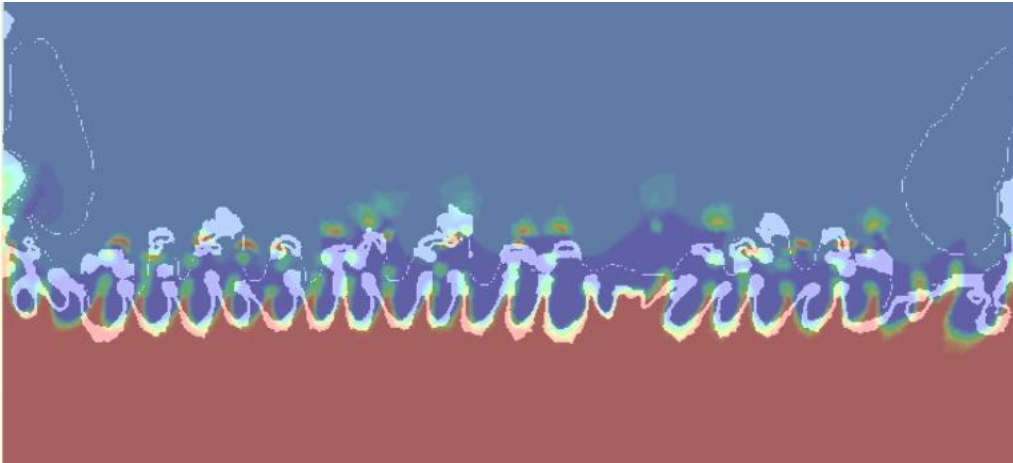


Figure 3-16. Overlapped results for different boundary conditions in the walls.

Once the geometry and necessary setup were made for the 2-D simulation of the stratified water/liquid metal system, measurements of the melt spikes length were obtained and studied.

Figure 3-17 shows the formation sequence of the melt jets through time, they look similar to the results in Ciccarelli and Frost (1994) that were digitally processed in Figure 3-10. Since no measurements for the melt spike length were made in (Ciccarelli and Frost 1994), qualitative agreement is shown only between the results and the simulation.

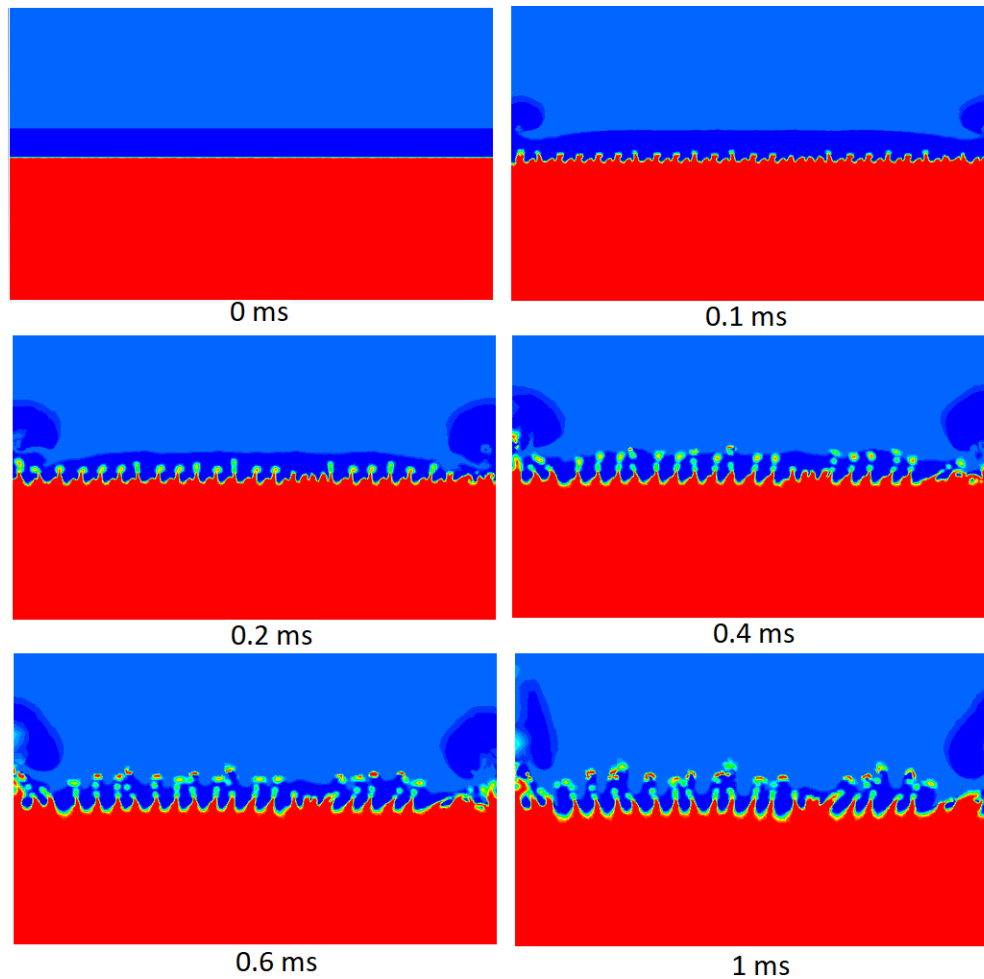


Figure 3-17. Density contours at various time instants for pressure pulse of 100 MPa.

In Figure 3-17, it can be observed that at time= 0 ms the system is at rest and there are no perturbations in the vapor film which is located between the water and liquid tin. The spikes appear in the flow as the time progresses. They grow in the vapor film zone for time ≤ 0.2 ms. After 0.2 ms the melt jets get fragmented for pressure pulse of 100 MPa and the density of the melt of 7000 kg/m^3 . The decrease in the pressure values results in little spikes or ripples of melt for the same density.

Figure 3-18 shows the effect of the melt density at the pressure of 40MPa. It is observed that the increase in density increases the spike height. For density $< 10000 \text{ kg/m}^3$, the spike maximum height does not vary with time. However, the spike height increases with time for $\rho = 10000 \text{ kg/m}^3$.

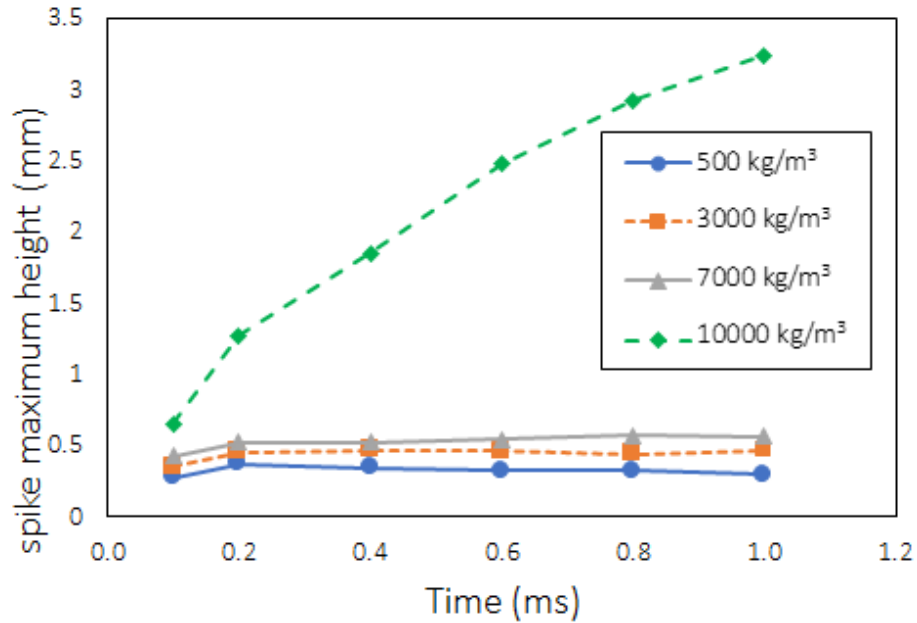


Figure 3-18. Variation of jet length with time for various melt densities when initial pressure is 40 MPa.

Figure 3-19 shows the variation of spike maximum height with time for various initial pressures. For this case, the melt density remained constant at 7000 kg/m³. The melt spikes height increases with an increase in the pressure values.

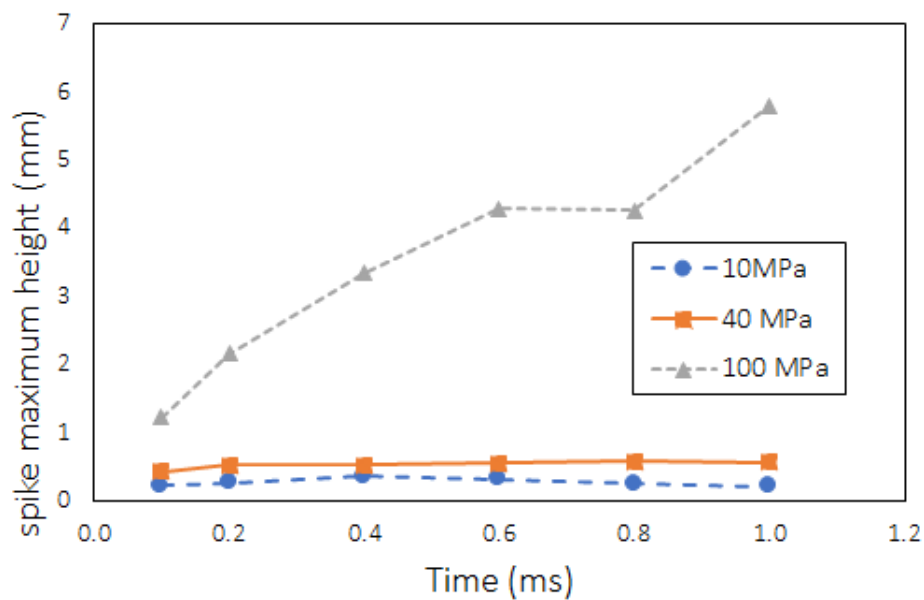


Figure 3-19. Variation of jet length with time for various initial pressures when density is 7000 kg/m³.

The formed craters push the melt upwards. The force that pushes the melt increases with increases in the melt density. This can be seen in Figure 3-20 where two different densities were simulated. Figure 3-21 shows the effect of having different initial pressure values in a qualitative way. It is observed that the increase in initial pressure increases the perturbations around the vapor film and increases the spike height. The increase in the density increases the melt spike height as well.

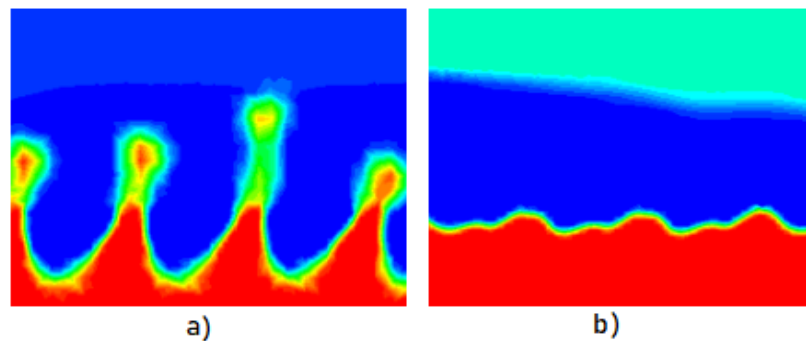


Figure 3-20. Density contour with a pressure of 40 MPa and a density of (a) 10000 kg/m³ and (b) 3000 kg/m³, both at 1 ms.

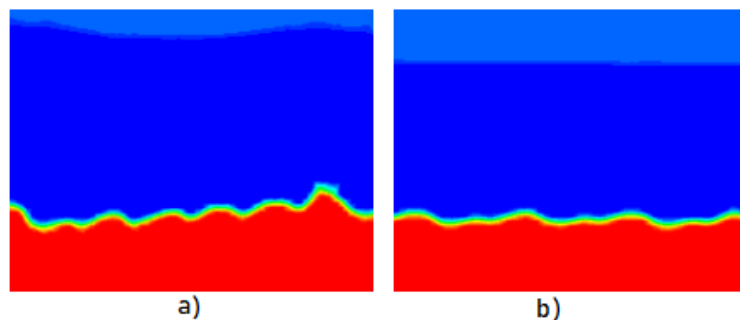


Figure 3-21. Density contour with a density of 7000 kg/m³ and an initial pressure of (a) 40 MPa and (b) 10 MPa, both at 1 ms.

Figure 3-22 shows the variation in the melt jets length when different vapor film thickness is selected. It is observed that the vapor film thickness doesn't affect too much to the melt jets height although when the vapor film is thicker the melt jet length is a little bit longer.

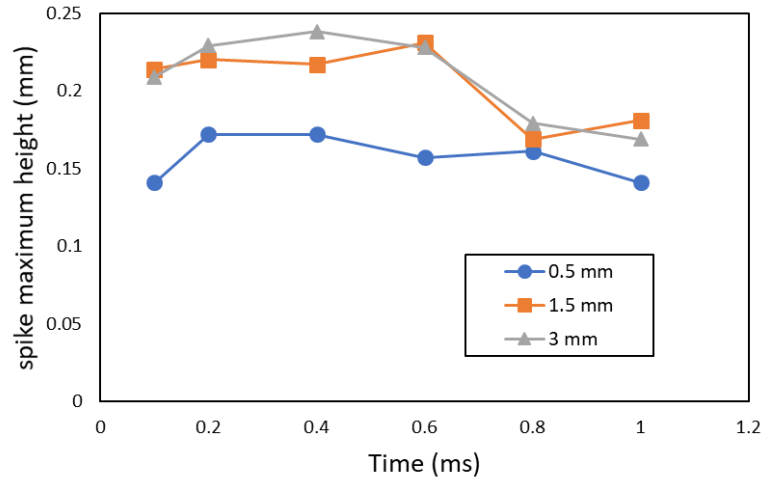


Figure 3-22. Variation of jet length with time for different vapor film thickness when density is 7000 kg/m³ and pressure is 10 MPa.

For this case the relation of the Bond number (Bo) with the formation of melt spikes has been analyzed. The Table 3-3 shows the calculation of bond number and Taylor time constant when the initial pressure in the system is varied when the density is 7000 kg/m³. The wave length was measured from the depth of the formed craters and the obtained results were calculated with equations (13-16) of section 3.3.1.

Table 3-3. Bond number when pressure is varied, and density is 7000 kg/m³.

Pressure (Pa)	L(m)	Wave Length (m)	Bo	Tb*
1.00E+07	2.14E-04	9.00E-05	5.9678	2.8100
4.00E+07	5.68E-04	1.40E-04	148.5324	1.2581
1.00E+08	5.80E-03	1.60E-03	10609.4566	0.4327

It can be observed that for higher pressure values, the deformation will be higher as well as the Bond number will be. It is good to remember that for the first two cases there was no fragmentation of the melt, only for the third one. Fragmentation occurs when the Bond number is near 10^4 for this part of the study. The breakup time adimensional number is lower if the bond number is higher when the density remains constant.

Also, Bond number was calculated when the density is varied for a pressure of 40 MPa, Table 3-4 shows the obtained results.

Table 3-4. Bond number when density is varied, and pressure is 40 MPa.

Density (kg/m ³)	L(m)	Wave Length (m)	Bo	Tb*
5.00E+02	3.00E-04	8.60E-05	91.2413	0.3798
3.00E+03	4.69E-04	1.37E-04	145.3496	0.8281
7.00E+03	5.68E-04	1.40E-04	148.5324	1.2581
1.00E+04	3.24E-03	9.23E-04	979.2528	0.9384

In this case the deformation of the melt spikes is also higher when the Bond number is bigger, but the breakup time adimensional number varies and this happens because the density is also varying.

Since, the calculation of bond number for both cases are consistent, the obtained results of both cases for this number can be combined in only one graph. Figure 3-23 shows how the height of the spikes varies according to the Bond number.

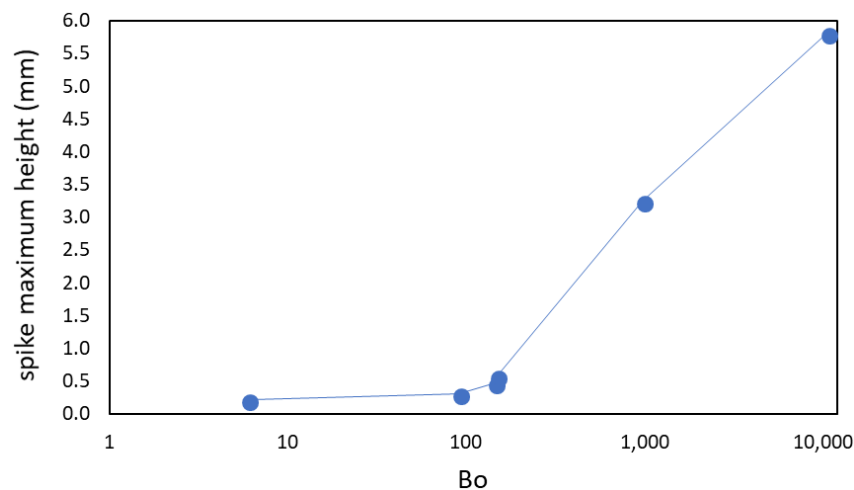


Figure 3-23. Spike height vs Bond number.

In conclusion for both simulated cases varying pressure and density, it can be said that when Bond number is near the value of 100, the deformation of the melt is

significant and when the Bond number is near 1000 the melt fragmentation is observed.

Also Reynolds number, equation (28), and Morton number, equation (29), were calculated to compare the obtained results with the bubble regime from Amaya-Bower and Lee (2010). Through computational simulation they draw a map that according to the Bo, Re and Mo number, a bubble changes its shape. I overlapped my results with the regime they show. Figure 3-24 shows the obtained results for the current simulation and validates that the gotten results have physical sense even though a bubble is not studied. The dotted lines indicate the Morton number for certain Reynolds and Bond numbers.

$$Re = \frac{\rho_l v r_d}{\mu_l} \quad (28)$$

$$Mo = \frac{\alpha_d \Delta \rho \mu_l^4}{\sigma^3 \rho_l} \quad (29)$$

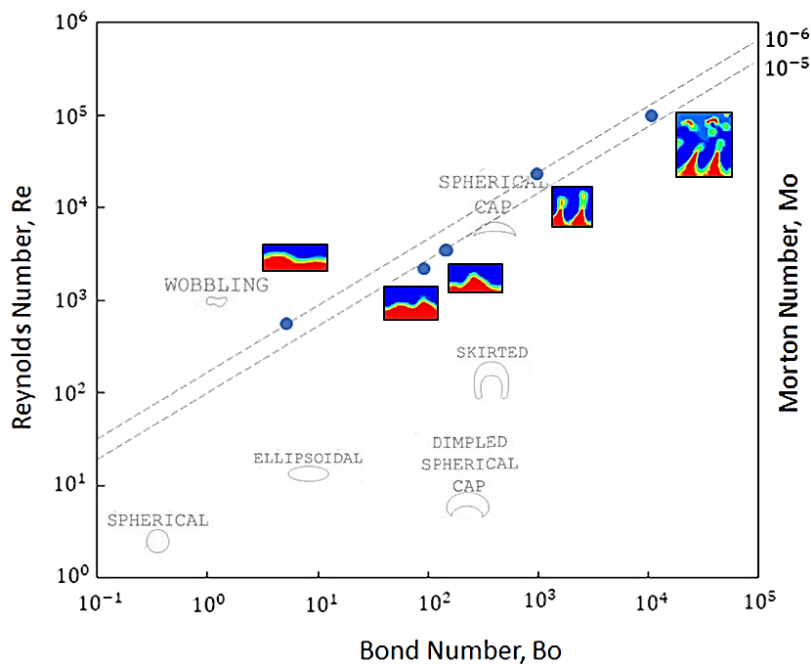


Figure 3-24. Shape regime map for the formation of melt jets overlapped with the bubble shape regime from Amaya-Bower and Lee (2010).

Board, Hall, and Hall (1975) use a simple one-dimensional model of a system in which two liquids (molten metal and water) are initially coarsly mixed and show that the structure a violent thermal steam explosion is analogous with a chemical explosion. It is possible to determine the downstream equilibrium states with the conservation laws and an equation of state without any knowledge of the nonequilibrium mechanical and thermodynamic processes in the “reaction zone” of a thermal explosion wave. These calculations are called the Hugoniot analysis or shock adiabetic.

Hugoniot analysis predicts the properties for a themal detanation. Knowing the initial pressure P_1 , specific volume V_1 and internal energy U_1 , it is possible to deduce the leaving states (U_2, P_2, V_2) with equation (30) along an equation of state.

$$\frac{1}{2}(P_1 + P_2)(V_1 - V_2) = U_2 - U_1 \quad (30)$$

There is only one state which ensures an estable explosion, it is the intersection of Rayleigh line and Hugoniot Curve known as Chapman-Jouguet (C-J) condition. Sonic chocking at C-J enable the explosion front section to propagate independently of the region behind it. Due an explosion must satisfy the C-J condition, the velocities and pressure of propagation can be predicted. Board, Hall, and Hall (1975) calculated de C-J condition for a system of equal volumes of tin, water and steam. With $P_1 = 1$ bar and $V_1 = 0.37$ g/cm³, the C-J point of pressure was found at 1 kbar (100 MPa) and the propagation velocity of 30000 cm/s (300 m/s). Figure 3-25 shows the schematic to obtain the C-J point.

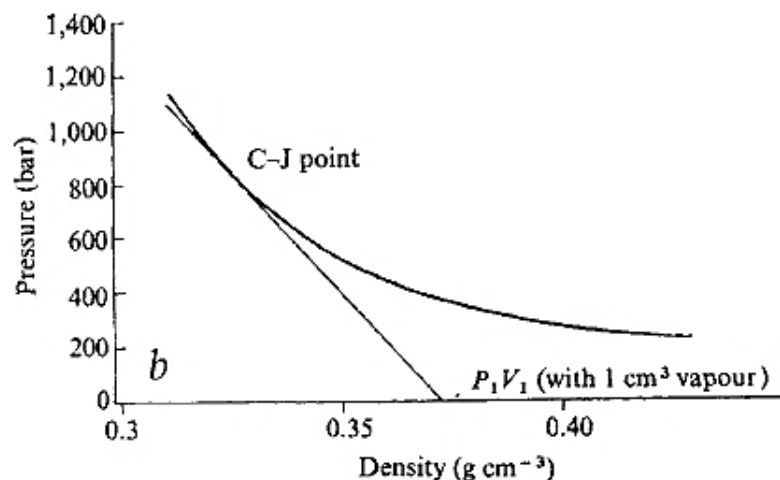


Figure 3-25. Shock adiabat for an initial mixture of equal volumes of tin (1000°C), water (100°C) and steam (Board, Hall, and Hall 1975).

For the studied case of the current simulation, equal volumes of tin and water are used but it is not for steam. Board et al. (1975) mention that if there is little or no vapour initially present in the mixture, the Hugoniot curve remains like the shown above, but the point from which the tangent line is drawn move to a lower specific volume. So, the pressure of the C-J point increases considerably. The propagation velocity is also increased by the absence of vapor.

Very similar to the current studied simulation, Board et al. (1975) mention that for experiments in horizontally and unconstrained metal-water mixtures the reaction region is observed to propagate at only moderate velocity (near 30 m/s) along the melt-water interface and pressures of few tens of MPa are generated. These interactions do not fulfill the conditions for a thermal detonation.

In the studied simulation the maximum pressure value is 100 MPa and the propagation velocity is 62.8 m/s, so thermal detonation point is not reached although melt fragmentation is observed. Figure 3-26 shows the Hugoniot analysis for current simulation with tin (1000°C) and water (100°C) at equal volumes and vapor with a fraction of 0.029126 of the total volume. The C-J point (intersection) of both curves is the low section of Hugoniot curve, so no thermal detonation is presented.

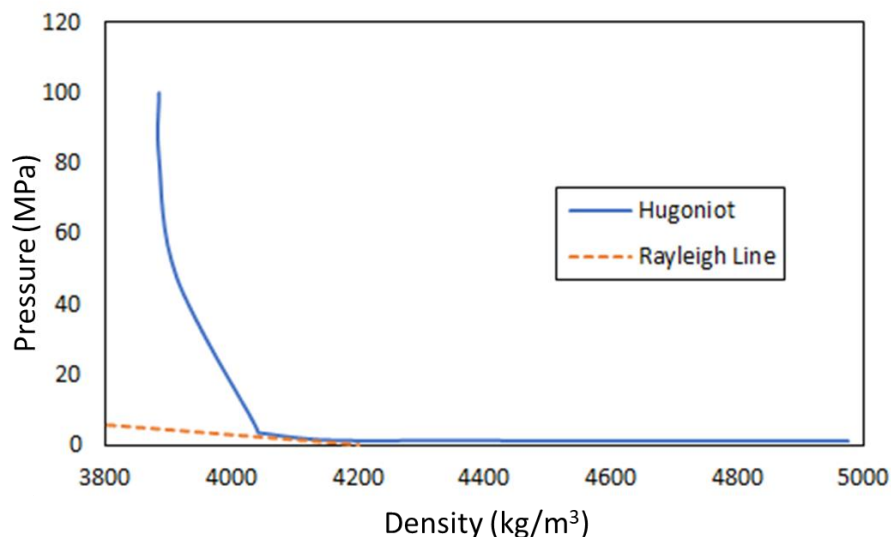


Figure 3-26. Hugoniot analysis for current simulation with tin (1000°C), water (100°C) with equal volumes a vapor with a fraction of 0.029 of the total volume.

3.4.2 Molten Metal Droplet in Water

To observe how the molten metal fragmentation is carried out, simulations about molten metal droplets in water were performed. These models have been already simulated by other authors, but they were performed in this thesis to see if with a simple model and academic software they could be replicated.

Two cases were applied to the simulations of a molten metal droplet in water, the first only has hydrodynamic effects. Isothermal condition is applied for all the domain. And for the second case, the thermal effects are studied. Energy equation and evaporation were habilitated, the melt droplet started with zero velocity.

3.4.2.1 Models 2 and 3. Hydrodynamic simulations

Ma et al. (2002) performed a numerical study on the hydrodynamics of a molten metal droplet with and without vapor film in water pool. They employed a Cubic

Interpolated Pseudo-Particle (CIP) algorithm to perform the calculations. They used a two-dimensional model with domain of 51.2mm x 64mm, and a grid system of 128 x 160. The top boundary was set to Neumann (open) conditions, while the others (side and bottom) were set to Dirichlet (non-slip wall) conditions.

Figure 3-27 shows the results that Ma et al. (2002) got when they simulated a droplet of molten metal with a initial diameter of 8 mm and velocity of 2.5 m/s.

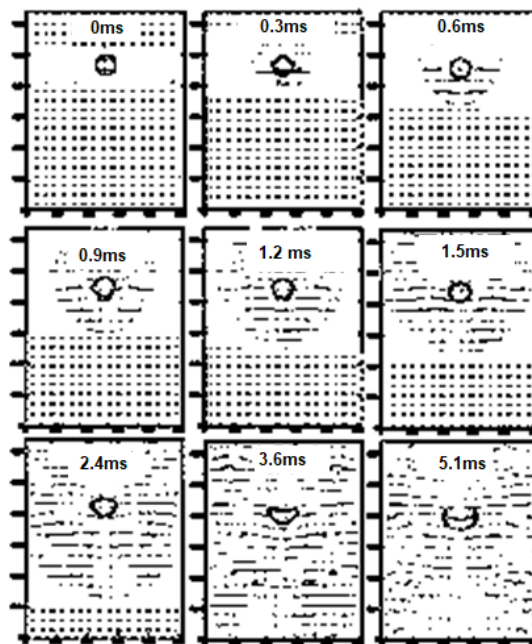


Figure 3-27. Metal droplet without vapor film in water pool (Ma et al. 2002).

Figure 3-28 shows the results that Ma et al. (2002) got when they simulated a droplet of molten metal surrounded by vapor film with a initial diameter of 8 mm, velocity of 2.5 m/s and vapor film thickness of 1.6 mm.

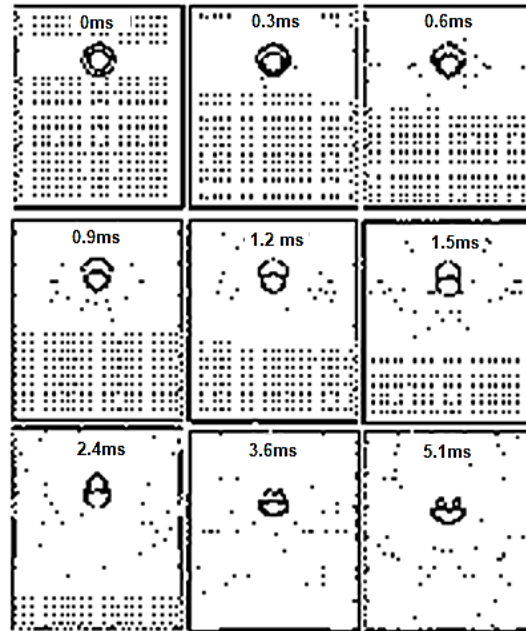


Figure 3-28. Metal droplet with vapor film in water pool (Ma et al. 2002).

Thakre, Ma, and Li (2013) simulated the molten metal droplet preconditioning in the initial phase of a fuel coolant interaction. They used CFD code FLUENT through the Volume of Fluid (VOF) method. They only studied the hydrodynamics of the multiphase system; heat transfer was not considered. They tested two configurations: melt-coolant two-phase system, and melt-coolant-vapor three-phase system.

Thakre, Ma, and Li (2013) used a two-dimensional rectangular domain of 20 mm x 50 mm with quadrilateral meshing. For the two-phase system they used a melt droplet with an initial diameter of 3 mm with an initial velocity of 2.5 m/s. Results for the two-phase system of this simulation are shown in Figure 3-29.

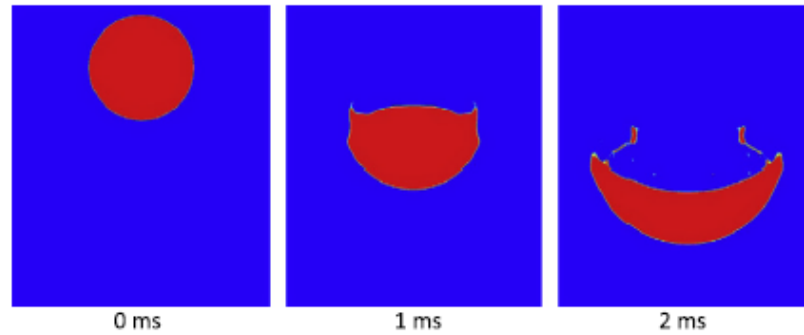


Figure 3-29. Molten metal droplet in water pool (Thakre, Ma, and Li 2013).

Thakre, Ma, and Li (2013) also simulated the case of vapor film around the melt droplet. The vapor film had a thickness of 0.15 mm, the molten droplet a diameter of 3 mm with an initial velocity of 2.5 m/s. Figure 3-30 shows the results they got when the metal droplet was surrounded by a vapor film.

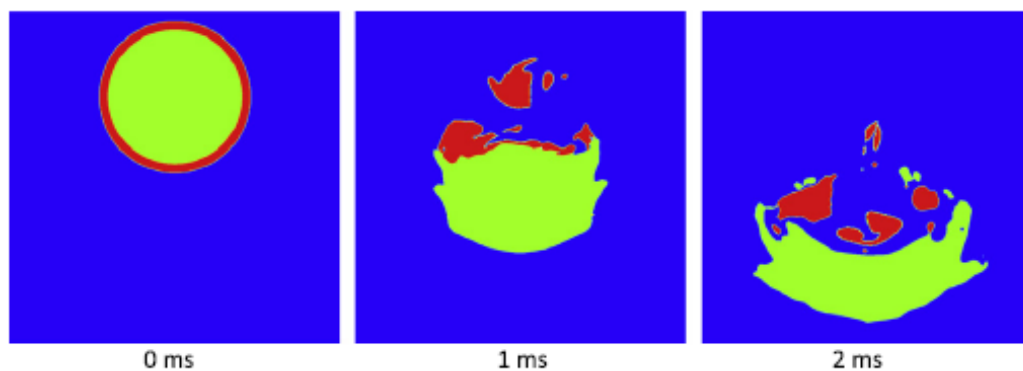


Figure 3-30. Molten metal droplet surrounded by a vapor film (Thakre, Ma, and Li 2013).

The simulations performed in this thesis for these cases were inspired in the presented previous works.

The current simulations were performed with 2-D axisymmetric simulations in ANSYS Fluent software. Standard k- ϵ model is used. The transient flow solver is used to simulate the multi-phase flow.

The volume of fluid method (VOF) is used because it is simple and accurate as it was for the formation of melt jets simulation.

Two phases were defined for the first system. A geo-reconstruct solution scheme for volume fraction is used to track the interfaces. SIMPLEC scheme used for pressure-velocity coupling. Continuum Surface Force model is used in the surface tension model as well as wall adhesion. Surface tension values were the same of Table 3-1. Figure 3-31 shows the geometry and boundary conditions for the two-phase system.

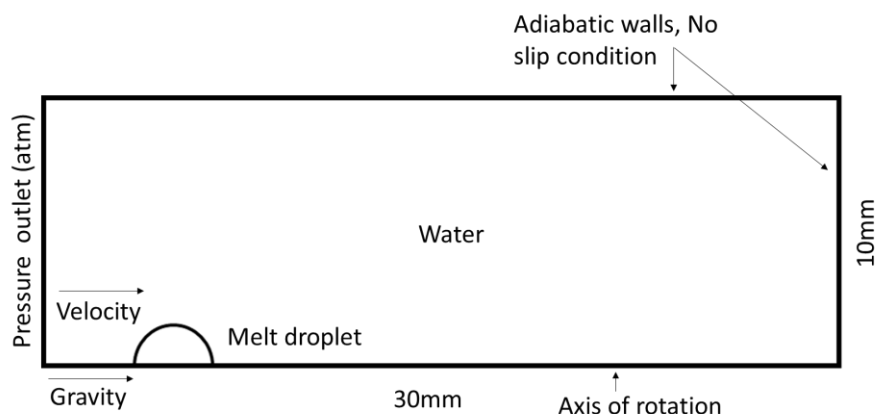


Figure 3-31. Geometry and boundary conditions of melt droplet in water.

The three-phase system consisted in water-vapor-melt, it had a pretty similar configuration to the two-phase system. It was only necessary to add new surface tensions between vapor-water and vapor-melt. Figure 3-32 shows the geometry and boundary conditions for the three-phase system.

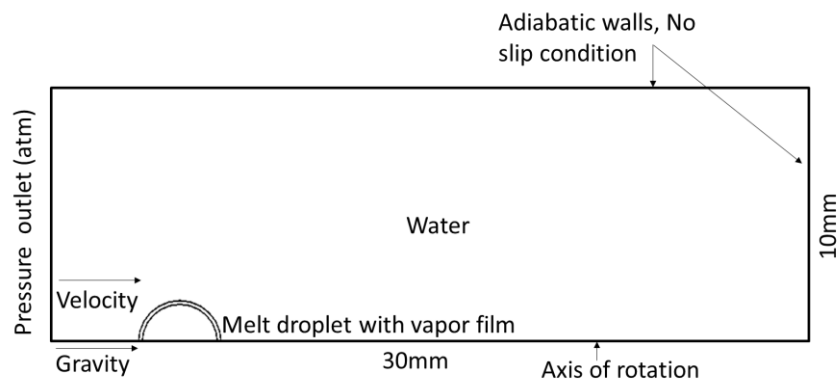


Figure 3-32. Geometry and boundary condition of melt droplet with vapor film in water.

Once the geometry and necessary setup were made for the 2-D simulations of the molten metal droplets in water, measurements of the deformation in the droplet were obtained and studied.

Figure 3-33 shows the deformation sequence of melt droplet in the two-phase system when its initial velocity is 2.5 m/s and initial diameter is 3 mm. The obtained deformation looks similar to the results in Figure 3-27 and Figure 3-29, qualitative agreement is shown between the previous simulations by other authors and current simulation.

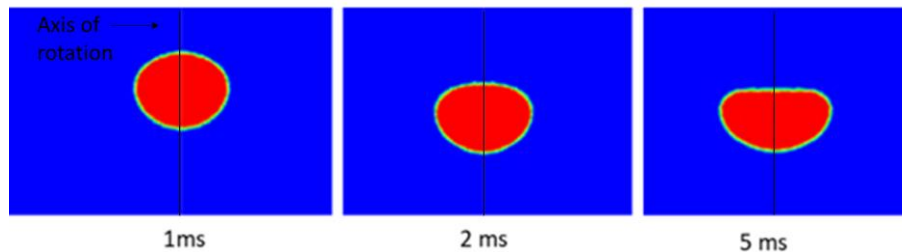


Figure 3-33. Melt droplet deformation through time, when $V_{\text{initial}} = 2.5 \text{ m/s}$.

Figure 3-34 shows the change in the relation between the deformed perimeter P and initial area (A_0) of the melt droplet when initial velocity is varied. The melt droplet deformation increases with an increase in the initial velocity.

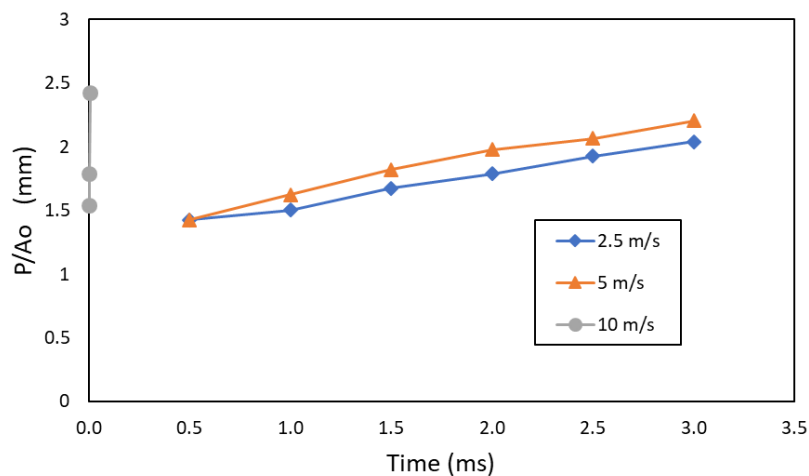


Figure 3-34. Change in droplet perimeter with various initial velocities when density is 6600 kg/m^3 .

Figure 3-35 shows the effects when the initial density is varied, when initial velocity is 2.5 m/s. The results show that for higher densities the deformation in the perimeter of the droplet is going to be greater, but it can be observed that the changes in the deformation are slow. The droplet deformation is more affected by velocity than by density.

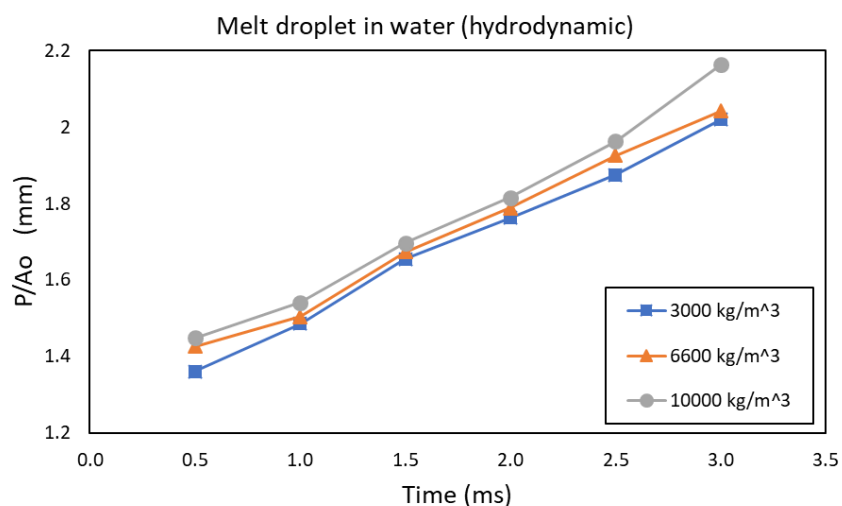


Figure 3-35. Change in droplet perimeter with various melt densities when initial velocity is 2.5 m/s.

Figure 3-36 shows the deformation sequence of melt droplet in the three-phase system when its initial velocity is 2.5 m/s, the initial diameter is 3 mm and vapor film thickness is 0.15 mm. The obtained deformation looks similar to the results in Figure 3-28 and Figure 3-30, qualitative agreement is shown between the previous simulations by other authors and current simulation.

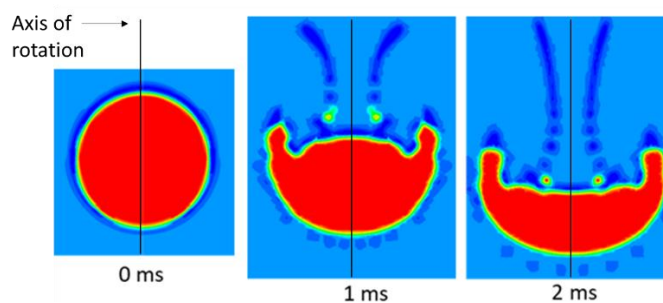


Figure 3-36. Melt droplet with vapor film deformation through time, when $V_{\text{initial}} = 2.5$ m/s.

Figure 3-37 shows the change in the relation between the deformed perimeter P and initial area (A_0) of the melt droplet when initial vapor film thickness is varied. The melt droplet deformation increases when the vapor film thickness is increased. The initial velocity was set to 2.5 m/s and density to 6600 kg/m³

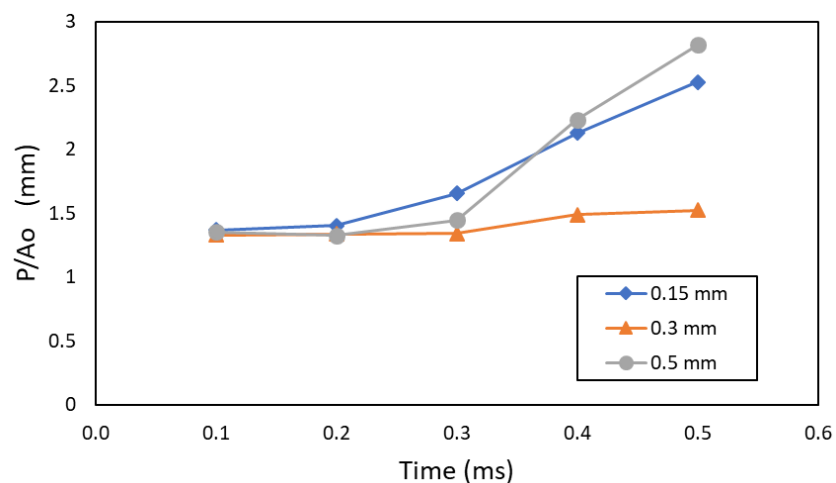


Figure 3-37. Change in droplet perimeter with various vapor film thicknesses.

Figure 3-38 shows the change in the relation between the deformed perimeter P and initial area (A_0) of the melt droplet when initial velocity is varied. The melt droplet deformation increases with an increase in the initial velocity.

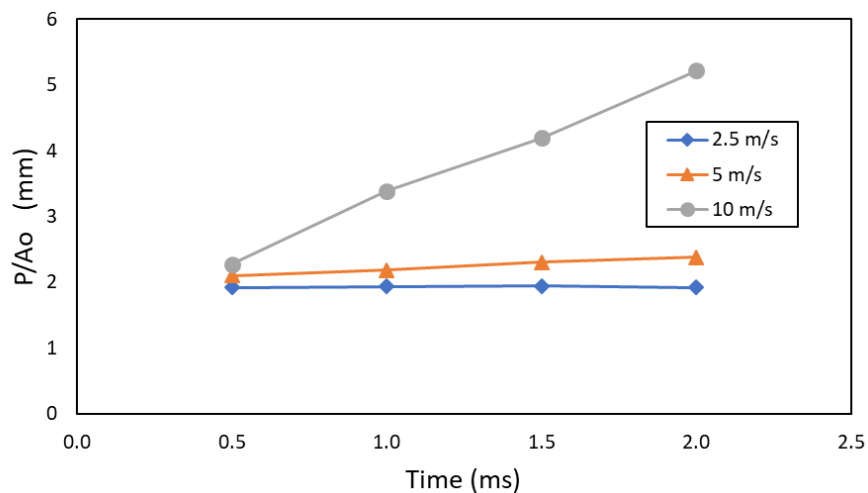


Figure 3-38. Change in droplet perimeter with various initial velocities when density is 6600 kg/m^3 and vapor film thickness is 0.15 mm .

Figure 3-39 shows the effects when the initial density is varied, and the initial velocity of is set to 2.5 m/s and vapor film to 0.15 mm of thickness. It is observed that the increase in density increases the deformation of the melt droplet.

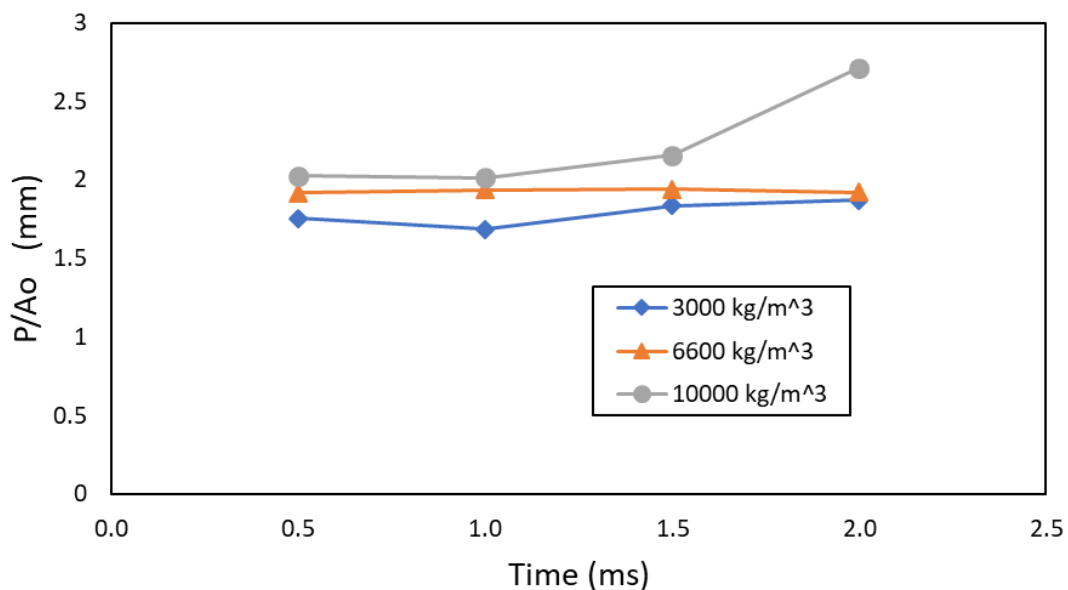


Figure 3-39. Change in droplet perimeter with various initial densities when V_{init} is 2.5 m/s and vapor film thickness is 0.15 mm .

3.4.2.2 Model 4. Thermal simulations

Zhong et al. (2014) performed a numerical study regarding the thermal effects of molten metal droplet fragmentation process that is triggered by an external pressure pulse. They used transient code, continuum surface force (CSF) model for surface tension, evaporation-condensation at the vapor film interface, and VOF method.

Zhong et al. (2014) system, consisted in a molten droplet surrounded by a vapor film in water. A 2-D axisymmetric domain was used of 80 mm (horizontal) x 40 mm (vertical) with an orthogonal grid. Figure 3-40 shows the results they got when a vapor film with 0.3 mm of thickness and a melt density of 7000 kg/m^3 were used.

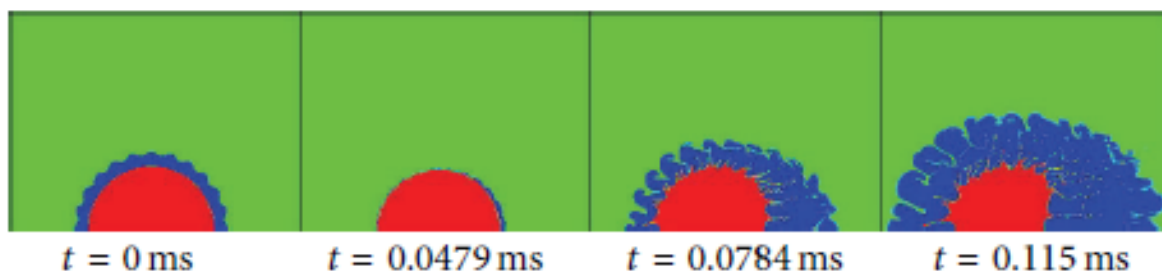


Figure 3-40. Thermal effects on melt droplet with unstable vapor film (Zhong et al. 2014).

The simulations performed in this thesis for the case of a melt droplet surrounded by a vapor film initially at rest were inspired by the works from (Zhong et al. 2014; Zhou et al. 2013).

The simulations were performed with 2-D axisymmetric domain in ANSYS Fluent software. Standard $k-\epsilon$ model is used as well as transient flow solver is used to simulate the multi-phase flow. The volume of fluid method (VOF) is used since the previous reported researches have had success with it.

Four phases were defined for the actual system. Air, water, vapor and tin were defined. A geo-reconstruct solution scheme for volume fraction is used to track the interfaces. SIMPLEC scheme used for pressure-velocity coupling. Continuum

Surface Force model is used in the surface tension model as well as wall adhesion. Surface tensions are 0.468 for water-melt, 0.52 for melt-vapor and 0.072 for water-vapor interface. Evaporation-condensation model is also applied to change water to steam. Gravity goes in axial direction. Figure 3-41 shows the geometry and boundary conditions for the four-phase system.

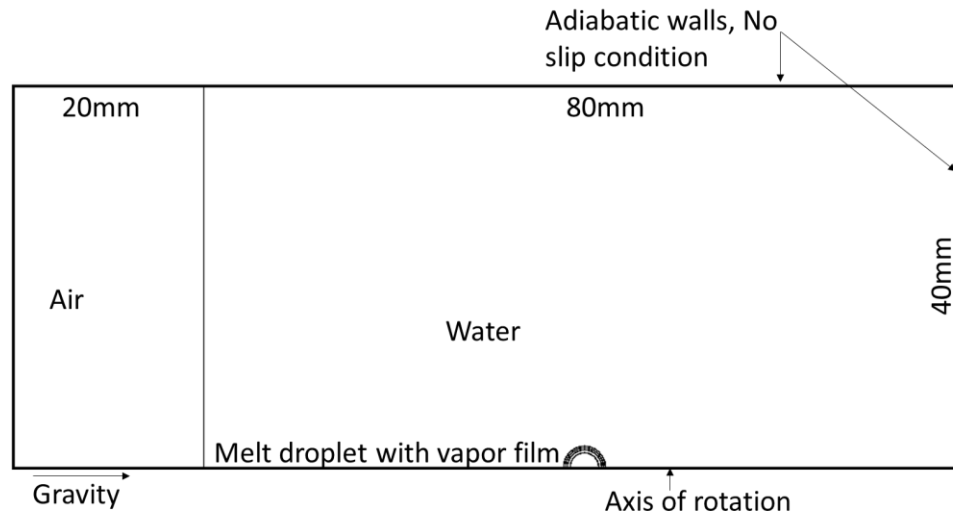


Figure 3-41. Geometry and boundary conditions for melt droplet with vapor film and thermal effects.

The melt droplet starts at rest with a diameter of 3 mm, and a pressure pulse of 4 MPa is added in the first 30 μ s into the vapor film. The initial temperature of water was set to 373K, the temperature for vapor initially was 374K and the one for the melt was set to 1073K.

The tests consisted in varying the initial pressure in the vapor film, varying the melt density and varying the vapor film thickness, in order to know how these parameters affected the results.

Figure 3-42 shows a sequence of the deformation when the vapor film has a thickness of 0.5 mm and the melt density is 10000 kg/m³, this sequence can be compared with Figure 3-40. It certainly does not have the same number of spikes, but the formation and fragmentation of spikes can be observed.

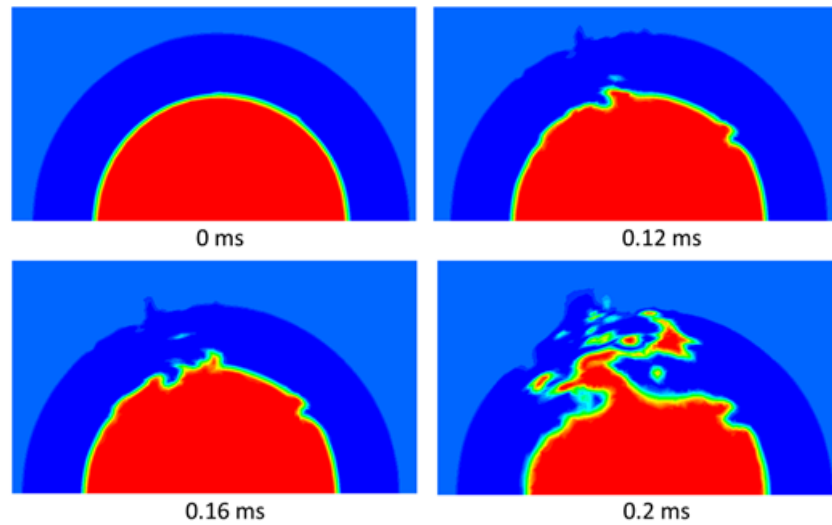


Figure 3-42. Sequence of melt droplet deformation when thermal effects are present.

Figure 3-43 shows the changes of the aspect ratio L/R_0 versus time when different densities are set for the melt droplet. L is the maximum length of the formed spikes and R_0 is the droplet initial radius. The figure indicates that the growth rate of the spike is higher when the melt density is greater.

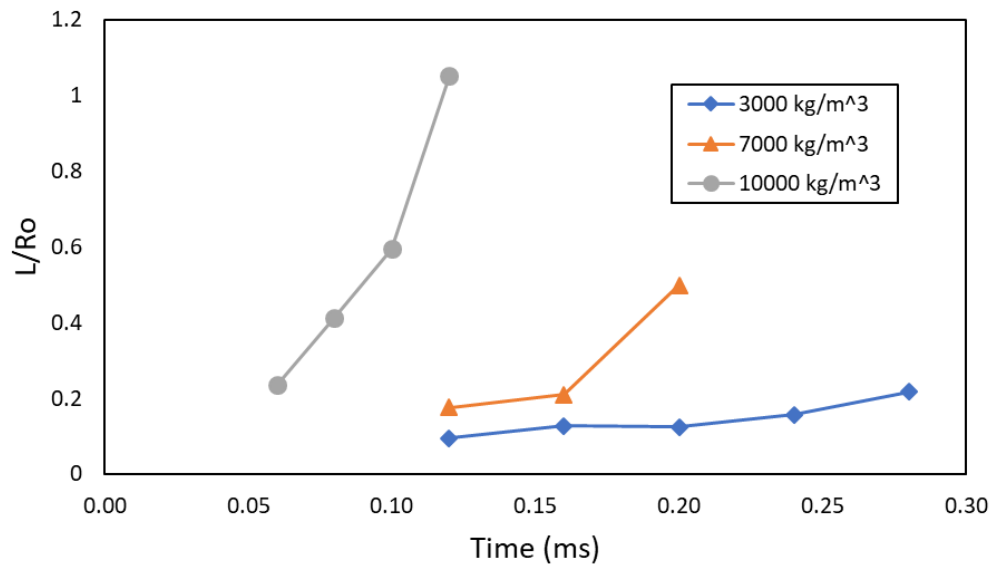


Figure 3-43. Change in spike length with various initial densities when vapor film thickness is 0.5 mm.

Figure 3-44 shows the effects in the aspect ratio L/R_o when various vapor film thicknesses are presented around the melt droplet. It can be observed when the vapor film is thicker the grow in the length of the melt filament is minor.

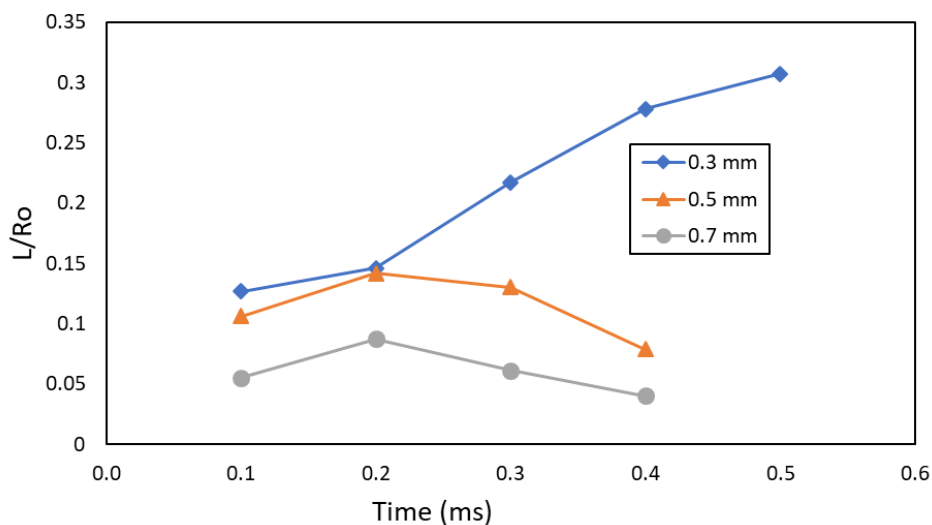


Figure 3-44. Change in spike length with various vapor film thicknesses when melt density is 7000 kg/m^3 .

Table 3-5 shows the calculated Bond number and breakup time adimensional number for the case when the density is varied, and the pressure is kept at 4 MPa.

Table 3-5. Bond number when density is varied, and pressure is 4 MPa.

Density (kg/m^3)	$L/R_o(\text{m})$	Wave Length(m)	Bo	Tb^*
3000	0.095333	5.80E-05	0.6153	3.2463
7000	0.17666	8.10E-05	0.8594	4.5616
10000	1.052	4.77E-04	5.0607	3.4999

For this case, significant droplet deformation is observed when the Bond number is 5, although pressure was much lower than the water/metal stratified system, it was possible to see that the Bond number is correlated with the deformation of the droplet (Figure 3-45).

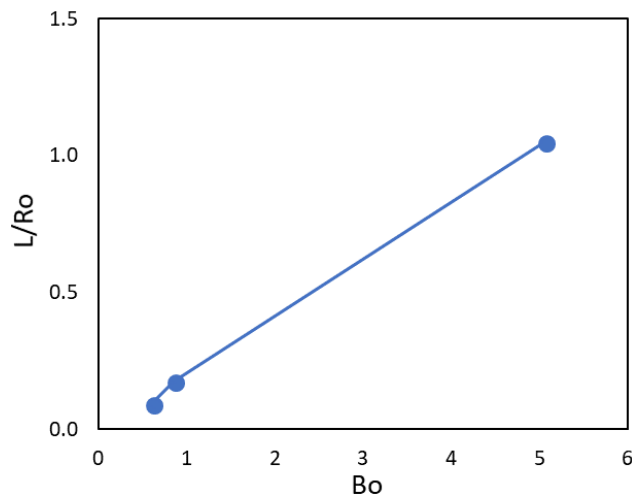


Figure 3-45. Aspect ratio L/Ro according the Bond number.

3.4.3 Model 5. Water Jet Falling in Molten Metal

Koshizuka, Ikeda, and Oka (1999) developed a new numerical method, the moving particle semi-implicit (MPS) method. That is based on moving particles and their interactions. They simulated the fragmentation from water to steam, new particles were generated in the water-steam interfaces. They calculated the water jet impingement on a molten tin pool in two dimensions using the MPS code as a simulation of collapse of a vapor film around a hot melt drop.

One of the geometries Koshizuka, Ikeda, and Oka (1999) used, was the impingement of a single jet shown in Figure 3-46.

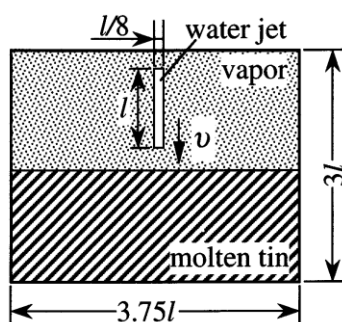


Figure 3-46. Geometry for single water jet in molten metal (Koshizuka, Ikeda, and Oka 1999).

For one of their cases, they used $l = 1.6 \text{ mm}$, $v = 5 \text{ m/s}$, tin temperature at 700°C with density of 6650 kg/m^3 and water at 100°C with density of 958.84 kg/m^3 . The results for these conditions are shown in Figure 3-47, where it can be observed the deformation that the water jet causes in the molten tin.

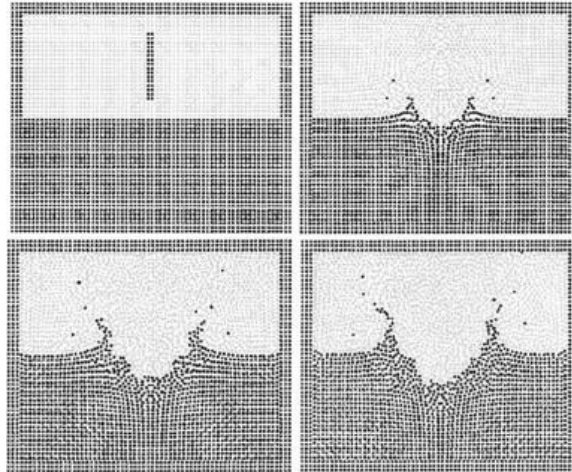


Figure 3-47. Water jet impingement in molten tin in a time interval of 0.6 ms.

Zhou et al. (2014) studied experimentally the interaction behavior of a water droplet with molten metal by a subcooled water droplet into hot molten tin in a thin vessel. They used a high-speed photography system to capture all the important moments when these two fluids interact. The experimental apparatus consisted in a test section, a water tank and an injection nozzle as shown in Figure 3-48.

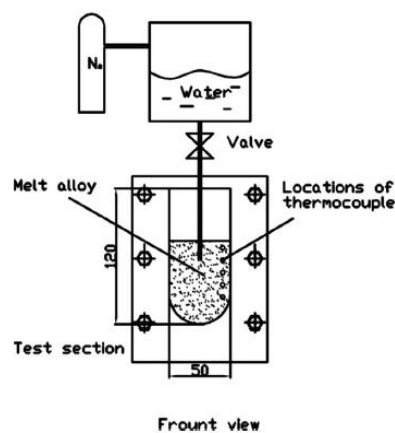


Figure 3-48. Experimental apparatus used by Zhou et al. (2014).

Figure 3-49 shows the results Zhou et al. (2014) got when the water droplet had a temperature of 298K, the tin was at 593K, the initial velocity and diameter of water droplet were 1.6 m/s and 3.31 mm.

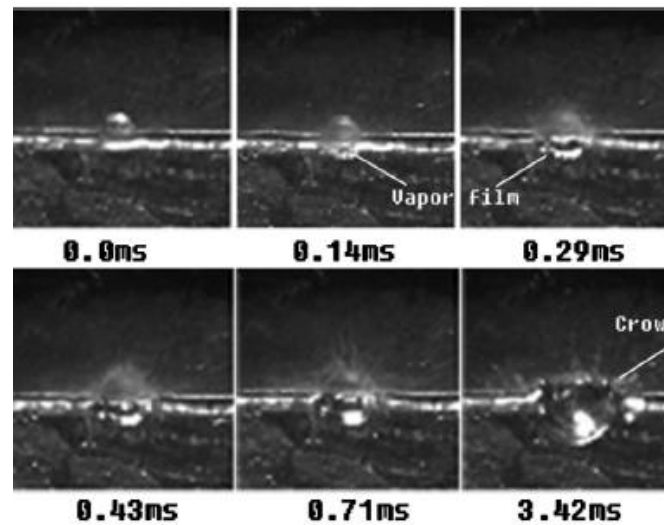


Figure 3-49. Sequence of explosive interaction of a water droplet in molten tin (Zhou et al. 2014).

Lin et al. (2014) continued the work of Zhou et al. (2014), but now with a numerical analysis (simulation). They developed a two-dimensional domain multi-phase thermal code with Volume of Fluid Method (VOF). Their work focuses on the deformation of the molten tin surface after a water droplet contacts it, Figure 3-50 shows the used geometry.

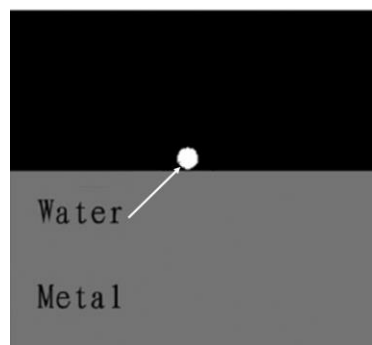


Figure 3-50. Water droplet in molten metal model (Lin et al. 2014).

With the water droplet at 293K, molten tin at 591K, water droplet initial velocity of 0.6 ms and water droplet diameter of 1 mm, Lin et al. (2014) got the results presented in Figure 3-51.

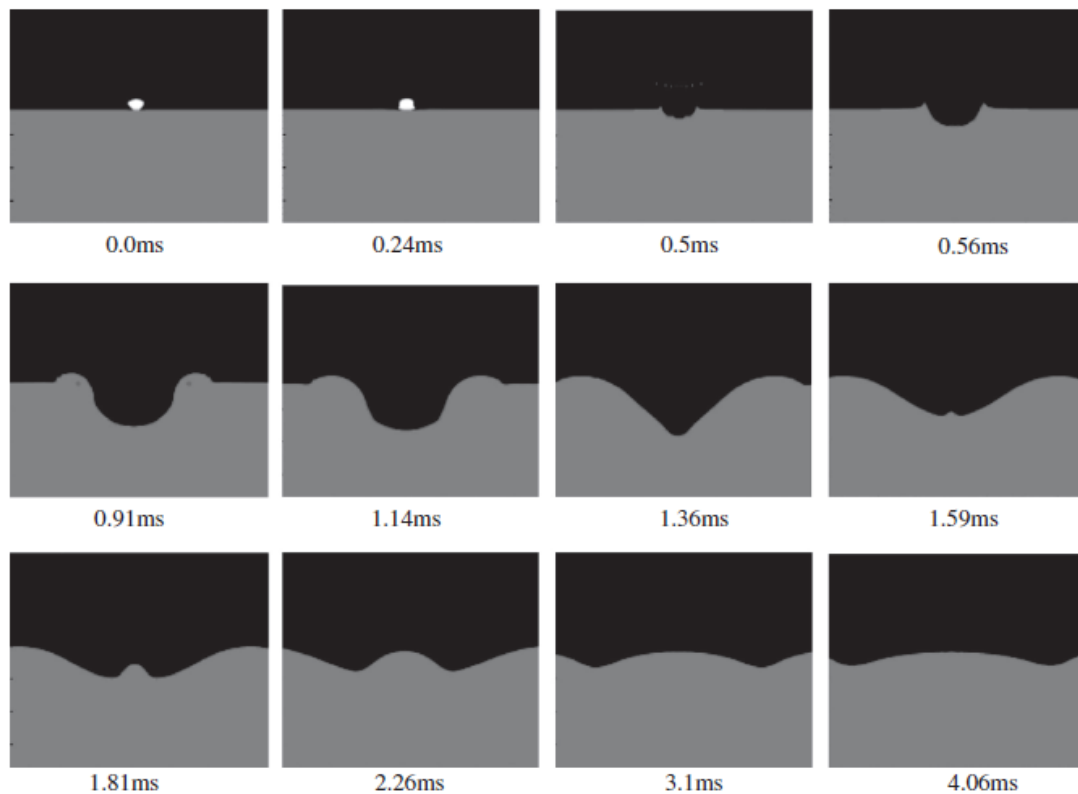


Figure 3-51. Sequence of molten tin surface deformation caused by water droplet (Lin et al. 2014).

Inspired in the presented previous works, simulations of a water jet falling in molten metal were performed in the current thesis. The simulations were performed with two-dimensional domain in ANSYS Fluent software. Standard $k-\epsilon$ model is used, transient flow solver is used to simulate the multi-phase flow. The volume of fluid method (VOF) is used since the previous reported researches have had success with it.

Four phases were defined in the system. Air, water, vapor and tin were defined. A geo-reconstruct solution scheme for volume fraction is used to track the interfaces. SIMPLEC scheme used for pressure-velocity coupling. Continuum Surface Force model is used in the surface tension model as well as wall adhesion. Evaporation-

condensation model is also applief for water and vapor. Figure 3-52 shows the geometry and boundary conditions for the four-phase system.

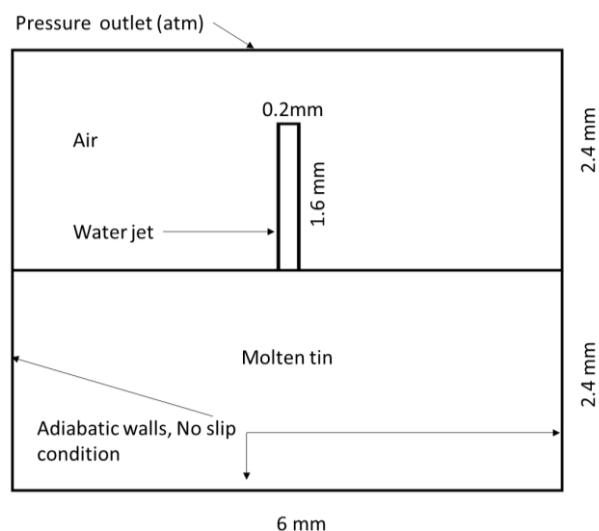
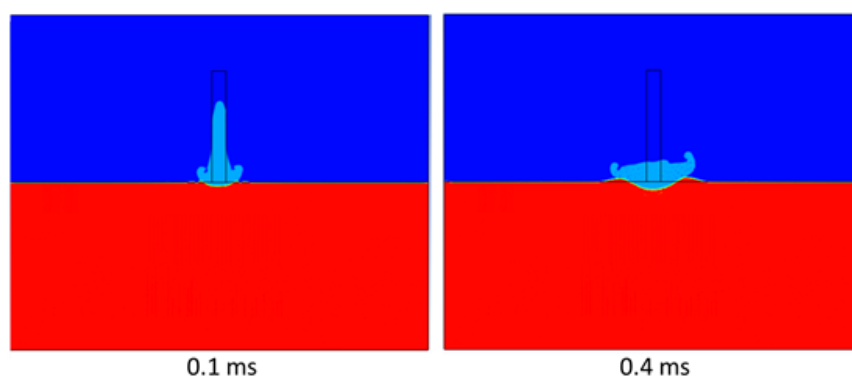


Figure 3-52. Geometry and boundary conditions for water jet falling in molten metal.

The melt droplet starts with a certain initial velocity, with a jet length of 1.6 mm, with a jet width of 0.2mm. Surface tension are 0.468 for water-melt, 0.52 for melt-vapor and 0.072 for water-vapor interface. The initial temperature of water was set to 373K, and the one for the melt was set to 973K. Air was at environment temperature. Initially there is no presence of vapor until the water starts evaporating.

Two simulations were performed with different water jet initial velocity of 5 m/s and 2.5 m/s. Figure 3-53 shows a sequence of the results obtained when the initial velocity was 5 m/s. Water boiling can be observed as little bubbles inside the water.



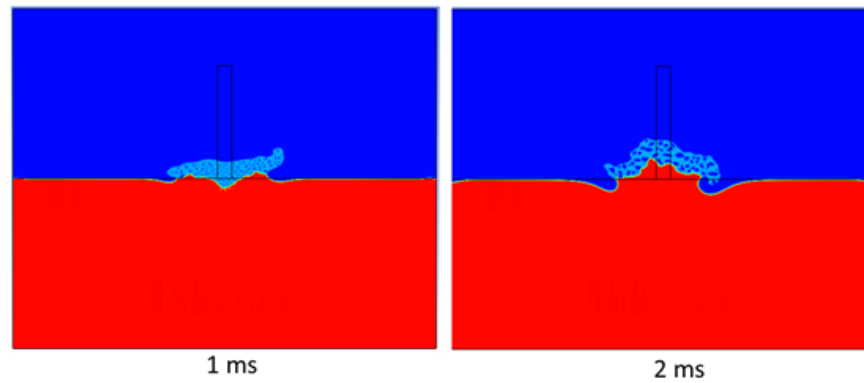


Figure 3-53. Water jet impingement sequence when initial velocity is 5 m/s.

Figure 3-47 and Figure 3-51 were measured with “Digimizer” software since no measurements of them were found in the papers they were taken from. A comparison of the results that were gotten in this thesis is made with the values obtained from the mentioned figures. Figure 3-54 shows the parameters measured from the images. c is the crater width, h is the crater depth (negative if it is a depression, positive if it is a spike) and Do is the width of the water jet or the initial diameter of the water droplet for the case of Lin et al. (2014) simulation.

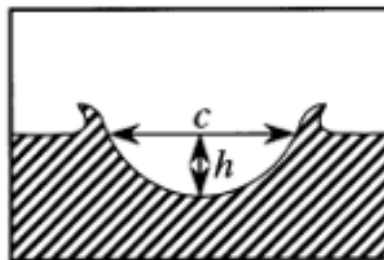


Figure 3-54. Length scales in calculation results.

The next figures show a comparison of the results from own simulations and from other authors simulations. “Koshizuka” series correspond to Figure 3-47, “Lin” corresponde to Figure 3-51. I performed 2 simulations, they are named as “This work 5 m/s”, “This work 5 m/s Software” and “This work 2.5 m/s”. “This work 5 m/s Software” was the only simulation that was measured by the phase fraction values that fluent gives for the molten tin, the other results were measured with “Digimizer”.

Figure 3-55 shows the change in the ratio h/Do for all the simulations. For the most of cases, depth can be observed within the first 1.5 ms, then the molten metal surface tends to grow and form a mountain instead of a valley.

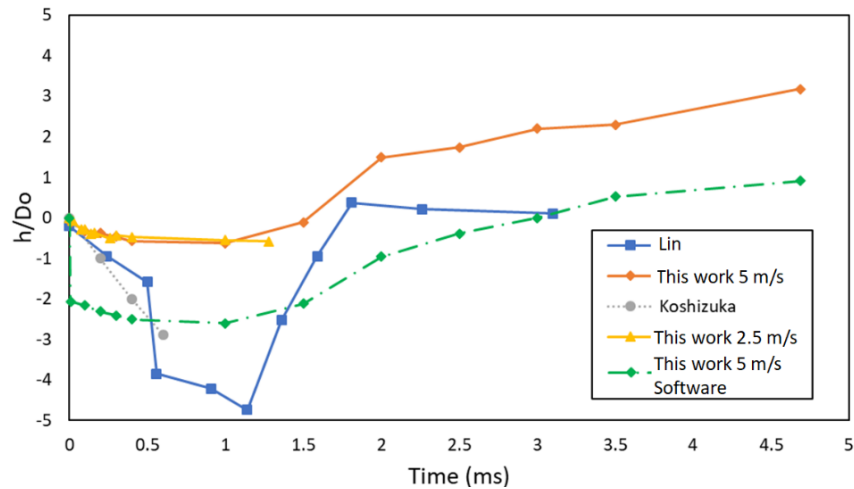


Figure 3-55. Change in the formed crater depth or height through time for various simulations of water falling in molten metal.

Figure 3-56 shows the change in the ratio c/Do for all the simulations. For the most of cases the grow in the crater width is increased over the time.

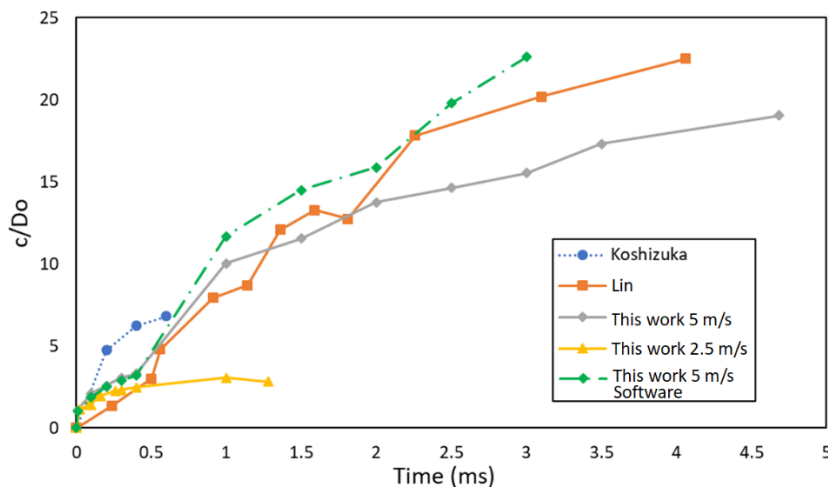


Figure 3-56. Change in the formed crater width through time for various simulations of water falling in molten metal.

3.5 Summary of Results

The first simulation, “Formation of Melt Jets” presented a little more of details. But all the simulations were made to reproduce and to clarify how the molten metal fragmentation is carried out when a hot liquid metal contacts water.

Table 3-6 shows the obtained results for each simulated model.

Table 3-6. Summary of results for molten metal fragmentation.

Model	Cases	Results	Contribution
1	<ul style="list-style-type: none"> • Varying pressure. • Varying density. • Varying vapor film thickness. 	Melt spikes are longer if the initial pressure and /or density are bigger.	It was possible to find a relation with Bond number, significant melt deformation is found when Bo is near 100, and fragmentation when Bo is near 1000. Good comparison with shape of bubbles literature using Bo , Mo and Re was performed. C-J plane was drawn for current simulation, no detonation point was found.
2	<ul style="list-style-type: none"> • Varying velocity. • Varying density. 	More deformation is observed for higher velocity and/or density.	40, 160 and 641 Weber numbers were obtained, it was confirmed that for $We > 350$ a catastrophic breakup is presented.
3	<ul style="list-style-type: none"> • Varying vapor film thickness. • Varying velocity. • Varying density. 	Same as model 2. Also, thicker vapor film causes bigger deformation.	A bigger deformation and fragmentation than model 2 is present because the surface tension is lower for vapor-water interface than for just melt-water interface.
4	<ul style="list-style-type: none"> • Varying density. • Varying vapor film thickness. 	Higher density causes a bigger deformation. Thinner vapor film causes bigger deformation.	Bond number could be obtained, when $Bo > 5$ significant deformation in the droplet surface can be observed.
5	<ul style="list-style-type: none"> • Varying velocity. 	Bigger velocity causes a bigger width in the formed crater.	It was possible to compare the results with previous literature. The crater width grows proportionally regardless if it is a water jet or water droplet.

The thermal and hydrodynamic effects are very important to understand the metal fragmentation, the performed simulations help to know that a metal droplet can be fragmented by its contact with water depending on its velocity and density. So, these

studies help to identify the most affecting variables for the phenomenon, as summary it can be said that:

- For the water/metal stratified system, the melt fragmentation will be greater if the initial pressure in the vapor film, the melt density and the vapor film thickness are bigger. For the water/metal stratified system, it can be said that when Bond number is near the value of 100, the deformation of the melt is significant and when the Bond number is near 1000, the melt fragmentation is observed.
- A molten metal droplet falling in water is fragmented quicker if its velocity and/or density is bigger, due to Weber number, although the effects are faster if the velocity is increased.
- A molten metal droplet surrounded by a vapor film falling in water presents the same behavior of the above point. It gets more deformed when its vapor film is thicker but spend a little more time to deform than for a thinner vapor film.
- A molten metal droplet surrounded by a vapor film in water with thermal effects is affected in a greater way if the melt droplet density is higher, and it is less affected if the vapor film is thicker.
- When a water jet is falling in molten metal, the thermal effects accelerate the metal fragmentation process. The width of the formed craters tends to grow with time but the depth changes from negative to positive because the walls of the vessel push backwards the melt that is deformed by the water.

In order to confirm the behavior that the water/metal stratified system was having, deep neural network algorithm reported in (Contreras-Serna et al. 2018) with a TensorFlow library that was implemented to facilitate the understanding of the

studied phenomena. Their results are not shown in this thesis, but they were able to predict the number of melt spikes and the maximum spike length with a very good precision.

3.6 Conclusions

It was shown that molten metal fragmentation in the presence of water can be observed through computational fluid dynamics techniques.

With simplified two-dimensional simulations it was possible to capture the formation of metal spikes under conditions (e.g., high pressure) similar to those reported previously for the case of water/metal stratified system. The other cases were also able to be simulated and good comparisons can be made qualitatively with the previous simulations reported for them.

Water penetration was not observed but the chance cannot be discarded. Hence, the 3-D simulation will be carried out in the future.

About molten metal fragmentation it can be said that the contact of molten metal with water does not necessarily have to generate a steam explosion but the conditions of both liquid and environment can affect them to generate a steam explosion. When there exists a difference in velocities or a pressure pulse disturbs the system, a steam explosion can be generated.

This topic is also relevant in nuclear engineering processes like generation plants where the nuclear fuel is at very high temperatures and can have contact with the present coolant water.

3.7 Future Work

To continue the development of this research topic, the following suggestions are made:

- A pressure pulse can be programmed in the vapor film instead of patching it as an initial condition.
- Simulations may be performed for all cases in a 3-D domain to have more reliable results. However, the axisymmetric model should be run first on those cases where pure 2-D planar model results were presented.
- Other metals should be tested to evaluate the changes that may occur in melt fragmentation due to surface tension values. Alternative coolants may be chosen as well.
- Experimental tests may be performed to validate the simulations. This will require the acquisition of a high quality slow motion camera, pressure transducers, equipment to melt and to keep metals, and security equipment since the experiments can be dangerous.
- Although dimensionless numbers like Weber and Bond are useful in estimating melt fragmentation onset, derivations for the hydrodynamic instability equations can be performed by adding a perturbation in the equations. This will allow finding the values in density, pressure and initial velocity that give rise to melt fragmentation.
- Plenty more test cases should be executed to complete the shape regime map about the formation of melt jets in Figure 3-24. The zones for certain type of melt spikes could be found according to their Reynolds, Bond and Morton numbers.

Once the preconditions are well analyzed for each case, the next step to study is the thermal detonation of the steam explosion. A more detailed C-J analysis should be performed as well as a detailed analysis of the energy associated with the explosions which is related to the amount of molten metal and water involved.

Chapter 4. Contributions

Two relevant topics were studied, even though, they are not very related. The only common thing that both topics have is that a water leak into molten metal can generate a steam explosion.

Both topics are important and should be studied with more detail, the current thesis only demonstrates that they can be simulated and that satisfactory results can be obtained with these simulations.

This thesis results tell the steel industry that the steam (water vapor) can take a specific path inside the off-gases duct of an EAF. Hence, if they know the portion of the duct by where more quantity of steam is entered, with the results of chapter 2 they can place in a better position a gas detector.

The results about molten metal fragmentation corroborates to the literature that the melt fragmentation is affected by the velocities, densities and pressure of the system. Also, a simulation, the one for the water/metal stratified system, was performed when no previous simulations made of it were found. So, this thesis aportes specifically, for this case, a new numerical study (simulation) about the formation of melt jets in the interaction of hot molten metal with water

Bibliography

- Amaya-Bower, Luz, and Taehun Lee. 2010. "Single Bubble Rising Dynamics for Moderate Reynolds Number Using Lattice Boltzmann Method." *Computers and Fluids* 39(7): 1191–1207. <http://dx.doi.org/10.1016/j.compfluid.2010.03.003>.
- BCSA, Steel for Life, and SCI. 2012. "No Title." <https://www.steelconstruction.info/File:EAF-dia.PNG> (May 8, 2018).
- Bekker, J G, I K Craig, and P C Pistorius. 2000. "Model Predictive Control of an Electric Arc Furnace off-Gas Process." *Control Engineering Practice* 8(4): 445–55. <http://www.sciencedirect.com/science/article/pii/S096706619900163X>.
- Bergstroem, T H. 1995. "A Review of Molten Metal-Water Reactions." In *ELECTRIC FURNACE CONFERENCE*, , 303.
- Board, S. J., R. W. Hall, and R. S. Hall. 1975. "Detonation of Fuel Coolant Explosions." *Nature* 254(5498): 319–21.
- Boin, Nadia, Armando Vazquez, and Pierluca Levrangi. 2012. "Improving EAF Performance and Enhancing Safety with EFSOP®." *Millennium Steel*: 59–64.
- Cengel, Yunus A., and John M.; Cimbala. 2014. *Fluid Mechanics: Fundamentals and Applications*. http://highered.mheducation.com/sites/0073380326/information_center_view0/index.html.
- Ciccarelli, Gaby. 1991. "Investigation of Vapor Explosions with Single Molten Metal Drops in Water Using Flash X-Ray." McGill University.
- Ciccarelli, Gaby, and David L Frost. 1994. "Fragmentation Mechanisms Based on Single Drop Steam Explosion Experiments Using Flash X-Ray Radiography." *Nuclear Engineering and Design* 146(1): 109–32. <http://www.sciencedirect.com/science/article/pii/0029549394903247>.
- Corradini, M L, B J Kim, and M D Oh. 1988. "Vapor Explosions in Light Water Reactors: A Review of Theory and Modeling." *Progress in Nuclear Energy* 22(1): 1–117. <http://www.sciencedirect.com/science/article/pii/0149197088900042>.
- Cronenberg, A W. 1980. "Recent Developments in the Understanding of Energetic

- Molten Fuel-Coolant Interactions.” *Nucl. Saf.:(United States)* 21(3).
- Dennis, P, and S Ganguly. 2010. “SAF Water Leak Detection By The Measurement of Gaseous Water Vapour.”
- Eckhoff, Rolf K. 2016. “Water Vapour Explosions – A Brief Review.” *Journal of Loss Prevention in the Process Industries* 40: 188–98. <http://www.sciencedirect.com/science/article/pii/S0950423015300681>.
- Fletcher, D F, and R P Anderson. 1990. “A Review of Pressure-Induced Propagation Models of the Vapour Explosion Process.” *Progress in Nuclear Energy* 23(2): 137–79. <http://www.sciencedirect.com/science/article/pii/0149197090900103>.
- Ghobara, Emad Moustafa Yasser. 2013. “Modeling, Optimization and Estimation in Electric Arc Furnace (EAF) Operation.”
- Gilbert, C P. 1979. *Nuclear Reactor Safety-a Review of the Rasmussen Report (WASH-1400)*. Australian Nuclear Science and Technology Organisation.
- Hyder, M L, and D K Allison. 1992. *A Review of Vapor Explosion Information Pertinent to the SRS Reactors*.
- Kirschen, Marcus, Viktor Velikorodov, and Herbert Pfeifer. 2006. “Mathematical Modelling of Heat Transfer in Dedusting Plants and Comparison to off-Gas Measurements at Electric Arc Furnaces.” *Energy* 31(14): 2590–2603.
- Koshizuka, Seiichi, Hirokazu Ikeda, and Yoshiaki Oka. 1999. “Numerical Analysis of Fragmentation Mechanisms in Vapor Explosions.” *Nuclear Engineering and Design* 189(1): 423–33. <http://www.sciencedirect.com/science/article/pii/S0029549398002702>.
- Leclerc, Eric, and Georges J Berthoud. 2003. “Modeling of Melt Droplet Fragmentation Following Vapor Film Destabilization by a Trigger Pulse.” *Nuclear technology* 144(2): 158–74.
- Lee, J H S, and D L Frost. 1987. “Steam Explosions-Major Problems and Current Status.” *Proc. 11th ICDERS, Warsaw, Poland*.
- Li, Gang, and Tingchao Ji. 2016. “Severe Accidental Water Vapour Explosions in a Foundry in China in 2012.” *Journal of Loss Prevention in the Process Industries* 41: 55–59. <http://www.sciencedirect.com/science/article/pii/S0950423016300547>.

- Lin, Meng et al. 2014. "Molten Metal and Water Direct Contact Interaction Research – II. Numerical Analysis." *Annals of Nuclear Energy* 70: 256–65. <http://www.sciencedirect.com/science/article/pii/S0306454913005884>.
- Ma, W.M., Z.L. Yang, A. Giri, and B.R. Sehgal. 2002. "Numerical Simulation of Hydrodynamics of a Heavy Liquid Drop Covered by Vapor Film in a Water Pool." *International Conference on Nuclear Engineering, Proceedings, ICONE 3*.
- Malfa, Enrico et al. 2009. "APPLICATION OF CFD AT EAF PROCESS SIMULATION." *Innovation in EAF and Steelmaking Process, Milan, Italy*: 27–28.
- P. Dennis, S.Ganguly. 2010. "SAF WATER LEAK DETECTION BY THE MEASUREMENT OF GASEOUS WATER VAPOUR." *The Twelfth International Ferroalloys Congress Sustainable Future*: 759–68.
- Patel, P. D., and T. G. Theofanous. 1981. "Hydrodynamic Fragmentation of Drops." *Journal of Fluid Mechanics* 103: 207–23.
- Pilch M., Erdman C A Reynolds A B. 1979. *Acceleration Induced Fragmentation of Liquid Droplets, Report NUREG/CR-2247 Prepared for the Nucl. Reg. Commission, USA*. Australian Nuclear Science and Technology Organisation.
- Pinto, Thiago, Breno Totti, and Paulo Hopperdizel. 2015. "Earliest Leak Detection (ELD): A New Concept of Security in Water Leak Detection in Electric Arc Furnaces." *The Iron & Steel Technology Conference and Exposition*: 88–93.
- Piriz, A R, O D Cortazar, J J Lopez Cela, and N A Tahir. 2006. "The Rayleigh-Taylor Instability." *American journal of physics* 74(12): 1095–98.
- Sharp, D H. 1984. "An Overview of Rayleigh-Taylor Instability." *Physica D: Nonlinear Phenomena* 12(1): 3–18. <http://www.sciencedirect.com/science/article/pii/0167278984905104>.
- Spencer, A J, and D S Cochran. 2015. "Design Decomposition for Selecting an Electric Arc Furnace Off-Gas System for SDI Butler Flat Roll Division." *Procedia CIRP* 34: 143–49. <http://www.sciencedirect.com/science/article/pii/S221282711500846X>.
- T. P. Wandekoken B. T. Maia, P Hopperdizel. 2015. "Earliest Leak Detection (ELD): A New Concept of Security in Water Leak Detection in Electric Arc Furnaces."

- In *The Iron & Steel Technology Conference and Exposition*, , 88–93.
- Thakre, Sachin, Weimin Ma, and Liangxing Li. 2013. “A Numerical Analysis on Hydrodynamic Deformation of Molten Droplets in a Water Pool.” *Annals of Nuclear Energy* 53: 228–37.
<http://www.sciencedirect.com/science/article/pii/S0306454912003581>.
- Timoshenko, N, A Semko, and S Timoshenko. 2014. “Modelling of Electric Arc Furnace off-Gas Removal System.” *Ironmaking & Steelmaking* 41(4): 257–61.
<https://doi.org/10.1179/1743281213Y.0000000163>.
- Witte, L C, J E Cox, and J E Bouvier. 1970. “The Vapor Explosion.” *JOM-Journal of the Minerals, Metals and Materials Society* 22: 39–44.
- Zhang, S F et al. 2009. “Analyses on 3-D Gas Flow and Heat Transfer in Ladle Furnace Lid.” *Applied Mathematical Modelling* 33(6): 2646–62.
<http://www.sciencedirect.com/science/article/pii/S0307904X08001996>.
- Zhong, Mingjun et al. 2014. “A Numerical Analysis Research on Earlier Behavior of Molten Droplet Covered with Vapor Film at the Stage of Triggering and Propagation in Steam Explosion.” *Science and Technology of Nuclear Installations* 2014.
- Zhou, Yuan et al. 2013. “Numerical Simulation of Fragmentation of Melt Drop Triggered by External Pressure Pulse in Vapor Explosions.” *Annals of Nuclear Energy* 57: 92–99.
<http://www.sciencedirect.com/science/article/pii/S0306454913000625>.
- . 2014. “Molten Metal and Water Direct Contact Interaction Research – I. Photographic Experiment Study.” *Annals of Nuclear Energy* 70: 248–55.
<http://www.sciencedirect.com/science/article/pii/S0306454913005859>.

Appendix A

Abbreviations, acronyms and symbols.

Table A-1. Abbreviations.

	Description
CFD	Computational Fluid Dynamics
CIP	Cubic Interpolated Pseudo-Particle algorithm
CSF	Continuum Surface Force
EES	Engineering Equation Solver
MPS	Moving Particle Semi-implicit
TDLAS	Tunable Diode Laser Absorption Spectrometer
VOF	Volume of Fluid method

Table A-2. Acronyms.

	Description
2-D	Two-dimensional
3-D	Three-dimensional
CO	Carbon Monoxide
CO ₂	Carbon Dioxide
DRI	Direct Reduced Iron
EAF	Electric Arc Furnace
FCI	Fuel-Coolant Interaction
H ₂	Hydrogen
H ₂ O	Steam (Water Vapor)
P-V-T	Pressure-Volume-Temperature

Table A-3. Symbols.

Variable	Description
a	Minimum element size
A_o	Initial Area
A_T	Total area
c	Crater width
C_p	Specific heat
D_o	Droplet initial diameter
e	Energy per unit mass
F	External body forces
g	Gravity
h	Element length
h	Crater depth
i	Specie number

J_i	Diffusion flux of species
k	Wave number
$k-\varepsilon$	Turbulence model
L	Maximum length of melt spikes
M	Molar mass
m	Mass flow rate
n	Unit normal vector
NE	Number of elements
NN	Number of nodes
P	Droplet perimeter
P_{in}	Pressure in gas Inlet
p	Pressure
R	Gas ideal constant = 8.3144598 J/K-mol
R_i	Net rate of production by chemical reaction
R_o	Droplet initial radius
S_h	Source term
S_i	Creation rate
S_m	Mass added to the continuous phase
T	Temperature
t	Time
v	Fluid velocity
We	Weber number
Y_i	Local mass fraction
α	Fractional volume
λ	Thermal conductivity; Wave length
ξ	New position
ρ	Density of fluid
σ	Surface tension
μ	Dynamic viscosity
ϕ	Heat transfer rate
Γ	Volume expansion or contraction
δ	Dirac distribution

Table A-4. Subscripts

Subscripts	Description
i	Phase index
l	Liquid
v	Vapor
m	Molten metal
x	X direction
y	Y direction

Curriculum Vitae

Jorge Contreras Serna was born in Monterrey, México, on 1993. He obtained the Mechatronics Engineering degree from the Universidad Autónoma de Nuevo León (UANL) with the best grades of his generation in June 2015. On August 2016 Jorge joined to the national postgraduate SENER-Conacyt program at Instituto Tecnológico y de Estudios Superiores de Monterrey (ITESM), Monterrey Campus, to achieve his master's degree in Energy Engineering.

Conference paper accepted for publication in FESDM 2018 by ASME in July, Montreal, Quebec, Canada:

- **Title:** Numerical Simulation of Formation of Melt Jets in Melt-Coolant Interactions.

Conference paper presented in CONAC 2018 by AIST in March, Monterrey, Nuevo León, México:

- **Title:** Water leaks detection in off-gas duct of Electric Arc Furnace (EAF).

Contact information:

- Jorge Contreras Serna
- jorge_10.007@hotmail.com
- <https://www.linkedin.com/in/jorge-contreras-s/>

This document was typed in using Microsoft Word by Jorge Contreras Serna.